RAPID ASCENT OF KIMBERLITES AS INDICATED BY COEXISTING MELT AND FLUID PHASES IN PERIDOTITES

Megan Dayl Purchase

In accordance with the requirements for the

M.Sc. degree

In the Department of Geology,

Faculty of Natural and Agricultural Sciences,

University of the Free State

July 2013

Supervisor: Dr. Holger Sommer

Declaration

I, Megan Dayl Purchase, declare that the dissertation hereby submitted for the qualification M.Sc. Geology, at the University of the Free State, is my own independent work and I have not previously submitted the same work for a qualification at/in another university or faculty.

MD Purchase 1 July 2013

Abstract

This thesis involves the investigation of OH^- in defect structures within garnets taken from peridotites. The information obtained from this is used to estimate the ascent rate of kimberlites to the surface. The importance of determining this ascent rate involves the resorption rate of diamond, which are inversely proportional to each other, as well as the energy needed for the kimberlitic melt to raise dense xenoliths to the surface. The samples used in this study are ten peridotitic xenoliths from the Bultfontein kimberlite mine, South Africa. The samples range from garnet to spinel peridotites and are either harzburgites or lherzolites. Scanning Electron Microscopy (SEM) was used to determine mineral chemistry which was also used in a geothermobarometric study. Fourier Transform InfraRed (FT-IR) spectroscopy investigated the mentioned defect structures for OH^- and other volatiles, which were not present. An optical petrographic study also took place. During the petrographic investigation, serpentine and phlogopite were observed and dissolution of garnet to spinel. Serpentine suggests hydration and the phlogopite shows evidence of an Al-, Ti- and K-rich, hydrous silicate melt. Garnet is unstable when interacting with melt at <40 km depth below the surface and temperatures greater than 850 ºC, forming spinel. Temperatures obtained in this study range from 1145 K–1893 K and pressures range from 0.56 GPa–6.03 GPa for various samples. The variations are owing to different metamorphic grades of the samples. The variation in results on the same sample is due to the effect that different analytical methods have on the accuracy of the geothermobarometry. Using the diffusion rate of OH^- from within a defect structure out into the matrix of a garnet grain, the ascent rate for the kimberlite was determined and ranges between 30min to a couple of hours.

Table of Contents

List of figures

List of tables

1 Introduction

Diamonds were discovered in South Africa in the 1860s along the Orange river (Erlich and Hausel, 2002). James Gregory, London diamond dealer, was sent to South Africa to investigate on the mining possibilities. He reported that the possibility were slim and that ostriches carried the diamonds to the Orange river (Erlich and Hausel, 2002). This mining statement was obviously proven untrue and resulted in years of mining. Diamond diggers travelled upstream and discovered placer deposits, which were later renamed kimberlites (Erlich and Hausel, 2002). At this stage kimberlites were only known as the diamond-bearing material, where the weathered kimberlite was called ‘yellow ground’ and fresh samples were referred to as ‘blue ground’ (Lewis, 1897). Mining of kimberlites in South Africa began in 1876 that mining of (Erlich and Hausel, 2002) and are nowadays defined as a group of ultrabasic rocks that are rich in volatiles and potassium (Mitchell, 1986).

Kimberlites are an important transport medium for xenoliths and xenocrysts from the mantle to the surface. A great portion of the xenoliths are peridotites, which are constituents of the mantle. The peridotites are only slightly chemically modified by the kimberlitic magma during this transportation process, suggesting a rapid rise from within the mantle (Peslier et al., 2008). There are many varieties of peridotites and due to the fact that they are ultramafic rocks, they mainly consist of olivine, ferro-magnesium minerals (pyroxenes) (Streckeisen, 1976) and accessory minerals (garnet, spinel and phlogopite). Peridotites are classified according to their composition and their textures. The composition of the peridotites classifies them into different rock types (lherzolite, harzburgite, wherlite and dunite), shown in figure 1.1, and is dependent on the normalized percentages of olivine, orthopyroxene and

clinopyroxene. Garnets from lherzolitic and harzburgitic rocks can then be differentiated from each other by using their compositions in a CaO versus Cr_2O_3 plot (Figure 1.2). A diagonal line is used to separate G9 and G10 garnets, where a G9 garnet is derived from a lherzolite and a G10 garnet from a harzburgite, (Gurney, 1984).

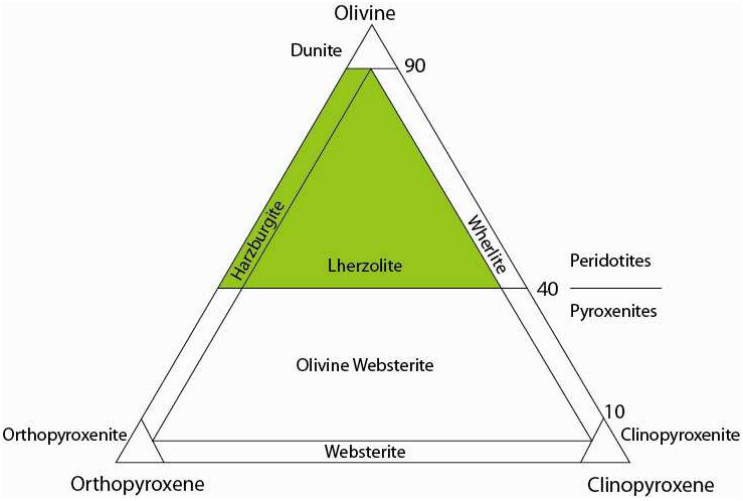

Figure 1.1: Classification diagram of peridotites, dependant on the quantities of olivine, orthopyroxene and clinopyroxene. Modified after (Streckeisen, 1976).

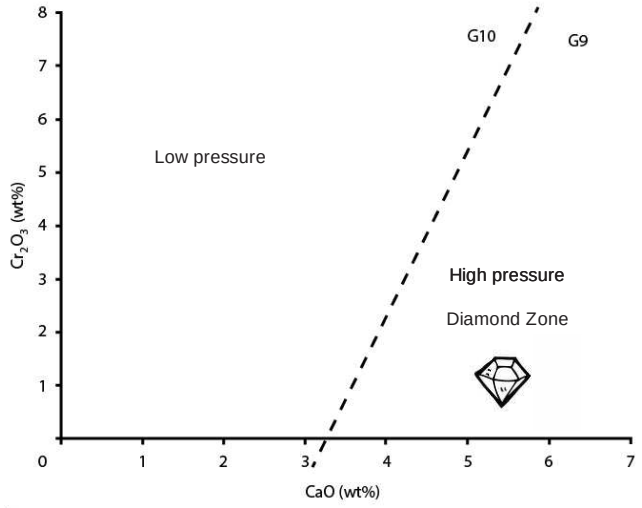

Figure 1.2: Separation of G10 garnets (harzburgite origin) and G9 garnets (lherzolite origin) with a plot of Cr_2O_3 vs. CaO compositions of the garnets (modified after Gurney, 1984).

According to Nielson Pike and Schwarzma (1977), peridotites can also be classified according to textures found within the rock. These authors mention that ultramafic xenoliths, transported with kimberlites and basalts, commonly have textures of metamorphic tectonites. They also mentioned that the types of textures found in ultramafic xenoliths show that many of them have experienced several metamorphic episodes and occasionally display relics of preserved igneous texture. The main idea is to separate the rocks into metamorphic type rocks and igneous type rocks with great emphasis on textures. The classification and the textures of each of these can be found in table 1. With each classification defect structures may be present.

Table 1: Textural classification of xenoliths, extracted from Nielson Pike and Schwarzma (1977).

Category	**Criteria**
Igneous and Pyrometamorphic	Igneous: Cross cutting veins, zoning and exsolution in pyroxenes, growth twins in pyroxene; grain shapes are euhedral to polygonal, grain-size: coarse (3-4 mm), euhedral spinel between or in silicate minerals, poikilitic texture.
	Pyrometamorphic: Interstitial glass; pyroxenes with spongy borders, clinopyroxene-spinel boundaries: plagioclase and olivine; clinopyroxene boundaries: spinel and plagioclase.
Metamorphic	Porphyroclastic: Large strained irregular grains that have curved boundaries, matrix of fine-grained strain-free recrystallized grains that may display foliation.
	Cataclastic: Large strained grains that have serrated boundaries, matrix consists of grains that are strained and grain boundaries that are usually sutured.
	Foliated: Foliated in hand specimen, grains are elongated and unstrained, foliation plains are concentrated with long grains, equigranular.
	Equigranular-mosaic: Grains are polygonal and equidimensional, straight or gently curved grain boundaries, triple junctions (120°) predominate.
Allotriomorphic-Granular	Grains are coarse-grained (3-4mm) equidimensional and anhedral.

Defect structures, according to Wenk and Bulak (2004), are flaws in the repeat of atoms in the crystal lattice. Types of defects (Figure 1.3) include: point defects (vacancies), line defects (dislocations) and planar defects. These authors also explain that a point defect involves the introduction (this includes impurities, e.g.: Al^{3+} in a Si^{4+} site) or the removal of an atom in the general repetition of the crystal lattice; that a line defect is the interruption of the crystal lattice and the displacement of atoms along a line and; a planar defect is the displacement of atoms over an entire plane. Sommer et al. (2008) reports that the mantle contains defects in the form of cracks which are present in the first 180km of the Earth's surface, which have been active for the past several hundred millions years. It has been suggested that plate tectonics relies on these cracks to facilitate a lubricant (volatiles) for motion (Sommer et al., 2008).

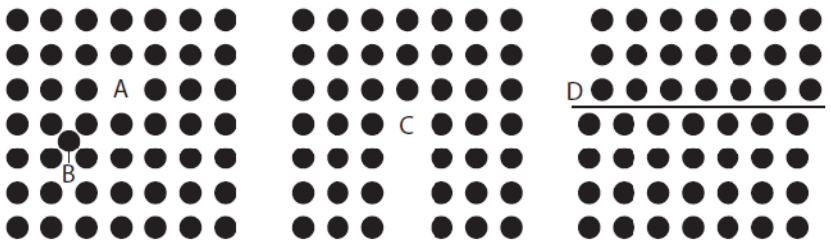

Figure 1.3: Image displaying the types of defects in crystals. A: point defect, removal of an atom. B: point defect, addition of an atom. C: line defect. D: planar defect. Modified after Wenk and Bulak (2004).

Volatiles such as: OH^- and H_2O are possibly found within defect structures and diffusion profiles, which will be discussed later, may form as the volatile diffuses out of these defect structures. Hydrogen in the upper mantle averages at a few 100ppm by weight as the component H_2O (Hirth and Kohlstedt, 1996). The extraction of hydrogen from the mantle occurs in the form of OH^- and H_2O dissolved in basaltic melts (O'Leary, 2007). Nominally anhydrous minerals (such as pyroxene, olivine and

garnet) are hydrogen poor minerals yet they may incorporate low quantities of hydrogen in defect structures (Miller et al., 1987). Bell and Rossman (1991, 1992a, 1992b) have carried out extensive infrared studies on the OH^- content in garnets derived from the mantle. They found that garnets display a typical OH^- infrared band position at 3570 cm^{-1} (wavenumber) and a smaller band position at 3670 cm^{-1}. In general though, the OH^- band position ranges from 3400 to 3700 cm^{-1} (Bell and Rossman, 1991). Examples of these infrared spectra, occurring in different environments, are shown in figure 1.4. As mentioned OH^- diffuses out of the defect structures.

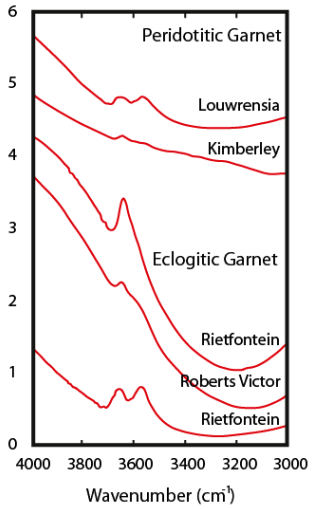

Figure 1.4: Modified after Beran and Libowitzky (2006), showing infrared absorption spectra in the OH^- region of garnets found within xenoliths from southern Africa.

Diffusion profiles, phenocryst dissolution and glass zoning are examples of reactions that take place between the host magma and the xenoliths (Rutherford, 2008). Magma ascent rates can be determined through the diffusion of a hydrous component in a garnet or an olivine, representing a “geospeedometer” (Wang et al., 1996). Diffusion involves the transportation of matter caused by a driving force, such

as chemical potential- or temperature gradient (Ingrin and Blanchard, 2006). Figure 1.5 displays a chemical gradient and the random motion of the particles to form a uniform distribution. Zhang (2010) reports that diffusion occurs through defect structures within a crystalline phase. This author also mentions that the diffusion rate is proportional to the concentration of defects in the crystal lattice and therefore proportional to the ionic porosity (IP - the amount of vacancies in the structure). Diffusion profile can be used to determine the ascent rate of kimberlites.

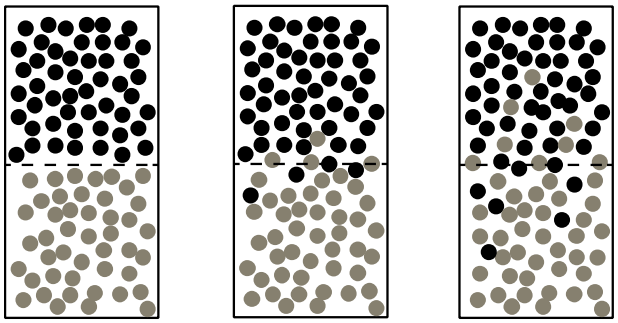

Figure 1.5: Initially within a crystal (from left), the grey particles (e.g.: Fe^{2+} ions) fill the lower half and black particles (e.g.: Mg^{2+} ions) fill the upper half. Random motion allows a flux of the grey particles upwards and the black particles downwards (last two images). Over time, all the particles will be uniformly distributed throughout the entire system (modified after Zhang, 2010).

In these samples, the ascent rate of the kimberlite can be determined by determining the OH^- content in defect structures and along diffusion profiles, as mentioned. The exact speed of ascent and the eruption process of kimberlites are still under debate. The importance of knowing this is to understand the volatile budgets, the investigation of mantle rocks and the mechanisms and dynamics of the eruption process (emplacement model) (Peslier et al., 2008).

There are many possible emplacement models for kimberlites, the Weertman crack model will be considered for this thesis, due to the fact that it is a model that allows

the magma to ascent at high enough speeds. A Weertman crack (Weertman, 1971a; Weertman, 1971b; Spence and Turcotte, 1990; Roper and Lister, 2007; Takada, 1990) involves a fluid filled fracture that is buoyancy – driven and according to Sommer and Gauert (2011) these cracks are a potential mechanism for kimberlitic melts to reach the surface. Sommer and Gauert (2011) also mention that this theory involves the uniform movement of liquid filled cracks where the crack's length remains constant. Weertman, 1971b expresses that within the crack there is a pressure gradient that will drive the fluid upwards. This author also explains that the crack breaks through into the solid above due to stress and the stress that was previously found above the tip of the static crack is now released, thus creating a pressure gradient that will continue to push the fluid towards the surface. The driving force is gravitational potential energy or the buoyancy of the fluid and magma transport in the crack can reach velocities of Rayleigh-wave speed (Sommer and Gauert, 2011). Geothermobarometry will be discussed further.

Geothermobarometry involves calculations supplying results of temperatures and pressures of the event when the rock was last in equilibrium (Spear, 1993). Geothermometers use reactions that exhibit temperature sensitivity with a small pressure sensitivity (Spear, 1993). Exchange reactions or partitioning of elements between two coexisting mineral phases, has long been used as useful geothermometers (Harley, 1984). Garnet has the tendency to fractionate Fe into most phases surrounding them and these can then be used as geothermometers (e.g. garnet-biotite, garnet-olivine, garnet-clinopyroxene, garnet-cordierite, etc.) (Harley, 1984). Table 2 displays examples of different types of geothermometers and geobarometers taken from Spear (1993). The following geothermometers were used in this study: garnet-biotite, garnet-orthopyroxene, and two pyroxene thermometers.

Table 2: Examples of geothermometers and exchange reactions involved in each (Spear, 1993), as well as the reasons why the others weren't used in this study. The methods that were used in this study are in italics.

Exchange thermometers	**Reaction**	**Reason for not being used**
Garnet-biotite	*$Fe_3Al_2Si_3O_{12}$+$KMg_3AlSi_3O_{10}(OH)_2$ ↕* *$Mg_3Al_2Si_3O_{12}$+$KFe_3AlSi_3O_{10}(OH)_2$*	
Garnet-cordierite	$2Fe_3Al_2Si_3O_{12}+3Mg_2Al_4Si_5O_{18}$ ↕ $2Mg_3Al_2Si_3O_{12}+3Fe_2Al_4Si_5O_{18}$	There is no cordierite found in the samples
Garnet-clinopyroxene	$Fe_3Al_2Si_3O_{12}+3CaMgSi_2O_6$ ↕ $Mg_3Al_2Si_3O_{12}+3CaFeSi_2O_6$	No consecutive grains were found
Garnet-hornblende	$4Mg_3Al_2Si_3O_{12}+NaCa_2Fe_4Al_3Si_6O_{10}(OH)_2$ ↕ $4Fe_3Al_2Si_3O_{12}+3NaCa_2Mg_4Al_3Si_6O_{10}(OH)_2$	There is no hornblende found in the samples
Garnet-orthopyroxene	*$Mg_3Al_2Si_3O_{12}$+$3FeSiO_3$ ↕* *$Fe_3Al_2Si_3O_{12}$+$3MgSiO_3$*	
Garnet-olivine	$2Mg_3Al_2Si_3O_{12}+3Fe_2SiO_4$ ↕ $2Fe_3Al_2Si_3O_{12}+3Mg_2SiO_4$	No consecutive grains were found
Biotite-tourmaline	$KMg_3AlSi_3O_{10}(OH)_2$+Fe tourmaline ↕ $KFe_3AlSi_3O_{10}(OH)_2$+Mg tourmaline	There is no tourmaline found in the samples
Garnet-chlorite	$5Mg_3Al_2Si_3O_{12}+3Fe_5Al_2Si_3O_{10}(OH)_8$ ↕ $5Fe_3Al_2Si_3O_{12}+3Mg_5Al_2Si_3O_{10}(OH)_8$	There is no chlorite found in the samples
Garnet-ilmenite	$Fe_3Al_2Si_3O_{12}+3MnTiO_3$ ↕ $Mn_3Al_2Si_3O_{12}+3FeTiO_3$	There is no ilmenite found in the samples
Garnet-phengite	$Mg_3Al_2Si_3O_{12}+3KFeAlSi_4O_{10}(OH)_2$ = $Fe_3Al_2Si_3O_{12}+3KMgAlSi_4O_{10}(OH)_2$	There is no phengite found in the samples
Solvus thermometers		
Two pyroxene	*Distribution of Ca and Mg between coexisting orthopyroxene and clinopyroxene*	
Calcite-dolomite	Distribution of Ca and Mg between coexisting dolomite and calcite	There is no calcite or dolomite found in the samples
Two feldspar	Distribution of K and Na between coexisting K-feldspar and plagioclase	The samples formed at temperatures where plagioclase breaks-down
Muscovite-paragonite	Distribution of K and Na between coexisting muscovite and paragonite	There is no muscovite or paragonite found in the samples

Table 2 (continued)

Net transfer equilibria		
Garnet-plagioclase-quartz-Al_2SiO_5	$3CaAl_2Si_2O_8 \leftrightarrow Ca_3Al_2Si_3O_{12} + 2Al_2SiO_5 + SiO_2$	There is no plagioclase or quartz found in the samples
Garnet-plagioclase-muscovite-biotite	$Fe_3Al_2Si_3O_{12}+Ca_3Al_2Si_3O_{12}+$ $KAl_3Si_3O_{10}(OH)_2 \updownarrow$ $3CaAl_2Si_2O_8+KFe_3AlSi_3O_{10}(OH)_2$	There is no plagioclase or muscovite found in the samples
Garnet-plagioclase-muscovite-biotite	$Mg_3Al_2Si_3O_{12}+Ca_3Al_2Si_3O_{12}+$ $KAl_3Si_3O_{10}(OH)_2 \updownarrow$ $3CaAl_2Si_2O_8+KMg_3AlSi_3O_{10}(OH)_2$	There is no plagioclase or muscovite found in the samples
Garnet-plagioclase-muscovite-quartz	$Fe_3Al_2Si_3O_{12}+2Ca_3Al_2Si_3O_{12}+$ $3Al_2Fe_{-1}Si_{-1}+6SiO_2 \leftrightarrow 6CaAl_2Si_2O_8$	There is no plagioclase or muscovite or quartz found in the samples
Garnet-muscovite-quartz-Al_2SiO_5	$Fe_3Al_2Si_3O_{12}+3Al_2Fe_{-1}Si_{-1}+4SiO_2 \updownarrow$ $4Al_2SiO_5$	There is no muscovite or quartz found in the samples

According to Spear (1993), garnet-biotite geothermometry is based on the exchange of Mg and Fe as shown in the equation below along with the minerals that are broken down and minerals that are formed.

$Fe_3Al_2Si_3O_{12} + KMg_3AlSi_3O_{10}(OH)_2 \leftrightarrow Mg_3Al_2Si_3O_{12} + KFe_3AlSi_3O_{10}(OH)_2$

almandine + phlogopite ↔ pyrope + annite

The distribution coefficient of Mg and Fe in the minerals can be calculated using the following equation (Spear, 1993):

$$K_D = \left\{\frac{Fe}{Mg}\right\}^{ga} / \left\{\frac{Fe}{Mg}\right\}^{bt}$$

This can then be used to calculate the pressure and temperature in the following equation (Spear, 1993):

$$52.112 - 19.51T(K) + 0.238P(bars) + 3RTlnK_D = 0$$

According to Harley (1984), garnet-orthopyroxene geothermometers involve the exchange of Mg and Fe viewed in the following equation:

$Mg_3Al_2Si_3O_{12}$+3$FeSiO_3$ ↔ $Fe_3Al_2Si_3O_{12}$+3$MgSiO_3$

pyrope + ferrosilite ↔ almandine + enstatite

The distribution coefficient between the two minerals can be calculated using the following equation (Harley, 1984):

$$K_D = \left\{\frac{Fe}{Mg}\right\}^{ga} / \left\{\frac{Fe}{Mg}\right\}^{opx}$$

This can then be used to calculate the pressure and temperature using the following equation (Harley, 1984):

$$T(℃) = \left\{\frac{3.74 + 1.4X_{gr}^{ga} + 22.86P(kbars)}{RTlnK_D + 1.96}\right\} - 273$$

where:

$$X_{gr}^{ga} = (\frac{Ca}{Ca + Mg + Fe})^{ga}$$

According to Gasparik (1984), two pyroxene geothermometer involves the exchange of Ca between diopside ($CaMgSi_2O_6$) and enstatites ($MgSiO_3$). This geothermometer is excellent due to the fact that Ca/(Ca+Mg) ratios of clinopyroxene are slightly dependent on pressure (Gasparik, 1984). The distribution coefficient of Ca between

clinopyroxene and orthopyroxene can be determined using the following equation (Brey and Kohler, 1990):

$$K_D = (1 - Ca)^{cpx}/(1 - Ca)^{opx}$$

The K_D values are then used to determine the temperature and pressure in the following equation (Brey and Kohler, 1990):

$$T = \frac{23664 + 24.9P}{13.38 + (lnK_D)^2} \quad range\ of\ 2 - 60kb$$

with temperature in Kelvin and pressure in kilobars.

This thesis uses OH^- contents measured by synchrotron based FT-IR across a garnet grain from a mantle xenolith to calculate the time of OH^- loss during the transportation within a kimberlite to the surface. Topics that this thesis will be based on is: *"Metasomatism and effects of a kimberlitic melt on peridotitic xenoliths", "Peridotitic depth of origin" and "Kimberlitic melt's ascent rate",* Results will show that kimberlitic melts ascend faster than alkali basaltic melts from their source to the surface of the earth, which preserves the OH^- content in the mantle xenoliths. The ascent rate then suggests that the eruption process of kimberlites is violent and rapid.

2 Methodology

2.1 Sample area and preparation

In the Kimberley area there is a cluster of kimberlites that have been dated at 84 ± 3Ma (Clement et al., 1979). This cluster consists of five larger kimberlite pipes (Figure 2.1A); namely Bultfontein, De Beers, DuToitspan, Kimberley ('Big Hole') and Wesselton mines (Poujol et al., 2003) and a number of smaller pipes (Wagner, 1914). The samples studied here, were taken from a mine dump containing material from the Bultfontein pipe (Figure 2.1B). This pipe consisted of a brecciated column with fragments of sandstone, dolerite and shale (Field et al., 2008). Figure 2.1 displays the Kimberley area as well as the Bultfontein pipe. The xenoliths found in this mine are mostly peridotites (harzburgites, lherzolites, dunites and wherlites), mica-rich rocks that are less common and eclogites that are rare (Field et al., 2008).

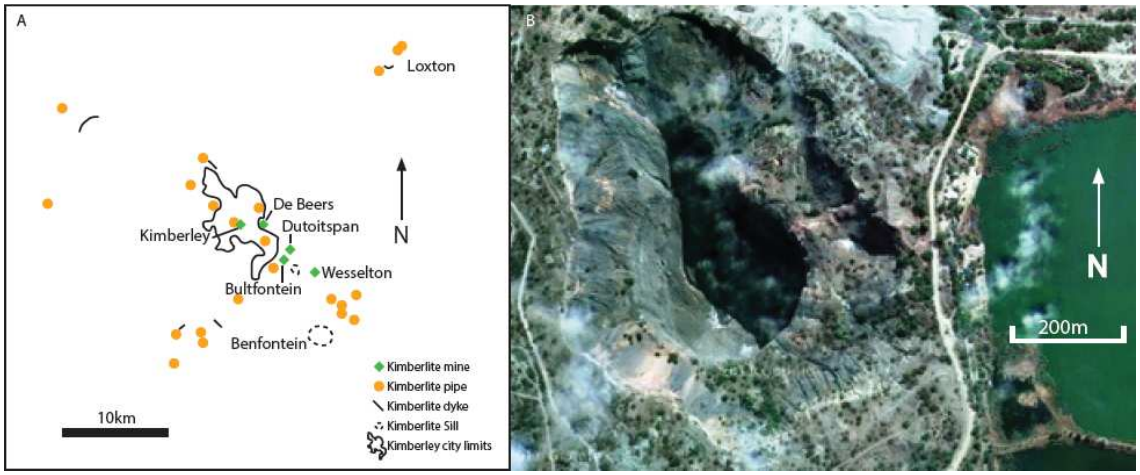

Figure 2.1: A - The area around Kimberley, modified after Field et al (2008), showing the location of kimberlite pipes and kimberlite mines. The samples in this study originate from the Bultfontein kimberlite mine. Kimberlites shown in green are the large mines; those in orange have undergone only small scale mining. B - A satellite image of the Bultfontein kimberlite pipe, coordinates: 28° 43' South and 24° 45' East *, South Africa (http://www.googleearth.com – accessed 19 September 2011).*

Ten xenoliths were taken from the Bultfontein mine dump for analysis (Table 3). Garnets were selected from the garnet bearing peridotites and these were examined to find melt inclusions and cracks. The best melt inclusion and totally embedded crack is dependent on their positioning within the grain (middle of a grain in the x-y directions and the z direction), to avoid any interference with surface cracks or polished surfaces of the garnet grains. The garnet grains were then placed in epoxy resin that is water-free then polished on both sides with paraffin to avoid water contamination. As these minerals are isotropic (Wenk and Bulak, 2004) they do not need to be orientated (Dowty, 1978). The thickness of the polished sections ranges between 226 and 263µm. These were then used for the analysis of OH^- analysis with synchrotron based FT-IR.

Table 3: The samples used for this study are displayed below.

Sample Name	**Major minerals**	**Accessory minerals**
KB1	Olivine, clinopyroxene, orthopyroxene, serpentine	Garnet, phlogopite, spinel
KB2	Olivine, clinopyroxene, orthopyroxene, serpentine, garnet	Phlogopite
KB3	Olivine, clinopyroxene, orthopyroxene, serpentine, garnet	
KB4	Olivine, clinopyroxene, orthopyroxene, serpentine	Garnet
KB5	Olivine, clinopyroxene, orthopyroxene, serpentine	Spinel
KB6	Olivine, orthopyroxene, serpentine	Garnet, clinopyroxene, phlogopite
KB7	Olivine, clinopyroxene, orthopyroxene, serpentine	Garnet, phlogopite
KB8	Olivine, clinopyroxene, serpentine	Orthopyroxene, phlogopite, pyrite
KB9	Olivine, clinopyroxene, orthopyroxene, serpentine	Garnet, phlogopite, spinel
KB10	Olivine, orthopyroxene, serpentine	Phlogopite, spinel

2.2 Analytical techniques

2.2.1 Optical microscopy

The microscope used in this study is an Olympus BX51, attached to a camera that is connected to a computer. This microscope has both a reflected and a transmitted light source. Figure 2.2 displays the microscope used in this investigation. The software used in obtaining photographs is Olympus Digital Imaging Solutions version 5.

Figure 2.2: Image displaying the optical microscope used in this study.

2.2.2 Scanning Electron Microscope (SEM)

Scanning electron microscopy involves the bombardment of the sample with electrons, causing an excitement of elements on the surface. This method can be used for both physical and chemical properties, namely: topography imaging and mineral chemistry. These two imaging methods are: secondary electron (SE) used to examine topography and back scatter electrons (BSE) used to examine element

distribution. This project was conducted using the back scatter electrons to analyse the composition of the minerals present.

The instrument also has two types of detectors: EDS (energy dispersive x-ray spectroscopy) and WDS (wavelength dispersive x-ray spectroscopy). EDS collects data from the sample in the form of energy and is less accurate than WDS. WDS detects the data in the form of wavelength which is more accurate. The instrument used in this analysis is a Jeol JSM 6610 with beam settings of 50nA and 20keV and standards that are displayed in Table 4.

Table 4: WDS analytical results for the minerals used as standards in this study. Taken from the standard: Astimex MINM25-53 + FC.

Mineral	Element	Quantity wt%	Mineral	Element	Quantity wt%
Diopside $MgCaSi_2O_6$	MgO	18.62	**Olivine $(Mg,Fe)_2SiO_4$**	MgO	50.43
	Al_2O_3	0.09		SiO_2	41.58
	SiO_2	55.37		MnO	0.10
	CaO	25.73		FeO	7.51
	TiO_2	0.08		NiO	0.38
	MnO	0.05			
	FeO	0.05			
Pyrope garnet $Mg_3Al_2Si_3O_{12}$	MgO	19.33	**Biotite $K(Mg,Fe)_3AlSi_3O_{10}(OH)_2$**	H_2O	4.11
	Al_2O_3	21.32		MgO	19.52
	SiO_2	41.45		Al_2O_3	15.13
	CaO	4.65		SiO_2	38.72
	TiO_2	1.16		K_2O	9.91
	Cr_2O_3	0.58		CaO	0.10
	MnO	0.27		TiO_2	1.77
	FeO	11.15		MnO	0.04
				FeO	10.72

2.2.3 Fourier Transform Infrared (FT-IR) spectroscopy

FT-IR spectroscopy is a form of analysis that involves the bombardment of a sample with an infrared beam that causes the vibration of bonds between atoms (Figure 2.3). The vibration motion forms a vibration spectrum with spectral bands that can be characterised by its amplitude and frequency (Dilek et al., 2009).

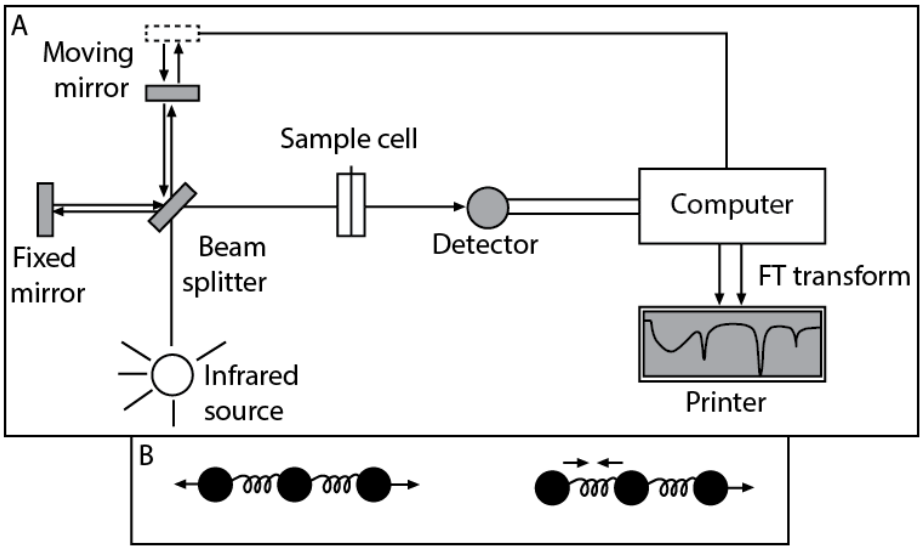

Figure 2.3: A- Image illustrating the inner workings of the FT-IR. B – Examples of the vibrations that occur when a sample is bombarded with an IR laser. Modified after Pavia et al. (2008).

The infrared region is subdivided in three zones, near- (1.0 – 5.2 µm), mid- (8 – 25 µm), and far (25 – 1000 µm) infrared. The mid-infrared region is used for primary molecular vibrations and all molecules present a characteristic absorbency peak or set of peaks (a fingerprint) (Dilek et al., 2009). The reason for choosing a synchrotron based FT-IR instead of a conventional FT-IR is the spot size: the resolution of a conventional FT-IR is typically 50µm and of the synchrotron based FT-IR is between 3 and 6 µm. The size of the beam spot of the infrared synchrotron (ANKA) is dependent on the wavelength. The defect structures and the inclusions

are approximately 40 μm in size thus the data quality is greater under the resolution of the synchrotron based FT-IR.

The FT-IR spectroscopy in the transmitted-light mode was used to investigate the garnet crystals with the totally embedded cracks and melt inclusions. The range of the IR absorption was acquired from 600 to 10 000cm^{-1} at the infrared beamline of the ANKA synchrotron with incident light polarized along *a*, *b* and *c* axes using a Bruker IFS 66v/S spectrometer coupled to an IRscopeII microscope with a x36, 0.5 N.A. Schwarzschild objective and a liquid N_2-cooled MCT detector.

The garnet samples were at first measured with an internal thermal Globar source in order to check the sample preparation quality using an aperture of 50μm. The average water concentration of this area was also determined from these measurements. Higher spatial resolution was achieved using brilliance advantage of the synchrotron light instead of the conventional sources (small sample areas and high beam intensity measurements). A grid pattern with blocks of 2μm by 2μm in size was used in order to create overlapping of the beam to make sure all areas are analysed. Apertures of 8 and 6μm were placed in the incoming and out coming beam, respectively in order to create a confocal arrangement. This then physically constrained the spot size to a range of 3 to 6μm. The workstation was placed in an enclosed plastic box to avoid volatile contamination. This plastic box is purged with dry N_2 in this prevention and the humidity in the box ranges between 1.2 and 1.8.

3 Results

3.1 Petrographic descriptions

Table 5 displays modal percentages of each mineral in the thin sections of the studied samples. The modal percentage was determined by point counting with totals of 2000 counts per section. Many grains and grain boundaries are serpentinised but due to the fact that the serpentine grains appear consolidated, this may obscure the results. The percentages in table 5 are displayed in a ternary diagram in figure 3.1, described in the introduction, classifying the rocks into harzburgites, lherzolites and wherlites. As mentioned in the introduction, the garnets can be separated into G10 and G9 garnets. The garnets' chromium and calcium compositions from the samples are displayed in figure 3.2 and show that only KB1 is a harzburgite, the other samples are lherzolites.

Table 5: The modal percentages of the minerals in all the studied samples using point counting.

	KB1	KB2	KB3	KB5	KB6	KB7	KB8	KB9	KB10
Olivine	40	35	40	45	60	49	48	36	38
Orthopyroxene	17	25	25	28	17	20	2	32	20
Clinopyroxene	18	15	10	10	5	10	30	3	10
Garnet	5	9	10	0	5	5	0	2	0
Serpentine	17	15	15	15	10	15	10	17	30
Spinel	1	0	0	2	0	0	0	2	2
Phlogopite	2	1	0	0	3	1	10	8	0
Ore minerals	0	0	0	0	0	0	Trace	0	0
Total	100	100	100	100	100	100	100	100	100

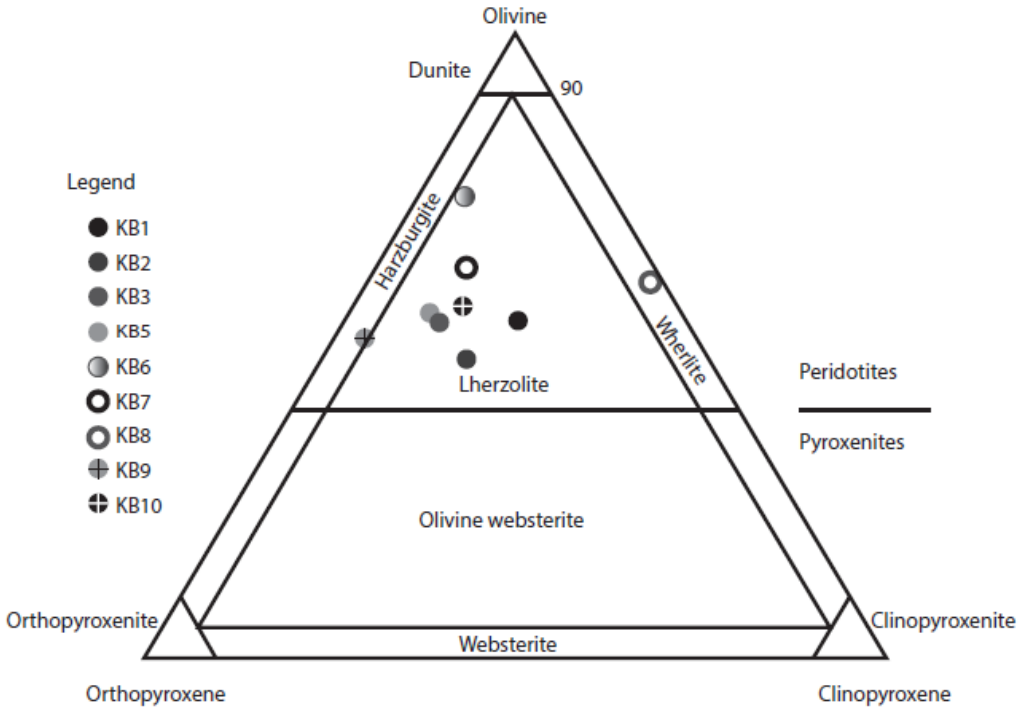

Figure 3.1: Ternary diagram used to classifying peridotites and pyroxenites. (modified after Streckeisen, 1976).

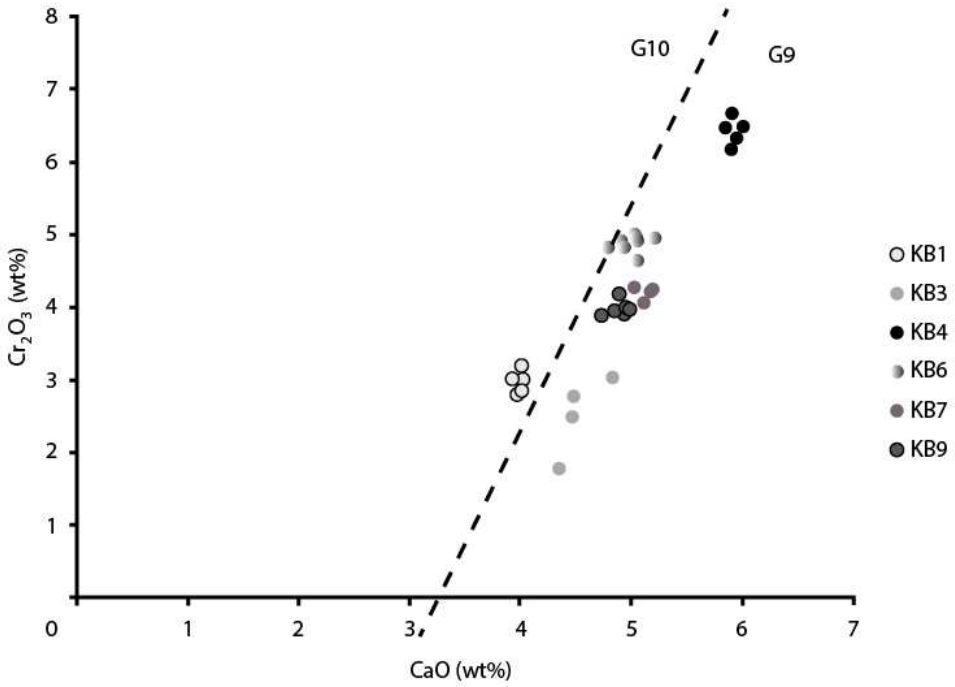

Figure 3.2: Modified after Gurney (1984), representing the difference between harzburgite and lherzolite garnets.

According to terminology defined by Best (2003), the observed samples are holocrystaline suggesting ample time for cooling with phaneritic, coarse-crystalline texture. The samples consist of euhedral, subhedral and anhedral crystals, thus making them hypidiomorphic (terminology taken from Best, 2003).

The microscopic images displayed in figure 3.3 below consist of an image on the left taken under plain polarised light and an image on the right, which is the same view, taken under crossed polarized light.

During this microscopic analysis of thin sections, the following alteration reactions were observed:

$Mg_2SiO_4 + H_2O \leftrightarrow Mg_3Si_2O_5(OH)_4$

olivine + $H_2O \leftrightarrow$ serpentine

$Mg_2Si_2O_6 + H_2O \leftrightarrow Mg_3Si_2O_5(OH)_4$

orthopyroxene + $H_2O \leftrightarrow$ serpentine and

$CaMgSi_2O_6 + H_2O \leftrightarrow Ca_2MgAl_2(SiO_4)(Si_2O_7)(OH)_2.H_2O$

clinopyroxene + $H_2O \leftrightarrow$ pumpellyite

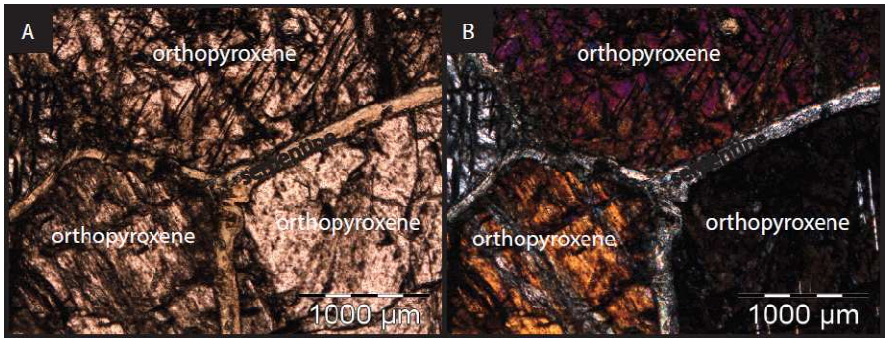

Figure 3.3: A (plain polarized light) and B (cross polarized light) - Euhedral orthopyroxene crystals in a triple junction from KB2. Serpentine rims the minerals.

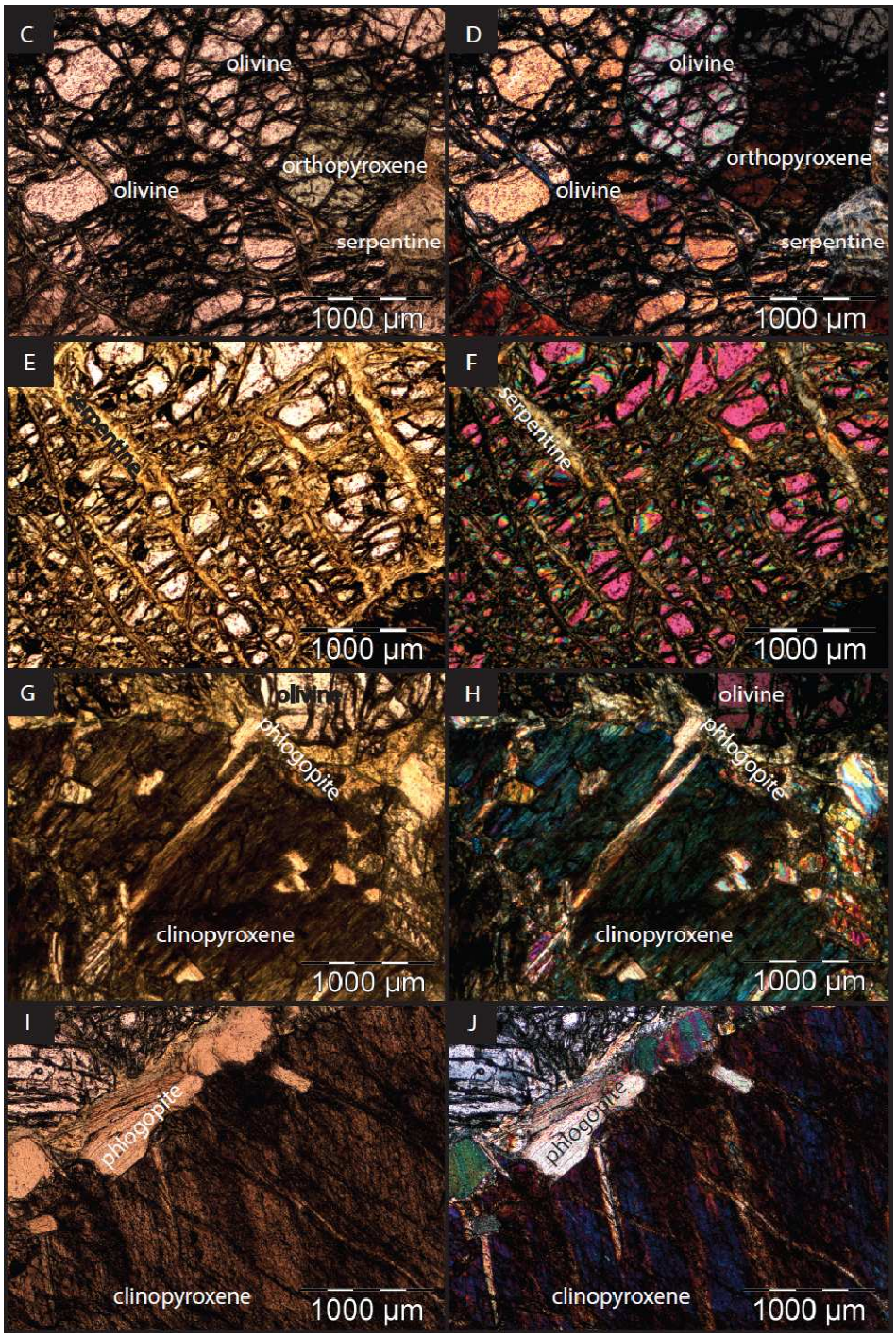

Figure 3.3 (continued): C (plain polarized light) and D (cross polarized light) - Disseminated texture of the minerals, as well as the anhedral form of olivine and orthopyroxene in sample KB3. E (plain polarized light) and F (cross polarized light) - The extensive serpentization of anhedral olivine within KB8. G (plain polarized light) and H (cross polarized light) - Reaction rim of phlogopite surrounding an altered clinopyroxene in sample KB8. I (plain polarized light) and J (cross polarized light) – Another reaction rim of euhedral phlogopite surrounding an altered clinopyroxene found in sample KB8.

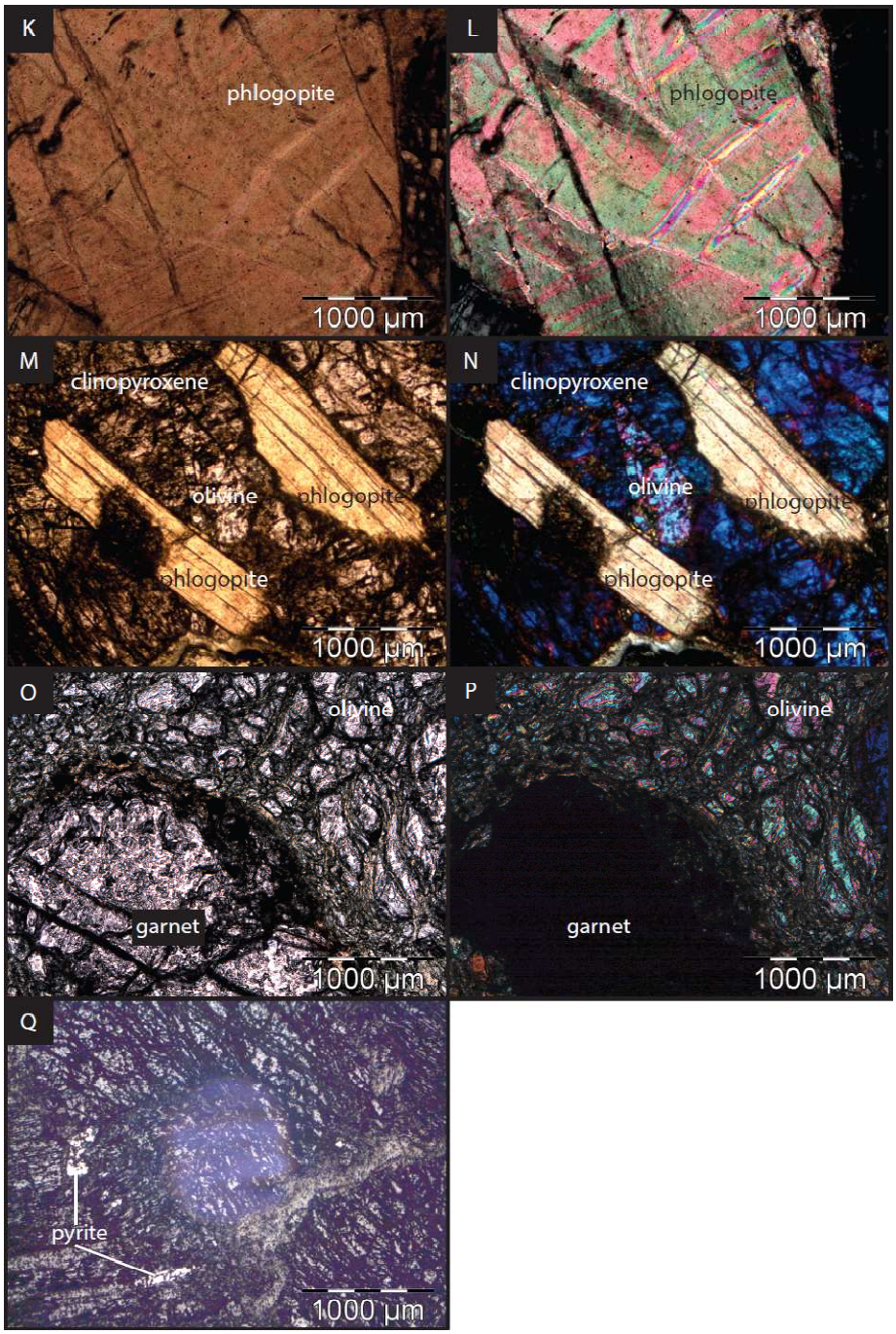

Figure 3.3 (continued): K (plain polarized light) and L (cross polarized light) - An image of phlogopite in sample KB1. Observed here is the light brown colour of the phlogopite under plain polarized light as well as the high birefringence on the right can be observed. M (plain polarized light) and N (cross polarized light) - Euhedral phlogopite and olivine engulfed in clinopyroxene, reaction between the clinopyroxene and phlogopite is evident. Taken from sample KB9. O (plain polarized light) and P (cross polarized light) - The dissolution of garnet to spinels, displaying a reaction rim. From sample KB1. Q (plain polarized light) - Reflective light used to observe ore minerals. Pyrite shows an anhedral crystal structure. Taken from sample KB8.

3.2 Microtextures

Yardley (1989) writes that reaction rims, as seen in figures 3.4A, 3.4B and 3.4C, are evidence of an incomplete reaction where there are zones of product mineral and reactant mineral. This author also reports that this texture forms in coarse grained rocks that underwent a metamorphic episode where the diffusion that took place was over a limited distance. Corona texture is a reaction rim that is well formed. Yardley (1989) also mentions they involve a rim of metamorphic mineral with an igneous mineral core and develop due to an interaction of two original minerals that reacted to form the rim. The reason for the reaction rim in figure 3.4C not being a corona texture is the alteration of the olivine and the garnet to phlogopite and not only involving the garnet.

The phlogopite presents evidence of an Al-, Ti- and K-rich, hydrous silicate melt (Lloyd et al., 1991). In figure 3.4A the phlogopite formed due to the breakdown of clinopyroxene and olivine along with the above mentioned mantle metasomatism. Similar scenarios are found in figure 3.4B and 3.4C, where garnet and olivine break down to form phlogopite, with the metasomatic and kimberlitic components. Components within the phlogopite that are not present in either olivine or clinopyroxene, originate from the kimberlitic melt.

The following equations represent the reactions that take place during these processes:

In figure 3.4A

$CaMgSi_2O_6 + Mg_2SiO_4 + H2O + \text{kimberlitic component} \leftrightarrow KMg_3AlSi_3O_{10}(OH)_2$

clinopyroxene + olivine + H_2O + kimberlitic component ↔ phlogopite

In figure 3.4B and 3.4C

$$Mg_3Al_2Si_3O_{12} + Mg_2SiO_4 + H_2O + K^+ \text{ rich fluid} \leftrightarrow KMg_3AlSi_3O_{10}(OH)_2$$

Garnet + olivine + H_2O + K^+ rich fluid ↔ phlogopite

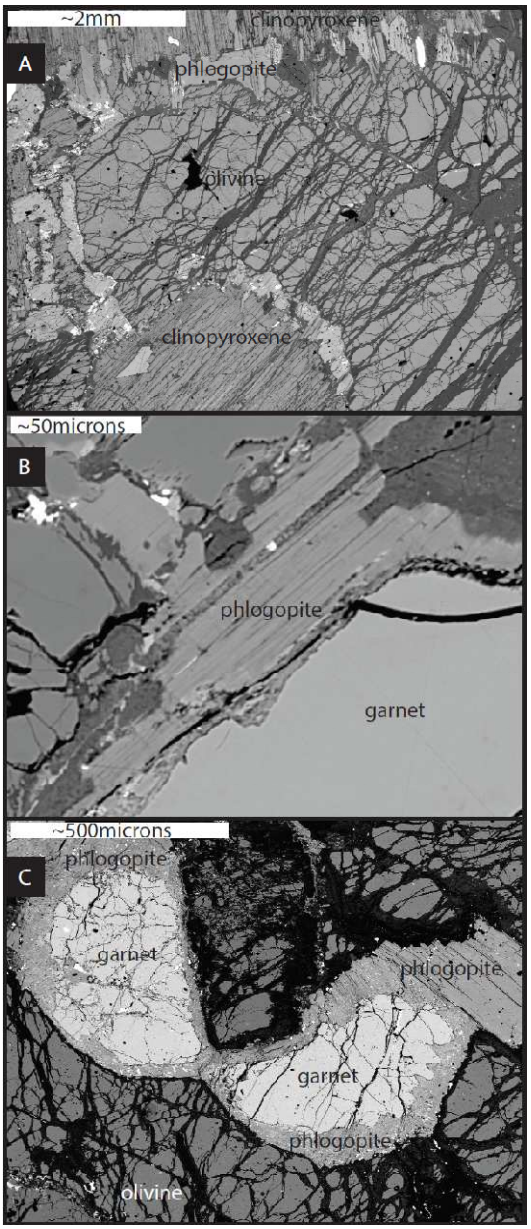

Figure 3.4: A - Backscatter electron image of a reaction rim of phlogopite surrounding clinopyroxene found in sample KB8. B - Backscatter electron image of a reaction rim of phlogopite surrounding a garnet grain in sample KB6. C - A backscatter electron image of a reaction rim found within sample KB9 of phlogopite surrounding garnet.

3.3 Microstructures

3.3.1 Exsolution blebs

Exsolution is the separation of a crystal that is homogenous into domains that have different compositions, which is caused by the attraction of atoms that are alike (Wenk and Bulak, 2004). Diffusion is required in order for this process to occur. In general, cooling in most metamorphic and igneous rocks will result in exsolution microstructures, but in ultra high pressure minerals, exsolutions are likely formed due to decompression when travelling from a depth of over 100 km to the surface (Liu et al., 2007). During decompression, an initial pyroxene (homogenous) might exsolve into diopside (Ca^{2+} rich) and enstatite or pigeonite (Ca^{2+} poor), which is observed in figure 3.5 (Wenk and Bulak, 2004). Due to the fact that these minerals are high pressure, an assumption can be made that this texture formed due to decompression during uplift.

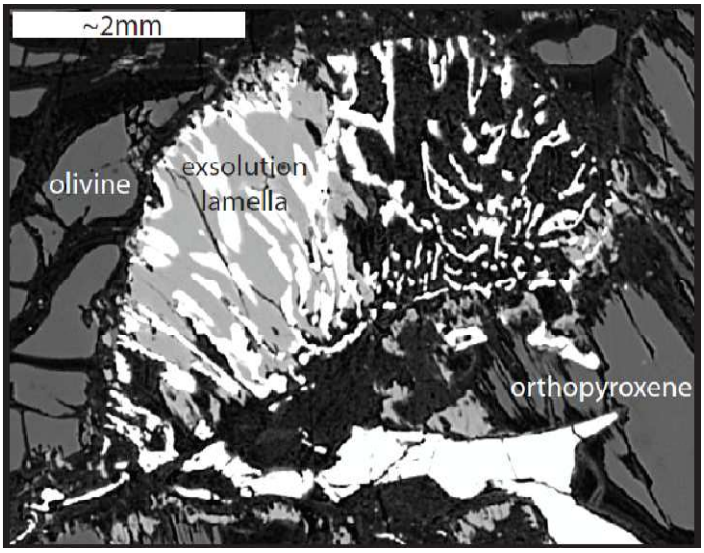

Figure 3.5: Exsolution blebs found in sample KB5. The lighter lamellae are clinopyroxene and the duller grey lamellae are orthopyroxene.

3.3.2 Hydraulic fracturing and fractures

Yardley (1989) discusses that fluid pressure is the pressure that a fluid exerts along grain boundaries or in pores and in the scenario where fluid pressure is absent, lithostatic pressure holds grains together, making failure difficult. This author also mentions that when a fluid and fluid pressure is present, cracking is more likely to occur. If the fluid pressure is greater than the lithostatic pressure, more than the rocks tensile strength, then the rock will burst owing to a process called hydraulic fracturing (Figure 3.6A and 3.6B), where the fluid uses cracks to escape (Norris and Henley, 1976). The rock then cools, the fluid pressure will decrease as the minerals react with the remaining fluid (Yardley, 1981). In the samples of this study the hydration results in serpentine that forms from olivines and occasionally from orthopyroxenes.

Park (2005) describes fractures as a crack where consistency is lost and is regarded as a plane of discontinuity. This author also mentions that when displacement occurs and the one block moves relative to the other side along a fracture, then it is known as a fault. Another definition from this author is on joints, which is a fracture where the displacement is either non-existent or too small to be noticed or only slight parting. Figure 3.6C displays fractures that propagate across two grains; the first is an orthopyroxene and the other an olivine grain (despite the common fracture found within olivine grains). These fractures do not display displacement and are thus joints. They occurred after crystallization and may be due to the decompression during uplift.

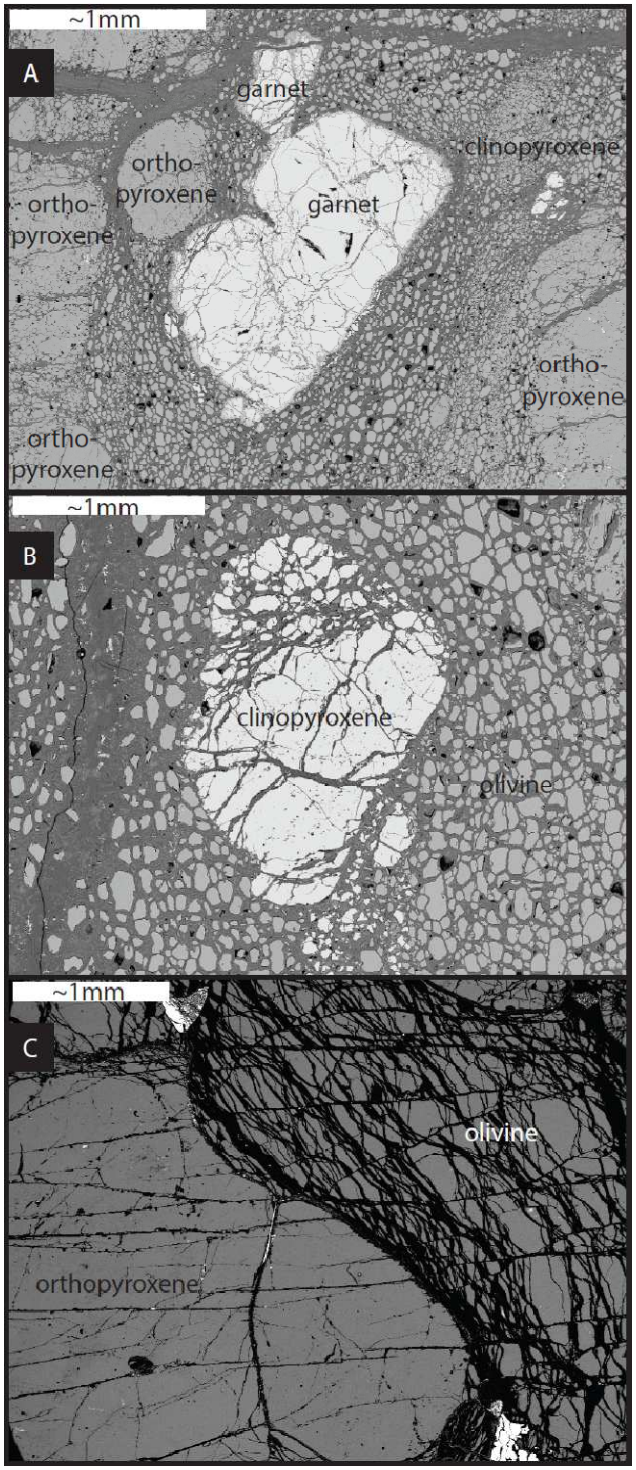

Figure 3.6: A - Backscatter electron image of sample KB4 displaying the extent of hydration during hydraulic fracturing. B - Another backscatter electron image from sample KB4 displaying serpentinization due to hydration and hydraulic fracturing. C - Backscatter electron image found within sample KB5, showing joints across two minerals.

3.4 Mineral chemistry

3.4.1 Olivine

Table 6 shows the average compositions of different olivine grains within each of the different peridotite samples described in this study, with the individual analyses given in appendix 1. Figure 3.7 is the graphical representation of the averages in table 6, to allow for clarity on the variations the values were normalized to 100. This figure also displays a literature example taken from Varne (1970) where analysis was carried out on an electron microprobe. Due to the fact that variation is slim, suggesting either little or no alteration or alteration of the same magnitude of metamorphism for all the samples during incorporation into the kimberlite magma and the ascent process. In figure 3.8 olivines were plotted on a forsterite-fayalite diagram, from which they classified as forsterite (Fo_{85-90}).

Table 6: The average compositions of olivine grains within each of the studied samples. It can be observed that there isn't a great variation in composition of the different olivine grains. Values are in wt%.

	KB1	KB3	KB4	KB5	KB6	KB7	KB8	KB9	Varne (1970)	Overall average
SiO_2	40.88	42.31	41.76	42.16	41.76	41.42	41.38	41.44	40.47	41.51
TiO_2	0.01	0.03	0.01	0.03	0.03	0.02	0.01	0.02	0.00	0.02
Al_2O_3	0.00	0.00	0.00	0.00	0.00	0.04	0.00	0.01	0.00	0.01
Cr_2O_3	0.01	0.01	0.04	0.12	0.04	0.02	0.02	0.00	0.03	0.03
FeO	9.36	7.62	7.52	6.50	7.06	7.50	7.02	6.80	9.00	7.60
MnO	0.09	0.10	0.10	0.07	0.10	0.12	0.09	0.10	0.16	0.10
MgO	48.93	52.63	49.90	51.52	49.54	48.99	50.57	50.22	49.83	50.24
CaO	0.09	0.03	0.03	0.03	0.03	0.01	0.06	0.05	0.00	0.04
Na_2O	0.00	0.00	0.00	0.00	0.01	0.00	0.01	0.01	0.00	0.00
K_2O	0.01	0.02	0.01	0.04	0.03	0.04	0.01	0.04	0.00	0.02
Totals	99.38	102.75	99.37	100.48	98.60	98.16	99.18	98.69	99.49	99.57

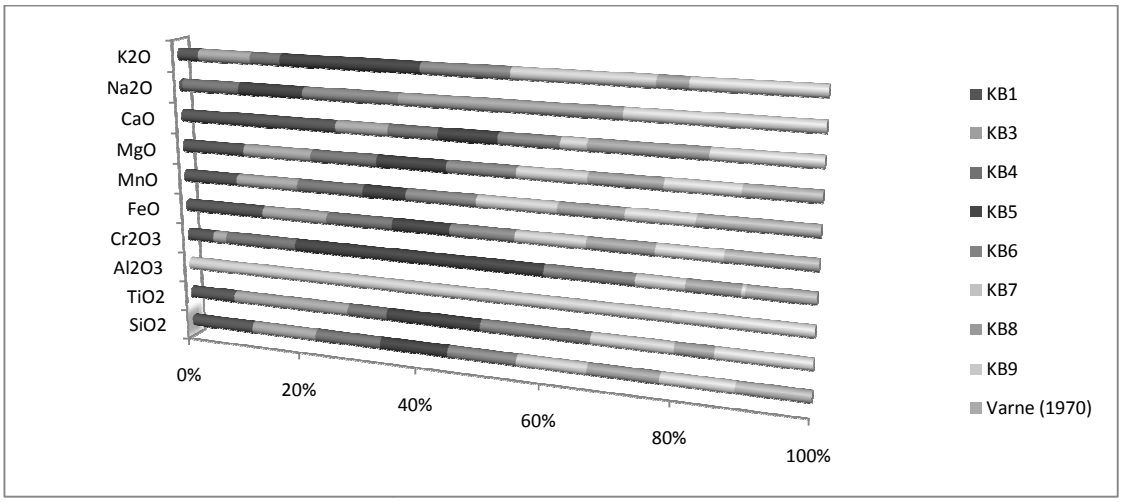

Figure 3.7: Graph displaying the average compositions found in table 6. There is minimal change in composition between the different samples.

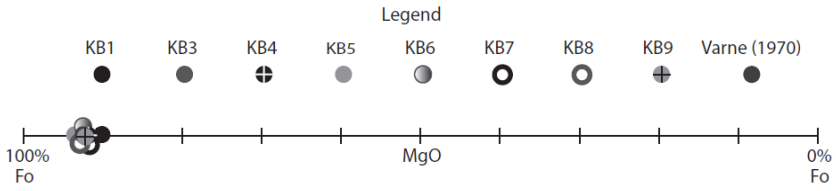

Figure 3.8: Binary diagram displaying the classification of the olivines in the samples. All the samples are magnesium-rich (Fo_{90-94}).

3.4.2 Clinopyroxene

The general formula for pyroxene is $XYSi_2O_6$, where for clinopyroxene the X is filled with larger atoms, such as Ca^{2+}, Na^{+} and Li^{+} and the Y position is filled with either Mg^{2+} of Fe^{2+} (Wenk, et. al., 2004). The average composition for the clinopyroxene grains from each sample is shown in table 7, where individual analyses can be found in appendix 1. It can be observed in figure 3.9 that KB5 varies in CaO composition and KB10 varies in Al_2O_3 composition. Gregoire et al. (2003) also did analysis on clinopyroxenes from peridotites which the average composition is used in this

diagram as a comparison; analysis was carried out using an electron microprobe. Figure 3.10 is a classification diagram for pyroxenes. This shows that they are either of diopside ($CaMgSi_2O_6$) or of endiopside (contains less CaO than diopside) composition, the magnesium rich members.

Table 7: Average compositions of the clinopyroxenes in each of the studied samples. Values are in wt%.

	KB1	KB2	KB3	KB4	KB5	KB6	KB7	KB8	KB9	KB10	Gregoire (2003)	Overall Average
SiO_2	54.96	54.55	55.85	55.14	55.00	54.22	54.63	53.92	54.23	55.20	54.84	54.77
TiO_2	0.07	0.02	0.19	0.17	0.03	0.56	0.05	0.19	0.33	0.18	0.12	0.18
Al_2O_3	2.09	2.17	1.76	2.02	1.45	2.99	2.00	1.50	1.99	0.61	2.79	1.86
Cr_2O_3	1.48	1.51	0.79	1.99	1.24	0.71	1.69	1.75	1.95	1.47	2.02	1.46
FeO	2.36	2.35	4.00	2.25	1.37	2.80	2.12	2.62	2.32	2.56	2.33	2.47
MnO	0.04	0.02	0.19	0.07	0.02	0.18	0.00	0.17	0.13	0.10	0.08	0.09
MgO	15.26	15.56	17.85	16.70	17.82	16.89	15.74	16.30	16.61	17.77	16.40	16.65
CaO	19.87	20.01	19.44	19.07	23.05	19.47	19.81	19.56	19.18	20.00	18.94	19.94
Na_2O	2.05	2.02	1.11	1.85	0.35	1.30	1.74	1.68	1.81	1.05	2.27	1.50
K_2O	0.01	0.02	0.00	0.02	0.03	0.07	0.00	0.06	0.03	0.03	0.03	0.03
Totals	98.19	98.22	101.19	99.28	100.36	99.19	97.77	97.75	98.57	98.97	99.81	98.95

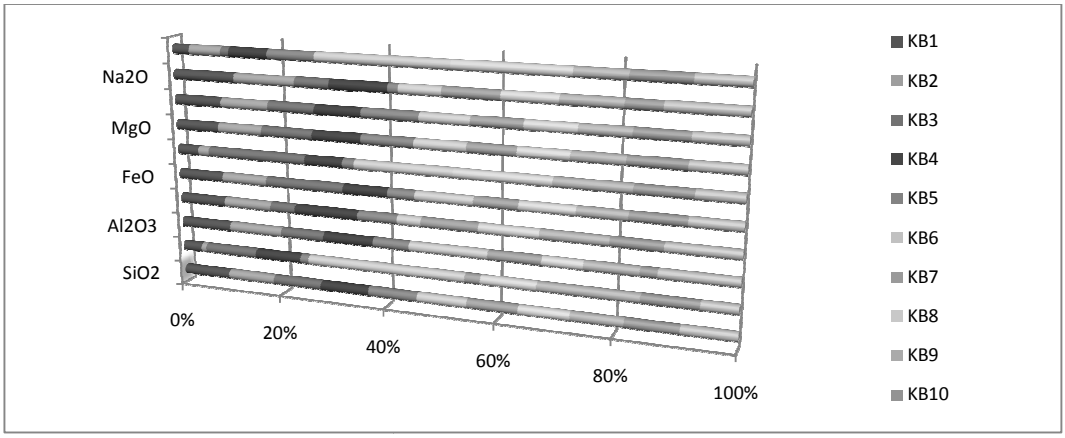

Figure 3.9: Graphical display of the average clinopyroxene composition in table 7. There are slight variations in compositions, such as the CaO content in KB5.

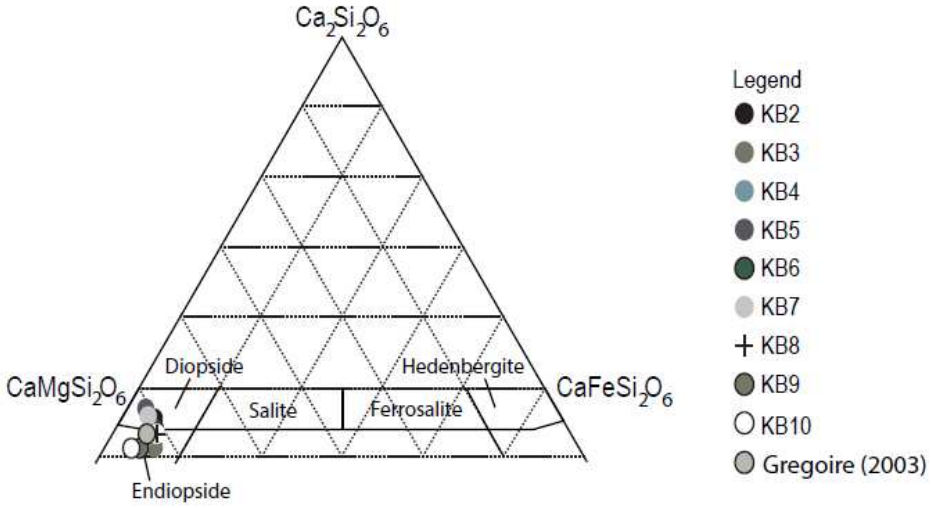

Figure 3.10: Classification diagram displaying the compositions of clinopyroxenes of the studied samples, classified as diopsides and endiopsides.

3.4.3 Orthopyroxene

The general formula for pyroxenes is $XYSi_2O_6$, where X and Y are filled with either Mg^{2+} and/or Fe^{2+}. They are split into ferrosillite (En_{0-49}) and enstatite (En_{50-100}), where enstatite is Mg^{2+} rich and ferrosillite is Fe^{2+} rich (Wenk et. al., 2004). Averages of the compositions of the orthopyroxene grains for each sample can be found in table 8 along with an overall average (Appendix 1 displays the individual analytical results). The graph in figure 3.11 displays these compositions, showing that the minerals compositions are very similar with only a slight variation in the Al_2O_3 content. Average orthopyroxene composition (Varne, 1970) is also displayed in this graph for comparison purposes, analysis carried out using an electron microprobe. Figure 3.12 displays the compositions of the orthopyroxenes to be enstatite ($Mg_2Si_2O_6$), thus the magnesium-rich member.

Table 8: Average orthopyroxene compositions within each sample of study with the overall average for all the samples. Values are in wt%.

	KB1	KB2	KB3	KB4	KB5	KB6	KB7	KB8	KB9	KB10	Varne (1970)	Overall average
SiO_2	57.52	58.42	58.74	59.14	58.09	58.88	58.31	59.50	58.35	56.45	55.95	58.34
TiO_2	0.04	0.00	0.02	0.06	0.04	0.02	0.03	0.04	0.02	0.04	0.00	0.03
Al_2O_3	0.45	0.32	0.42	0.50	2.07	0.52	0.69	0.18	0.36	3.06	1.36	0.85
Cr_2O_3	0.28	0.15	0.24	0.41	0.81	0.35	0.30	0.14	0.36	0.86	0.35	0.39
FeO	5.68	5.06	4.69	4.55	4.34	4.37	4.50	4.59	4.23	4.44	5.63	4.64
MnO	0.10	0.13	0.12	0.13	0.10	0.07	0.12	0.08	0.12	0.12	0.19	0.11
MgO	33.75	35.28	35.97	35.19	35.08	34.58	34.37	36.15	35.32	34.02	36.17	34.97
CaO	0.47	0.29	0.28	0.56	0.64	0.45	0.38	0.11	0.27	0.77	0.57	0.42
Na_2O	0.17	0.04	0.10	0.13	0.01	0.15	0.12	0.01	0.09	0.03	0.08	0.09
K2O	0.01	0.00	0.02	0.02	0.02	0.01	0.04	0.00	0.04	0.03	0.00	0.02
Totals	98.46	99.69	100.59	100.70	101.20	99.39	98.84	100.79	99.15	99.81	100.30	99.86

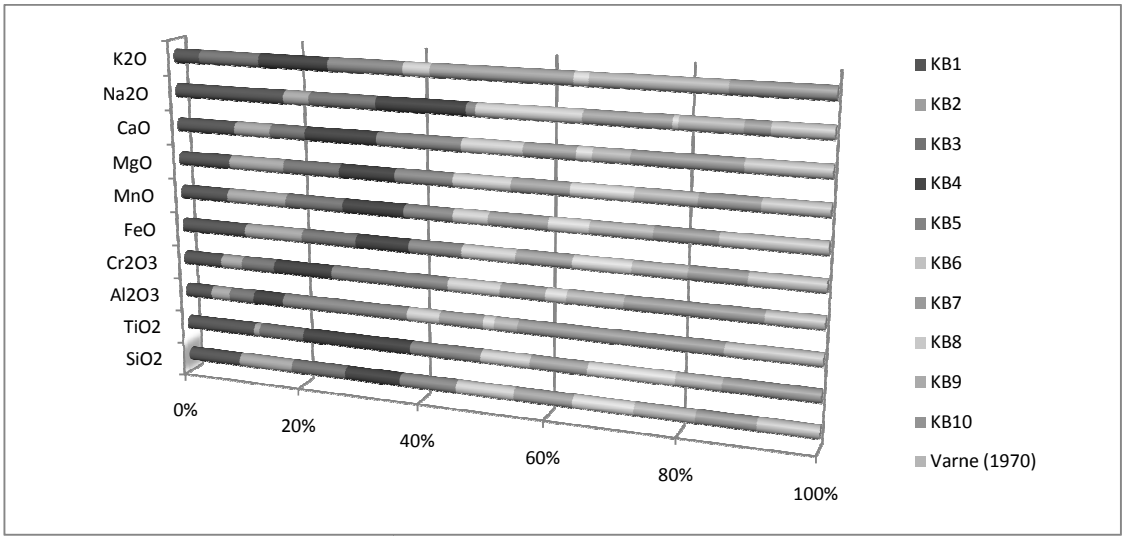

Figure 3.11: Graph representing the average compositions displayed in table 8 for orthopyroxene grains in each sample. There is only a variation in the Al_2O_3 content between the different samples all the other constituents are vary only slightly.

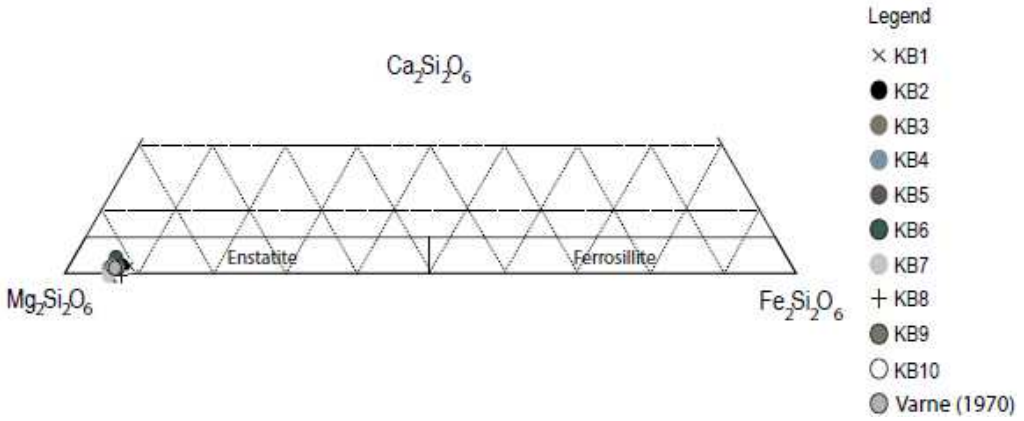

Figure 3.12: Ternary diagram displaying the classification of the orthopyroxenes found in the samples studied. All the orthopyroxenes are enstatites ($MgSiO_3$).

3.4.4 Garnet

Table 9 displays the average compositions of garnets from each sample that contained garnets. These values are then displayed in a graph in figure 3.13; this displays a difference in Cr_2O_3 and MgO composition. Average compositions of garnets were taken from Gregoire et al. (2003) as a literature comparison, analysis carried out using an electron microprobe. Figure 3.14 represents the composition of the garnets showing that they are all magnesium rich.

Table 9: The compositions of the garnets in the samples that contain garnets in the study. Values are in wt%.

	KB1	KB3	KB4	KB6	KB7	KB9	Gregoire (2003)	Overall average
SiO_2	42.57	42.62	42.25	42.20	41.84	41.90	41.85	42.18
TiO_2	0.14	0.06	0.11	0.06	0.08	0.07	0.21	0.10
Al_2O_3	21.54	21.85	18.90	19.92	20.34	20.67	21.14	20.62
Cr_2O_3	2.95	2.58	6.43	4.87	4.20	3.98	4.00	4.14
FeO	6.17	7.86	6.76	6.72	6.91	6.92	7.13	6.92

Table 9 (continued)

	KB1	KB3	KB4	KB6	KB7	KB9	Gregoire (2003)	Overall average
MnO	0.29	0.42	0.34	0.34	0.38	0.44	0.35	0.37
MgO	22.56	20.67	19.92	20.17	19.63	20.32	20.28	20.51
CaO	3.98	4.52	5.93	4.97	5.12	4.89	4.95	4.91
Na_2O	0.03	0.02	0.03	0.07	0.02	0.03	0.05	0.04
K_2O	0.03	0.03	0.02	0.01	0.00	0.02	0.00	0.02
Totals	100.27	100.64	100.68	99.33	98.52	99.24	99.94	99.80

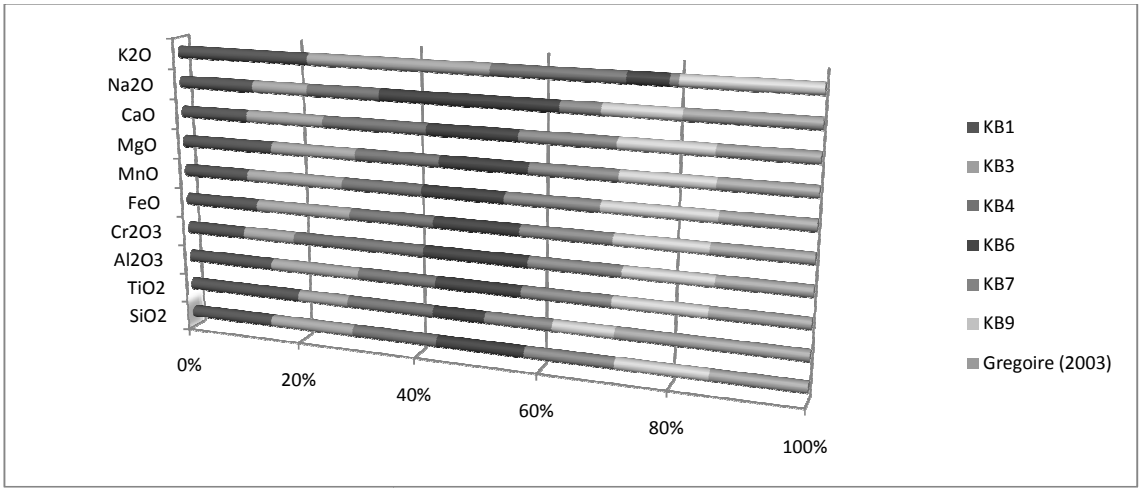

Figure 3.13: Graphic representation of table 9. The garnets seem to be of the similar compositions, with a slight variation in Cr_2O_3 and MgO composition.

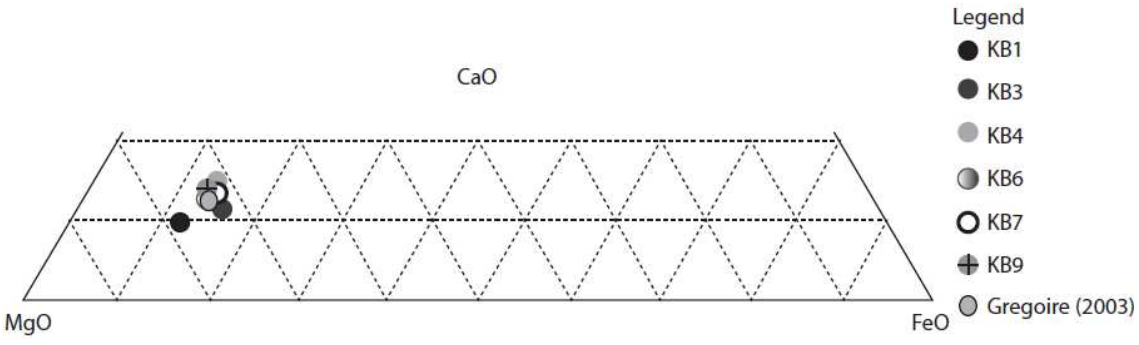

Figure 3.14: Ternary diagram showing the general composition of the garnets studied.

A feature commonly encountered in garnets, also in this study, is zoning, which can be defined as is the compositional variation from the core to the rim of the crystal (Wenk and Bulak, 2004). Different types of zoning can occur, namely: concentric-, sector-, growth- and diffusion zoning. Line measurements with SEM WDS were taken from rim to rim across garnets in the thin sections of the garnet bearing lherzolites. Below are graphs (Figure 3.15–3.18) showing this analysis, specifically of the Mg^{2+}, Fe^{2+}, Mg# [Mg/(Mg+Fe)] and Ca^{2+}. Enrichment in Mg^{2+} implies high temperature crystallisation, whereas Fe^{2+}-enrichments implies crystalisation at low temperatures, according to Bowen's reaction. An increase in Fe^{2+} will result in a decrease in Mg^{2+} and vise versa, owing to the same occupancy sight in the crystal lattice and thus implying a decrease in temperature. Ca^{2+} occupies points in the lattice at high pressures and will decrease in quantity in the lattice as the pressure decreases.

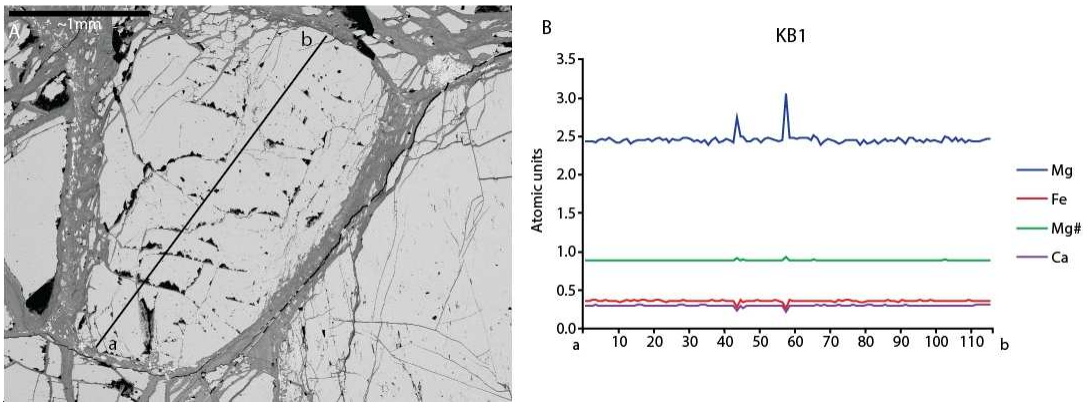

Figure 3.15: A – Backscatter electron image of the garnet crystal found in sample KB1, where the line 'ab' is the line on which the analysis displayed in B was taken. B – Graphical display of the line measurement, indicating the homogeneity of the studied garnet with only occasional slight peaks.

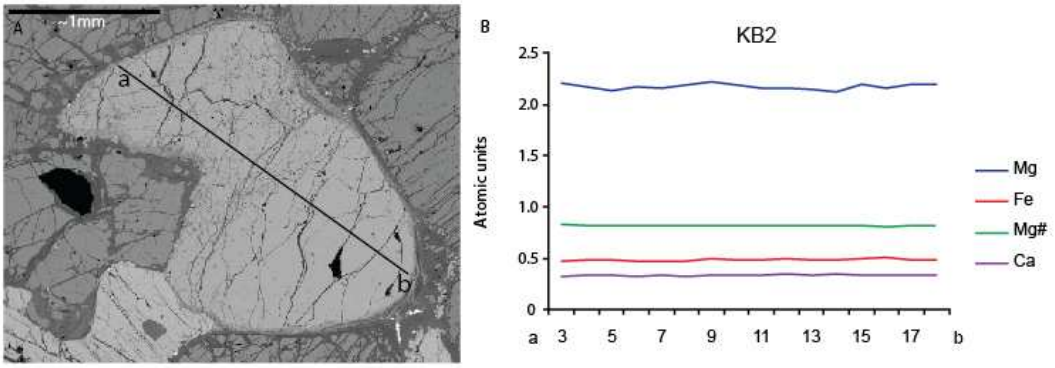

Figure 3.16: A – Displays a backscatter image of the garnet crystal found in sample KB2. The line 'ab' is the line along which analysis took place to investigate possible zoning. B – A graphical display of the line measurements, indicating homogenous garnet crystal.

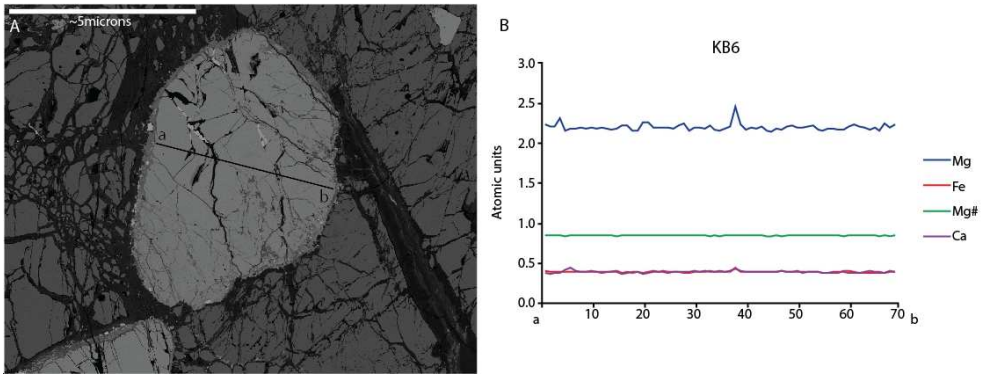

Figure 3.17: A – Backscatter electron image of a garnet crystal in sample KB6. Analysis took place along the line 'ab' to investigate for zoning. B – A display of results of the line measurements, proving an almost homogenous garnet.

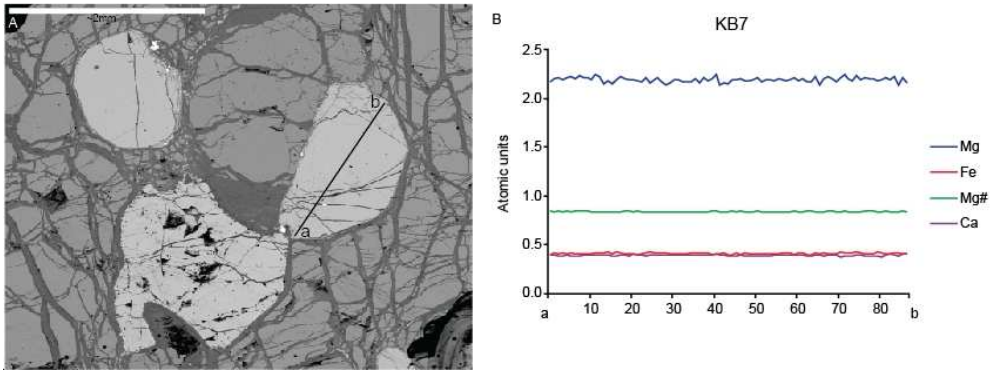

Figure 3.18: A – A backscatter electron image of a garnet crystal in sample KB7 that was analysed along the line 'ab'. B – Display of the line measurements, indicating no zoning.

3.4.5 Biotite

Biotite grains were found in samples KB3, KB4, KB6, KB8 and KB9. The theoretical end members in the group include: phlogopite [$KMg_3AlSi_3O_{10}(OH,F)_2$], siderophillite [$KFe_2^{2+}AlAl_2Si_2O_{10}(OH,F)_2$] and annite [$KFe_3^{2+}AlSi_3O_{10}(OH,F)_2$] (Wenk and Bulak, 2004). The biotites found in these samples all lean towards the Mg^{2+} end member, phlogopite due to the fact that the grains contain more Mg than Fe. Table 10 displays the average chemical compositions from SEM WDS for biotites from each sample. Note that none of the results add up to 100% due to the fact that water content couldn't be measured. The compositions are displayed graphically in figure 3.19. Individual analyses of the biotite grains can be found in Appendix 1.

Table 10: Average composition of phlogopite minerals found within the samples. Values are in wt%.

	KB3	KB4	KB6	KB8	KB9	Overall average
SiO_2	40.27	35.25	40.94	41.01	40.51	39.60
TiO_2	0.66	0.22	1.01	0.71	0.91	0.70
Al_2O_3	14.50	12.03	13.22	13.52	13.78	13.41
Cr_2O_3	1.57	3.76	1.56	1.20	1.57	1.93
FeO	3.32	6.26	2.92	2.58	2.61	3.54
MnO	0.06	0.08	0.07	0.06	0.06	0.07
MgO	23.70	27.72	23.43	24.27	23.93	24.61
CaO	1.99	0.77	0.07	0.05	0.06	0.59
Na_2O	1.69	0.92	0.43	1.03	0.82	0.98
K_2O	6.88	2.64	9.93	8.97	9.33	7.55
Totals	94.64	89.64	93.58	93.40	93.59	92.97

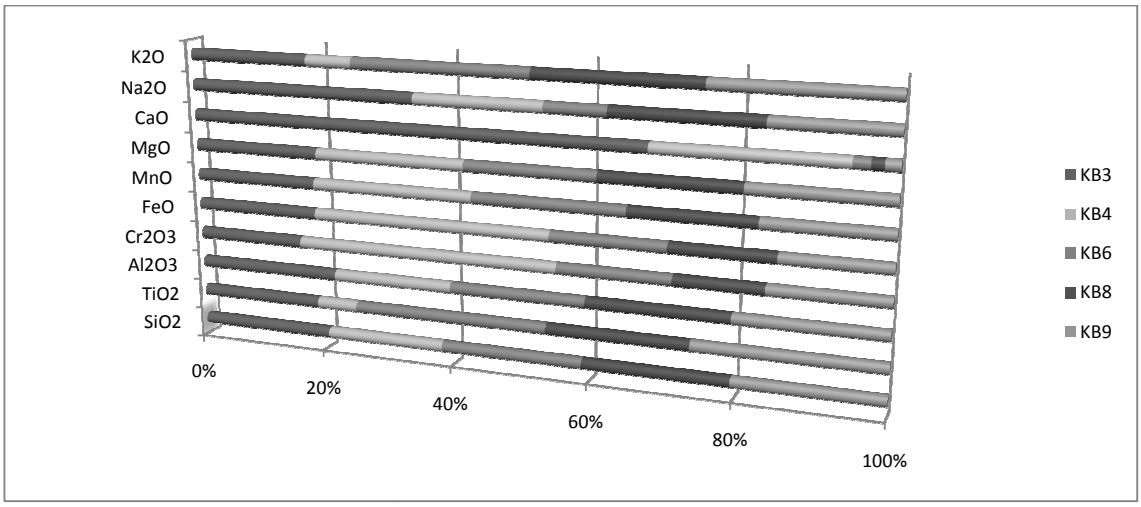

Figure 3.19: Graphic display of the compositions in table 10. It can clearly be viewed that there is a variation in chemical compositions between samples.

3.4.6 Amphibole

Table 11 displays the results of SEM WDS analyses on the amphibole grains found in sample KB3. Figure 3.20 is a graph which compares the overall average to a literature composition taken from Varne (1970). The classification of the amphiboles is shown below in figure 3.21, all plotted as the amphibole tschermakite. Appendix 1 shows all individual chemical analysis.

Table 11: Average amphibole composition in sample KB3. Values are in wt%.

	KB3_AM11	**KB3_AM13**	**KB3_AM14**	**KB3_AM15**	**KB3_AM16**	**KB3_AM17**	**Varne (1970)**	**Overall average**
SiO_2	46.49	47.28	44.22	44.80	46.50	45.99	44.73	45.72
TiO_2	0.26	0.27	0.45	0.60	0.17	0.35	0.29	0.34
Al_2O_3	13.98	11.98	13.44	12.87	15.19	12.99	12.58	13.29
Cr_2O_3	1.98	2.08	1.64	1.83	2.11	2.03	2.43	2.01
FeO	3.43	3.68	4.35	3.97	3.61	3.22	3.47	3.68
MnO	0.00	0.06	0.07	0.11	0.11	0.00	0.11	0.07

Table 11 (continued)

	KB3_AM11	KB3_AM13	KB3_AM14	KB3_AM15	KB3_AM16	KB3_AM17	Varne (1970)	Overall average
MgO	19.93	20.14	18.89	18.49	20.01	20.00	19.17	19.52
CaO	8.99	9.18	11.68	11.31	8.58	9.13	10.95	9.97
Na_2O	3.88	4.15	3.34	3.39	3.88	3.70	3.84	3.74
K_2O	0.91	1.03	0.77	0.85	0.76	1.05	0.43	0.83
Total	99.86	99.86	98.86	98.21	100.92	98.46	98.00	99.17

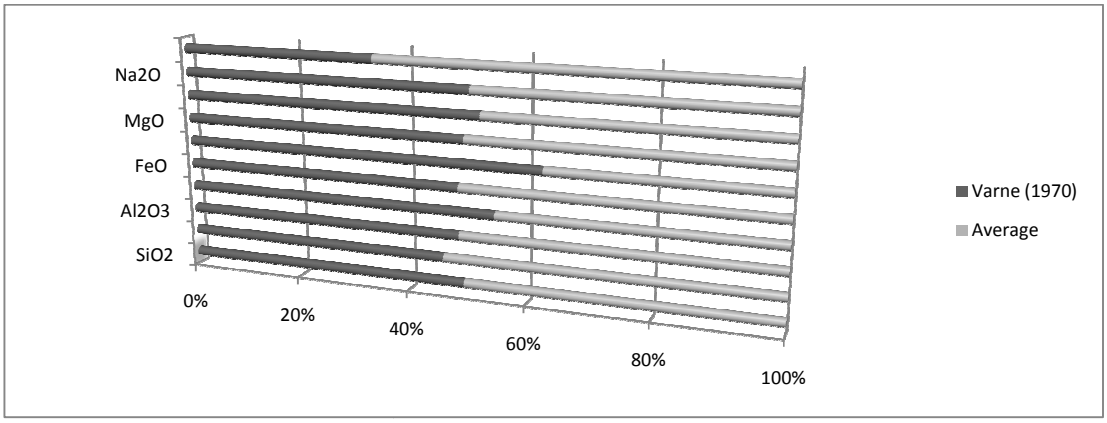

Figure 3.20: Graphic display of the overall average and literature compositions in table 11. There are only slight composition variations.

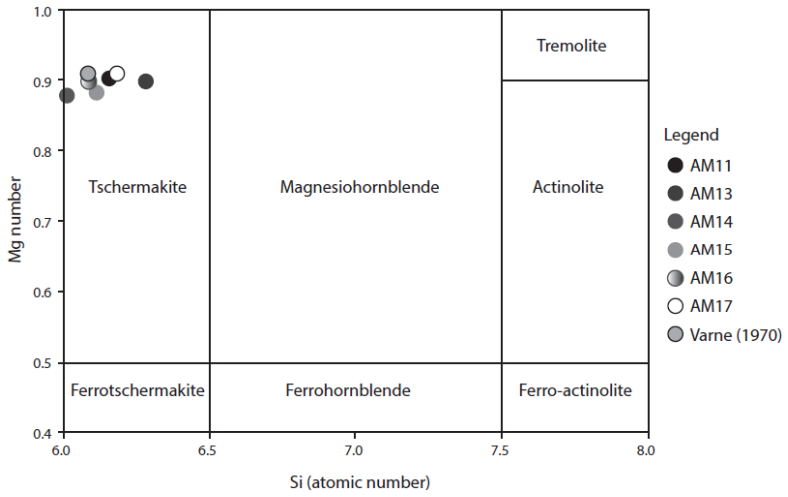

Figure 3.21: Classification diagram of amphiboles after Meeker et al. (2006). This classifies them all as tschermakites.

3.5 Geothermobarometry

3.5.1 Garnet-biotite geothermometry

Figure 3.22 and figure 3.23, show backscatter electron images of coexisting garnet and orthopyroxene grains. Points A through F indicate the points of SEM WDS analysis, the results of which were plotted in figure 3.24 and 3.25 to determine the temperature and pressure of the last metamorphic event experienced by the peridotites. Figure 3.22 is an image from sample KB6 with a K_D value ($K_D = \left\{\frac{Fe}{Mg}\right\}^{ga} / \left\{\frac{Fe}{Mg}\right\}^{bt}$) between points A (result KB6Bt30 in appendix 1) and B (result KB6Gt30 in appendix 1) of 0.374082. Figure 3.23 is an image from sample KB9 with a K_D value ($K_D = \left\{\frac{Fe}{Mg}\right\}^{ga} / \left\{\frac{Fe}{Mg}\right\}^{bt}$) calculated from the average of A – D for garnet (results KB9Gt10, KB9Gt2, KB9Gt1 and KB9Gt3 respectively, in appendix 1) and the average of E and F for biotite (results KB9Bt4 and KB9Bt5 respectively, in appendix 1), with a result of 0.335606.

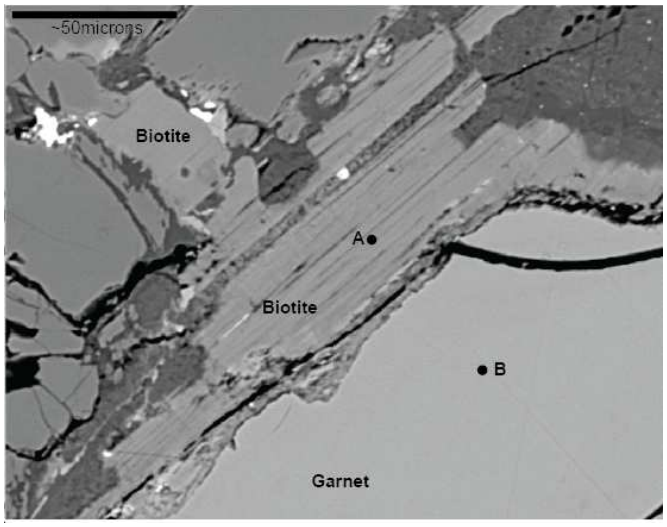

Figure 3.22: Backscatter electron image from KB6 which displays consecutive biotite and garnet grains which analysis (A and B) is used to determine the K_D value and then the temperature of formation, observed in figure 3.24.

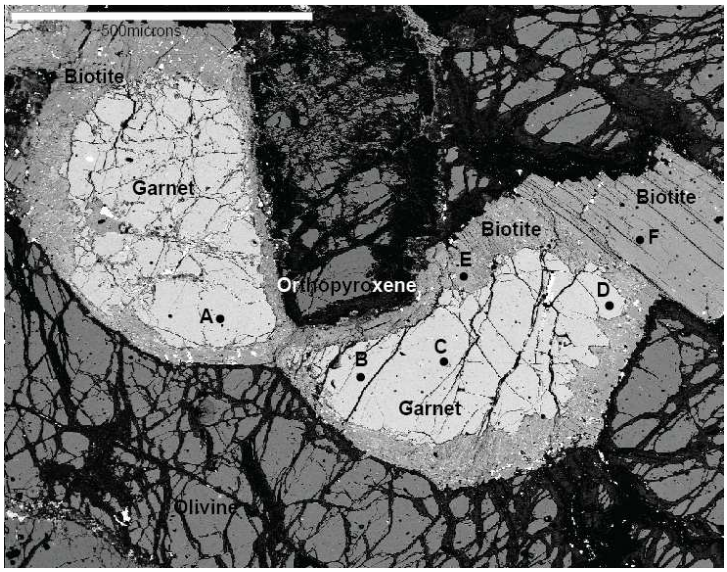

Figure 3.23: Backscatter electron image from KB9 which displays consecutive biotite and garnet grains. The average of the analysis A – D were used for the garnet values to determine the K_D and average of the analysis E and F were used as the values for biotite.

Figure 3.24 is a plot of K_D vs. T (K), with reference values taken from Dasgupta et al. (1991) creating a trend line. On this trend line the K_D values for KB6 and KB9 were plotted, from which the temperatures 1205 K for KB6 and 1145 K for KB9 could be read off.

Figure 3.25 is a graph, taken from Brey et al. (2008), displaying Ca/(Ca+Mg+Fe^{2+}+Mn) values in garnet vs. the pressure, as well as isotherms. The average Ca/(Ca+Mg+Fe^{2+}+Mn) value, calculated from the results mentioned above, for KB6 is 0.129295 and for KB9 is 0.125858. By plotting the Ca/(Ca+Mg+Fe^{2+}+Mn) values of KB6 and KB9 on the correct isotherms, pressures could be read off as 4.12 GPa (41.2 kbar) for KB6 and 6.03 GPa (60.3 kbar) for KB9.

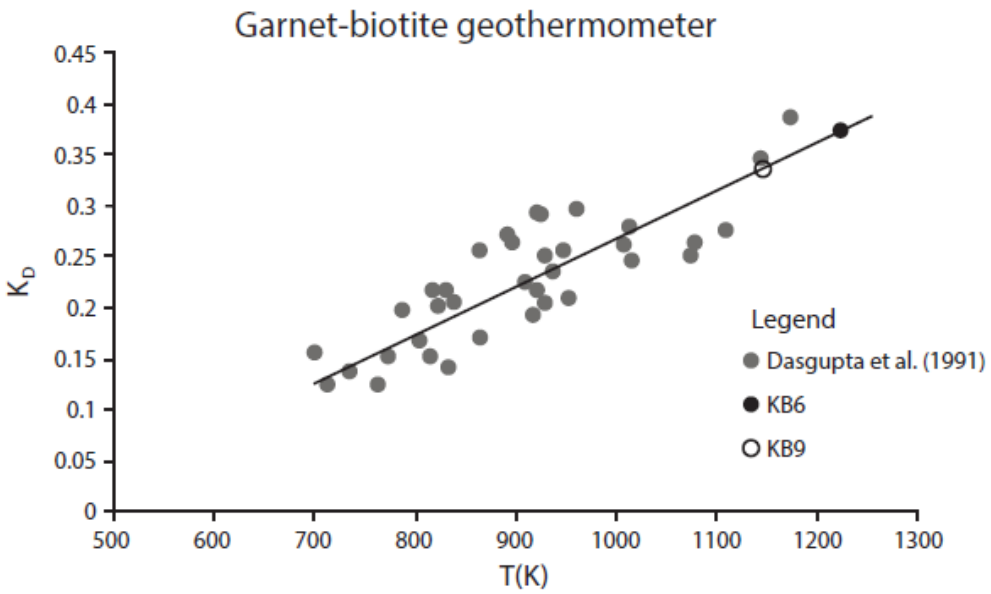

Figure 3.24: Graph displaying the K_D value (distribution coefficient) vs. the temperature. The grey points are values taken from Dasgupta et al. (1991), the solid black point is the K_D value of KB6 and the open point is the K_D value of KB9.

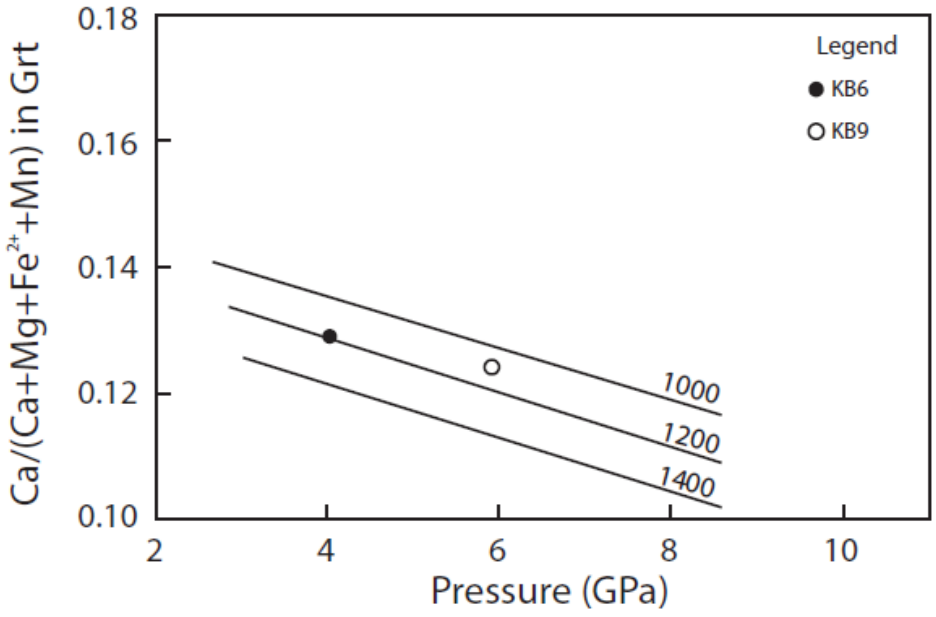

Figure 3.25: Graph, modified after Brey et al. (2008), of the composition of the garnet used in the geothermometry calculations vs. the pressure with isotherms. The solid black point represents sample KB6 and the open black point represents sample KB9.

3.5.2 Garnet-orthopyroxene geothermometry

Figure 3.26 displays coexisting garnet and orthopyroxene grains with SEM-WDS measurements taken at points A (result KB6Opx5 in appendix 1) and B (result KB6Gt3 in appendix 1) from sample KB6. From these two points it was determined that the K_D value ($K_D = \left\{\frac{Fe}{Mg}\right\}^{ga} / \left\{\frac{Fe}{Mg}\right\}^{opx}$) is 2.521368.

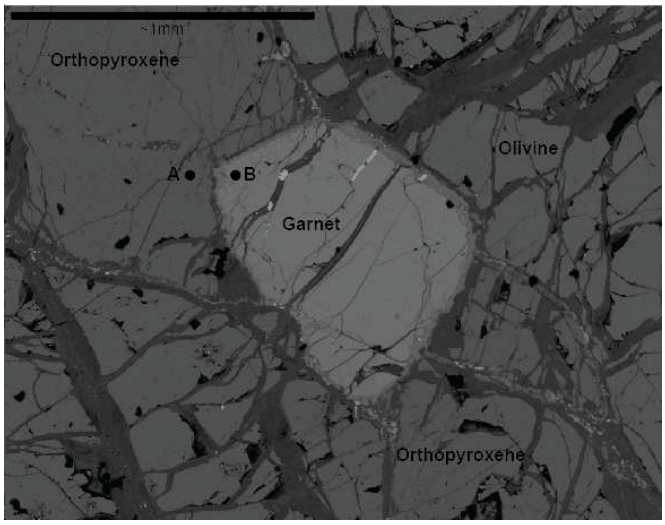

Figure 3.26: Backscatter electron image from KB6 which displays consecutive orthopyroxene and garnet grains where analysis A and B is then used to determine the K_D value and then the temperature of formation in figure 3.27.

Figure 3.27 is a plot of K_D vs. T (K), with the grey points as reference points that were taken from Harley (1984) to create a trend line. The K_D value for KB6 was then plotted on this trend line and a temperature of 990 K was read off the graph. The temperature obtained and the K_D value were then used to obtain the pressure of the sample using the graph in figure 3.28. The pressure obtained from this and the pressure of 5.58 kb (0.558 GPa). This temperature and pressure can represent the formation conditions or the last metamorphic event.

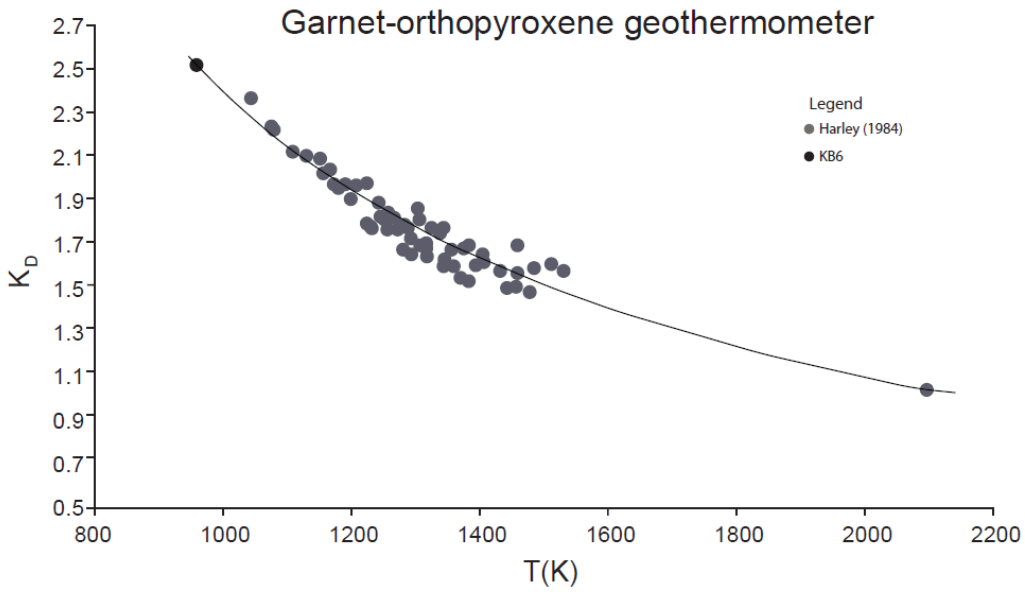

Figure 3.27: Graph displaying the K_D value (distribution coefficient) vs. the temperature where the grey points are values taken from Harley (1984) and the solid black point is the K_D value of sample KB6.

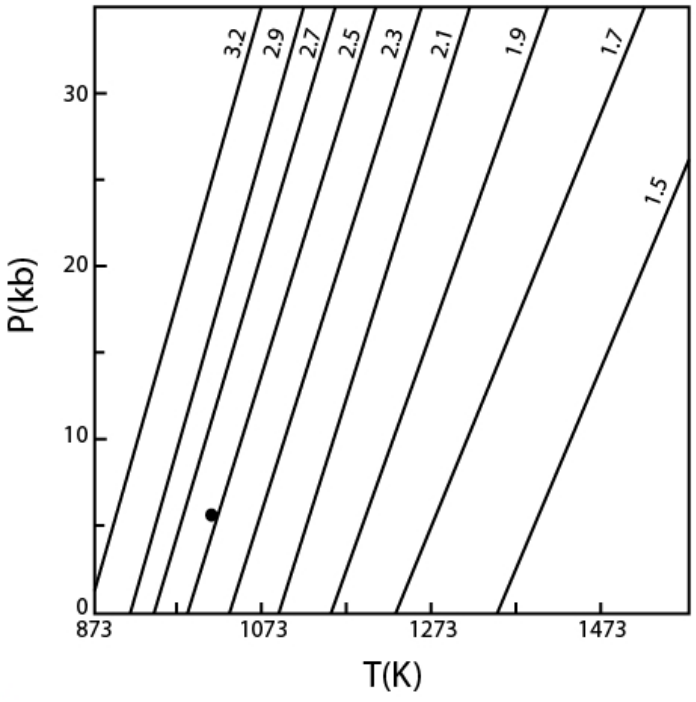

Figure 3.28: A graph taken from Harley (1984) with iso-K_D lines. The black point represents the K_D and temperature of sample KB6.

3.5.3 Two pyroxene geothermometry

Figure 3.29 displays coexisting clinopyroxene and orthopyroxene grains with SEM analysis done at points A (result KB10Cpx4 in appendix 1) and B (result KB10Opx2 in appendix 1) from sample KB10. From the analysis done at these two points, the K_D value ($K_D = (1 - Ca)^{cpx}/(1 - Ca)^{opx}$) was calculated to be 0.214658.

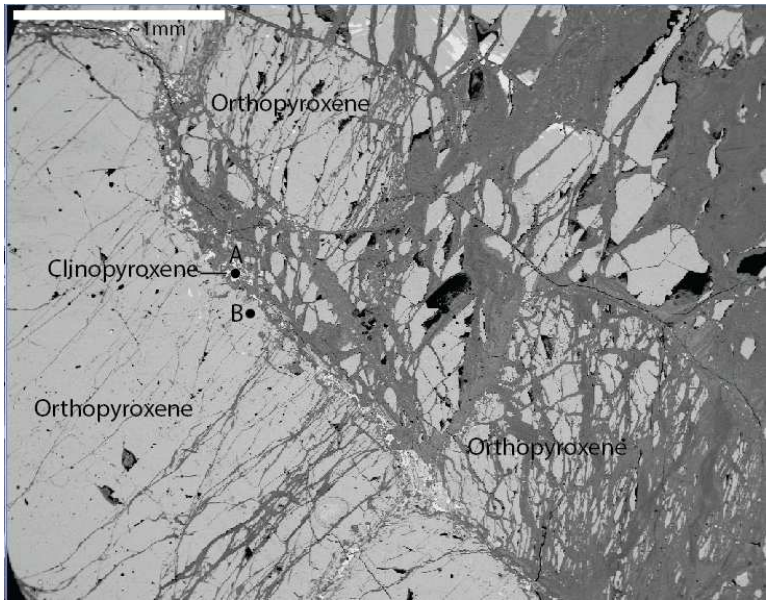

Figure 3.29: Backscatter electron image of coexisting orthopyroxene and clinopyroxene grains in KB10. Analysis was preformed at point A and B, which was then used to determine the K_D value and then the temperature of formation in figure 3.30.

Figure 3.30 is a plot of K_D vs. T(K), with pyroxene compositions from studies by Gasparik (1984) and Brey et al. (2008), used as references. On this diagram the K_D value for KB10 plots at a temperature of 1531 K for mineral formation or the last metamorphic event. This temperature, along with the $\ln K_D$ value, was then used to determine the pressure of the sample using the graph in figure 3.31. With a

temperature of 1258 ˚C and a $\ln K_D$ value of -1.538709, a pressure of 39.94 kb (3.99 GPa) was determined for the pyroxene formation in sample KB10.

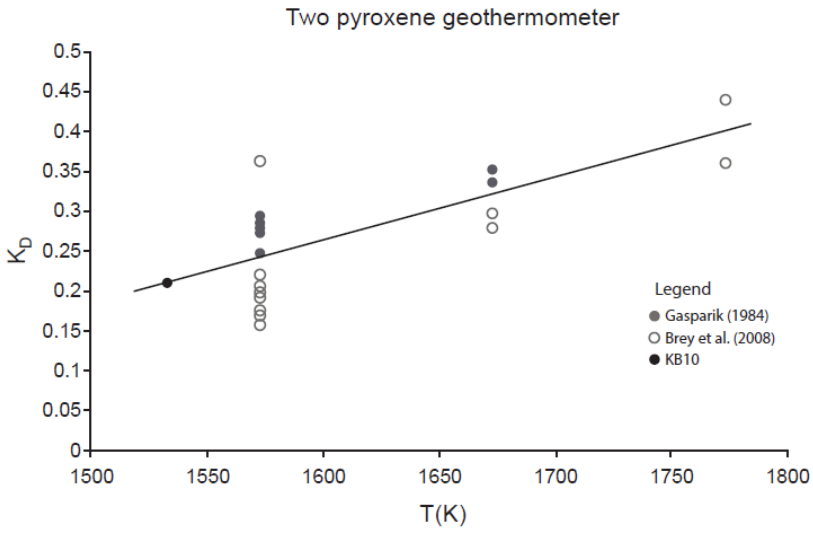

Figure 3.30: A display of the distribution coefficient vs. the temperature. The solid grey points are values taken from Gasparik (1984) and the open grey points are taken from Brey et al. (2008). The solid black point is the K_D value of sample KB10.

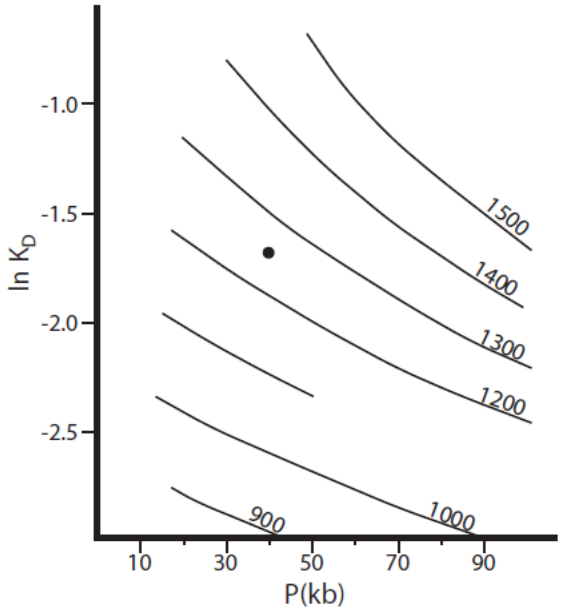

Figure 3.31: The solid lines represent isotherms in ˚C and the solid point represents the ln K_D and temperature values for sample KB10. (Graph taken from Nickel et al. (1985) with reference to the CMAS system)

3.6 Melt inclusion study

Melt inclusions were investigated to analyse the OH^- content in these inclusions. Using synchrotron based FT-IR, a specific melt inclusion was investigated in sample KB3. The motive for choosing this melt inclusion was the small amount of OH^- that is found within the inclusion in relation to the matrix of the garnet. This melt inclusion was then used to determine the temperature of formation. Figure 3.32 displays the studied melt inclusion,and its size. The images figure 3.32A and 3.32B are images of the layers above and below the melt inclusion respectively. These images display that the melt inclusion is fully embedded and thus no contamination occured. Maps of the OH^- concentration were created of the area and displayed in figure 3.33 in both 2D and 3D. The higher OH^- concentrations in these images is displayed in white/pink and the lower concentrations are blue. Figure 3.34 verifies that figure 3.33 displays OH^- composition due to the infrared band position that is found at 3655 cm^{-1}, as mentioned in the Introduction. The highest OH^- concentration is found in the matrix of the garnet and is lower in the melt inclusion which can be concluded from the concentration in figure 3.33.

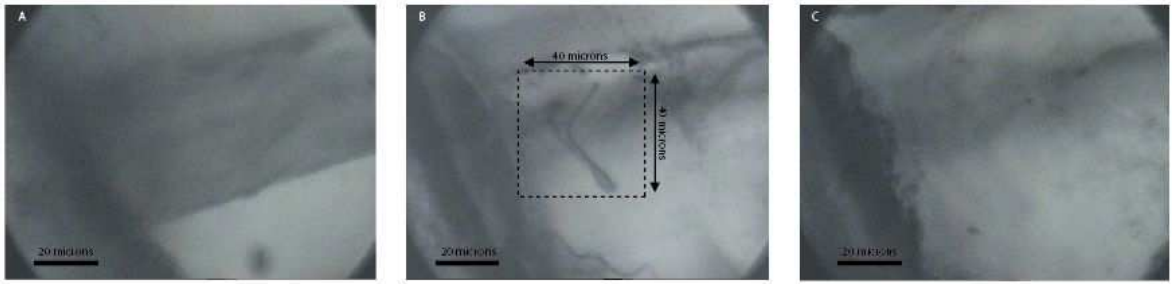

Figure 3.32: Backscatter electron images displaying: A – The area below the melt inclusion. B –The melt inclusion under investigation in sample KB3. C – The area below the melt inclusion. Images A and C are displayed here to demonstrate that there aren't defects above or below the melt inclusion, thus it is totally embedded.

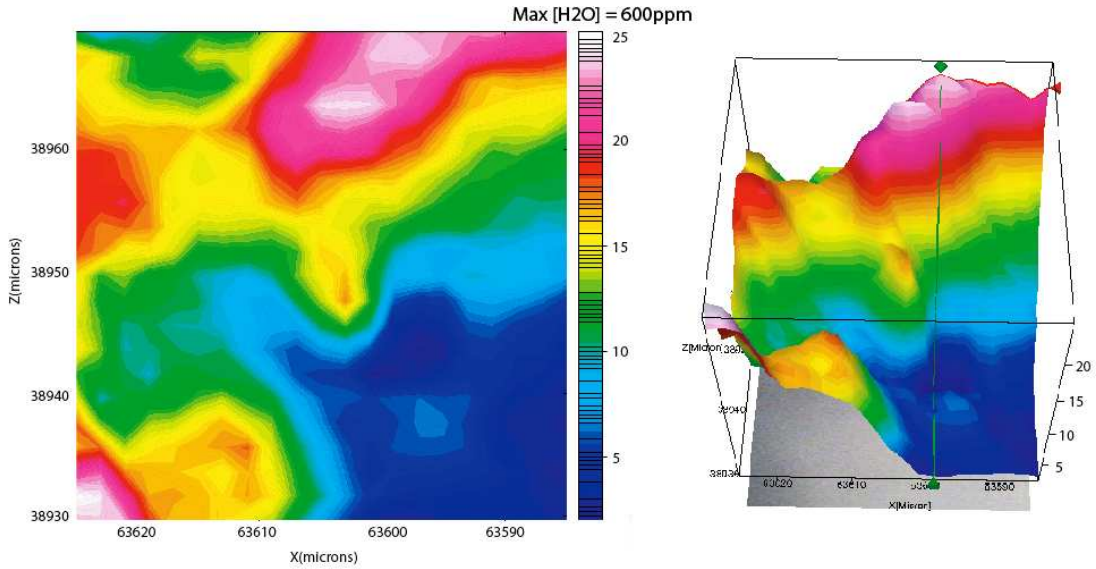

Figure 3.33: OH^- map of figure 3.32B in both two dimensions and three dimensions. Pink/white colours display areas of higher OH^- content and blue colours are areas of lower OH^- content.

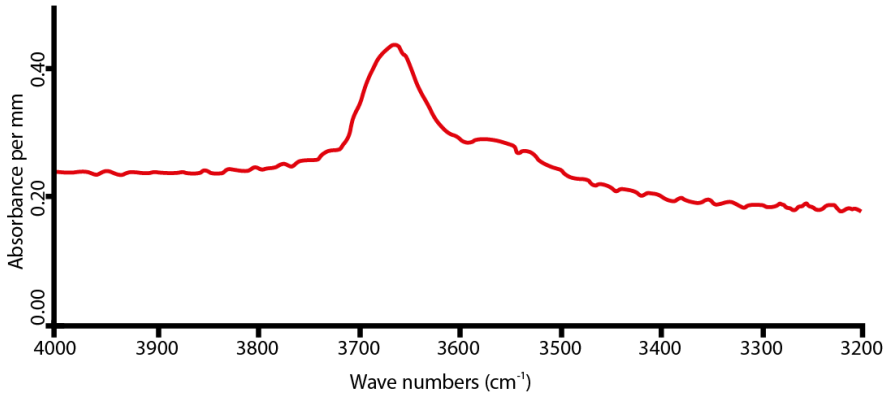

Figure 3.34: The OH^- infrared band position at 3655cm^{-1} on the melt inclusion.

The composition of the studied melt inclusion was determined using SEM-WDS and can be found in table 12. Yoshino et al. (2009) displays results of pressures, temperatures and compositions of melt within various peridotite samples. These results were then used to create a diagram displaying SiO_2 and MgO wt% against the temperature of the melt in experiments (Figure 3.35). Within this figure, the blue

points represent the SiO_2 compositions and the pink points represent the MgO compositions, taken from Yoshino et al. (2009), also displaying trend lines of each element. The green points are the compositions of the melt inclusion (figure 3.32) composition determined from sample KB3. Using the green points it can be deduced that the temperature of formation is 1620 ºC (1892 K).

Table 12: Composition of the melt inclusion obtained using SEM-WDS (refer to table 4 for standards).

SiO_2	Al_2O_3	Cr_2O_3	FeO	MnO	MgO	CaO	NaO	K_2O
46.59	2.50	10.07	7.96	0.01	29.29	0.53	0.23	0.12

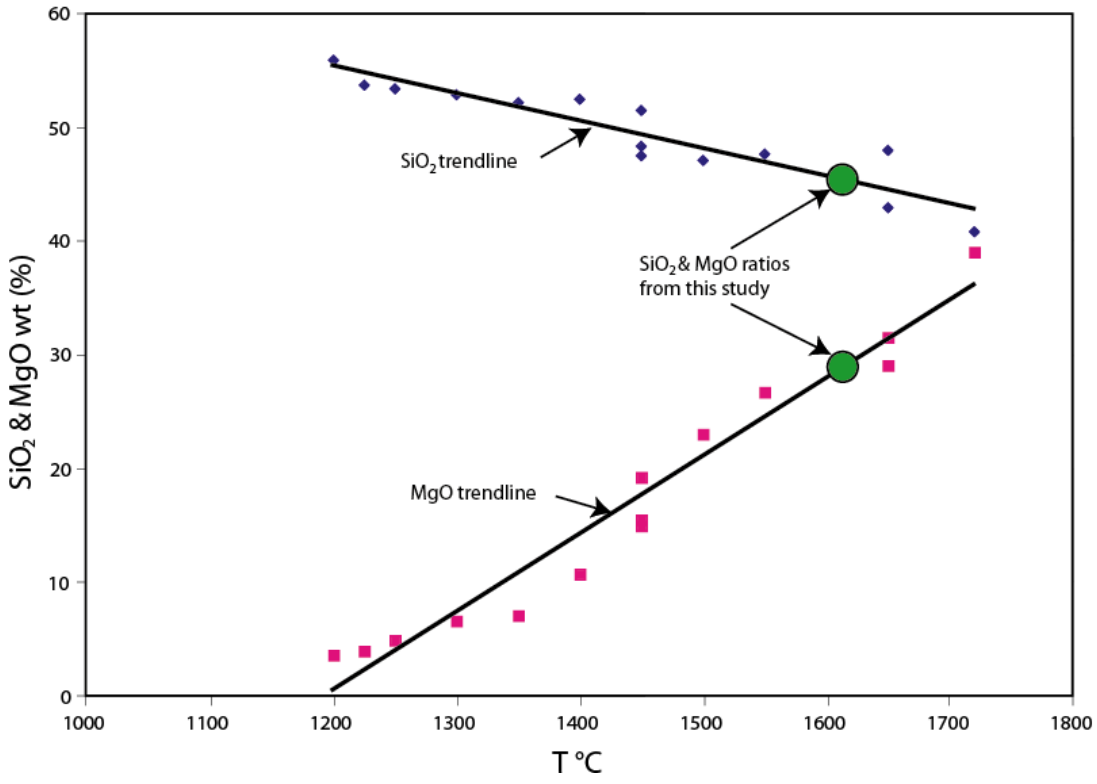

Figure 3.35: MgO (pink points) and SiO_2 (blue points) trend lines deduced from the results from experiments on melt according to their temperatures and compositions (Yoshino et al., 2009). The melt composition of the studied sample is also displayed as the green points.

3.7 Depth calculations

There is an increase in temperature and pressure with an increase in depth below the earth's surface. The geothermal gradient varies according to location and depth and the pressure gradient is dependent on the density of the overlying rocks. According to Dziewonski and Anderson (1981) there is a linear pressure gradient in the crust, mantle and inner core, due to the fact that these sections are composed mostly of solids, but the outer core is a liquid forming a non-linear gradient. An approximate rate of pressure increase (pressure gradient) with an increase in depth is: 0.03 GPa/km (crust) and 0.035 GPa/km (mantle), taken from Dziewonski and Anderson (1981). The thickness of the crust in the Kimberley area of 35.4 km was taken from Niu and James (2002). Using the pressures determined using geothermobarometry and from the composition of the melt inclusion which (table 13), the depths were determined. The depth of the samples was calculated using the following equations and displayed in figure 3.36:

If the sample originated from within the mantle:

$$Depth = Thickness\ of\ the\ crust + (\frac{Pressure - x}{Mantle's\ pressure\ gradient})$$

where:

$$x = Thickness\ of\ the\ crust\ \times Crust's\ pressure\ gradient$$

If the sample originated from within the crust:

$$Depth = (\frac{Pressure}{Crust's\ pressure\ gradient})$$

Table 13: Summary of the temperatures and pressures calculated in this study.

Sample	Temperature	Pressure	Method	Depth
KB3	1893 K	5.60 GPa	Experimental melt inclusion compositions	165.06 km
KB6a	1205 K	4.12 GPa	Garnet-biotite geothermometry	122.77 km
KB6b	990 K	0.56 GPa	Garnet-orthopyroxene geothermometry	18.67 km
KB9	1145 K	6.03 GPa	Garnet-biotite geothermometry	177.34 km
KB10	1531 K	3.99 GPa	Two pyroxene geothermometry	119.06 km

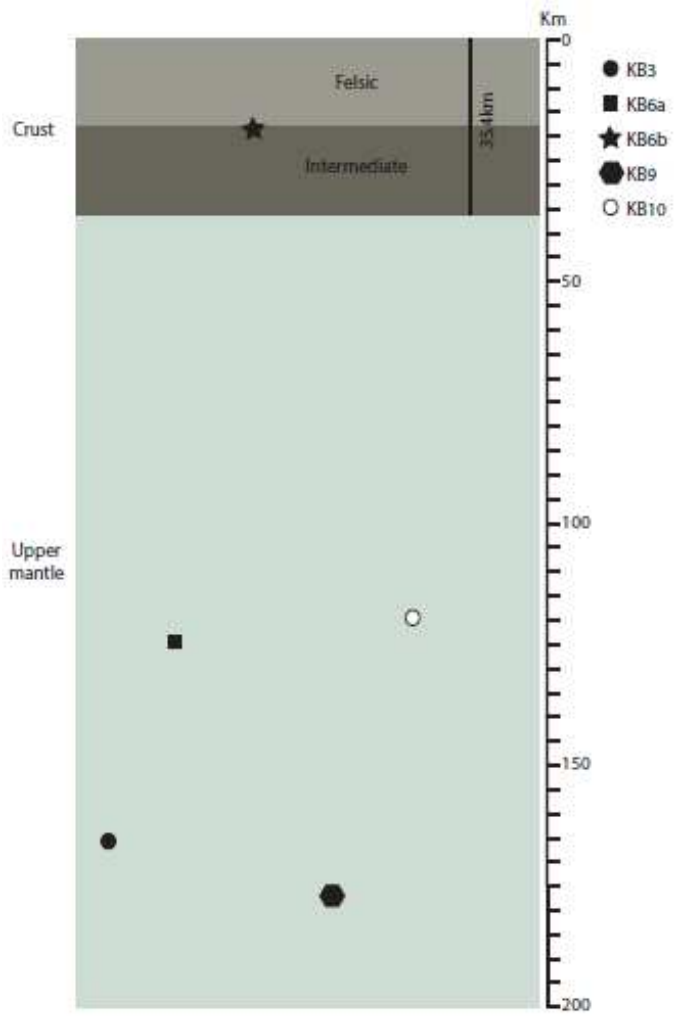

Figure 3.36: Display of the depths of the samples in table 13. The pressure gradient was calculated according to Winter (2001) and the thickness of the crust in the Kimberley area was taken from Niu and James (2002).

3.8 Micro crack study

A line defect structure in a garnet crystal (Figure 3.37) was investigated, which is sub-micron in width and is known as a monominerallic grain boundary. This defect is totally embedded in the crystal and thus there could be no contamination of OH^- from external sources. Synchrotron-based FT-IR was used to investigate this section, results are displayed in figure 3.38. Figure 3.38 consists of a 2D and a 3D image of the OH^- concentrations over the defect structure. The blue colours represent lower OH^- concentrations and the pink/white colours represent high OH^- concentrations. The OH^- concentration peaks in the line defect and diffuses out into the matrix of the garnet. The maximum concentration of OH^-, measured in within the crack, is approximately 450 ppm. Figure 3.39 displays the FT-IR peak in the centre of the line defect structure with an infrared band position at 3690 cm^{-1}, concluding that OH^- was measured in this scenario.

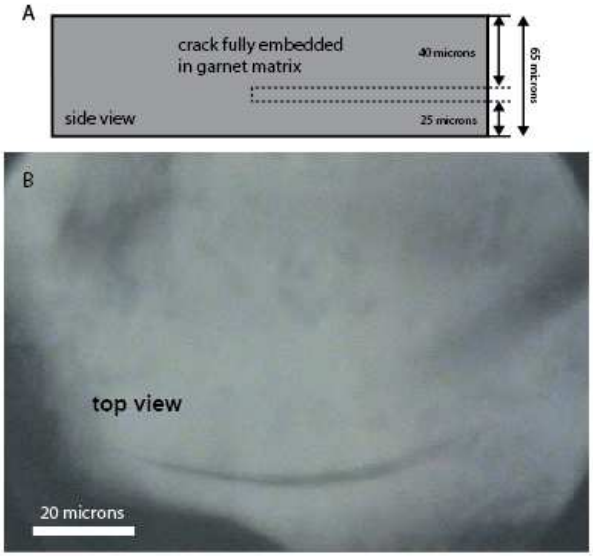

Figure 3.37: A – Demonstrates the concept of a totally embedded sub-micron crack. B - Backscatter electron image of the line defect that was investigated.

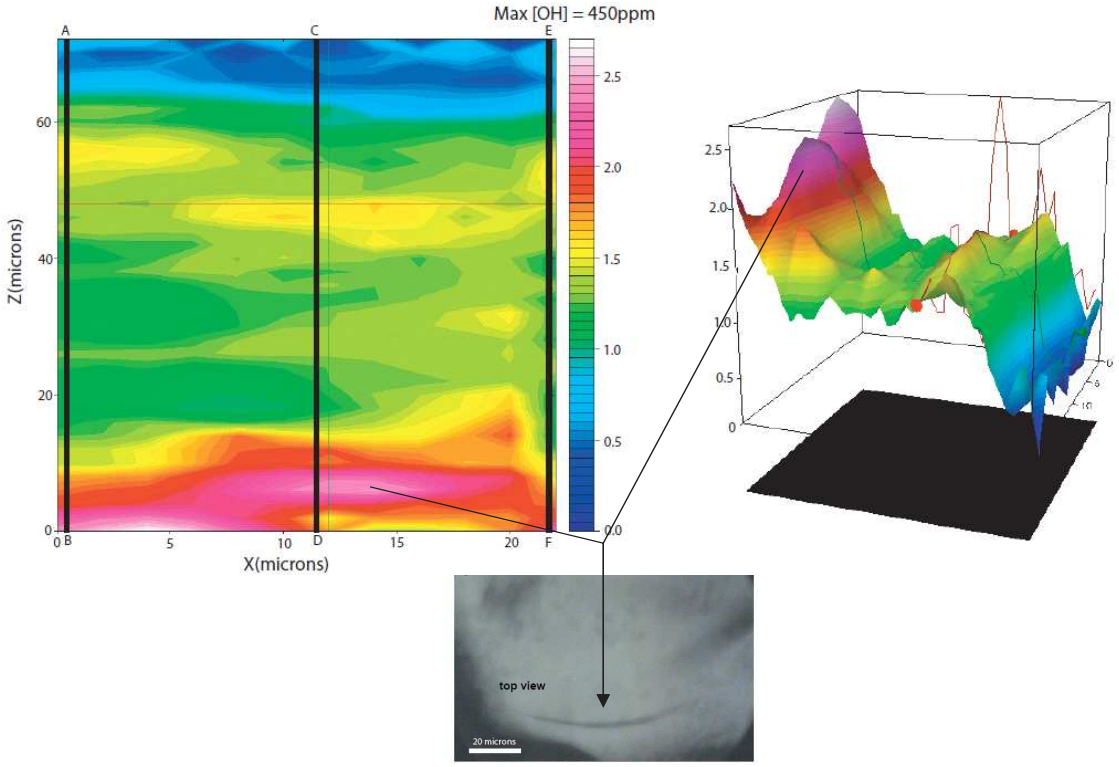

Figure 3.38: OH^- distribution over the area shown in figure 3.37B measured with a synchrotron-based FT-IR. White/pink colours represent higher OH^- content and blue colours represent lower OH^- content. It can clearly be viewed that the highest concentration is found within the defect structure and diffuses out into the matrix of the garnet. Where the blue and red lines coincide, is the point where the peak in figure 3.39 was taken. The lines 'AB', 'CD' and 'EF' are used in figures 3.41, 3.43 and 3.45.

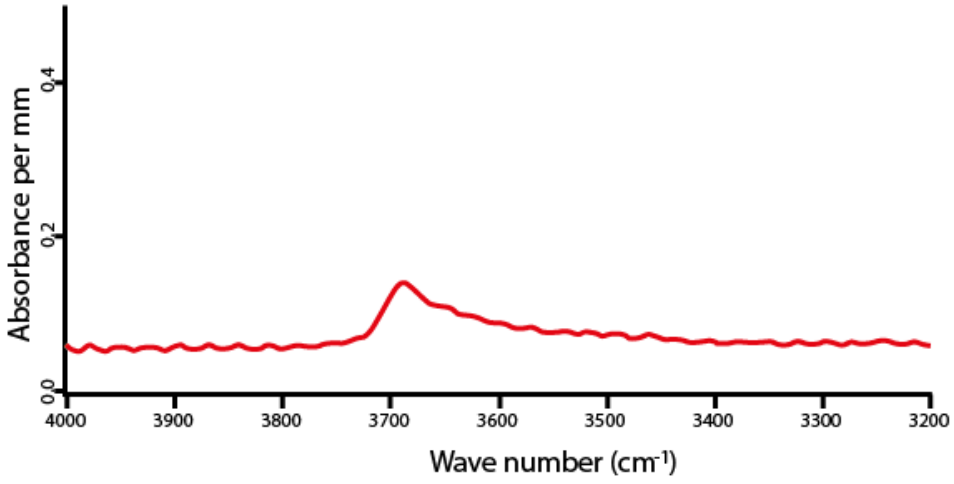

Figure 3.39: OH^- absorbance peak at 3690cm^{-1} taken on the line defect.

The equation below expresses the distribution coefficient of H^+ between melt and peridotites, as well as the effect that hydrogen has on nominally anhydrous minerals, with relation to the solidus (dry) (Aubaud et al., 2004). A change in the enthalpy results in a change in entrophy and thus alters the temperature and pressure conditions. This equation is the basis of the lines in figure 3.40.

$$T = \frac{1}{\left(\frac{1}{T_{peridotite}^{fusion}}\right) - \left(\frac{R}{\Delta H_{peridotite}^{fusion}}\right)\ln\left(1 - X_{OH^-}^{melt}\right)}$$

T: melting temperature (wet melting)

$X_{OH^-}^{melt}$: fraction of OH^- into the melt in moles

$T_{peridotite}^{fusion}$: dry peridotite's melting temperature

$\Delta H_{peridotite}^{fusion}$: change in enthalpy of the fusion of the peridotite

R: gas constant

Figure 3.40 displays the dry solidus of basaltic melt with respect to temperature and pressure, (Aubaud et al., 2004). As OH^- is added to the melt in parts per million, so the solidus moves to lower temperatures and pressures. The other lines found in this figure are adiabats which are lines found on thermodynamic charts of a specific substance that undergo adiabatic change. An adiabatic change is a change in temperature, volume or pressure where there is no energy transfer between the systems. The plume adiabat indicates mantle origin and the ridge adiabat indicates mid-oceanic ridge origin. The temperature of the melt studied was taken from figure 3.35 and projected into figure 3.40, and the pressure was taken from Purchase

(2009), thus representing the vertical and horizontal lines, which indicates a mantle origin as well as an OH^- content of 200 ppm of the entire peridotite.

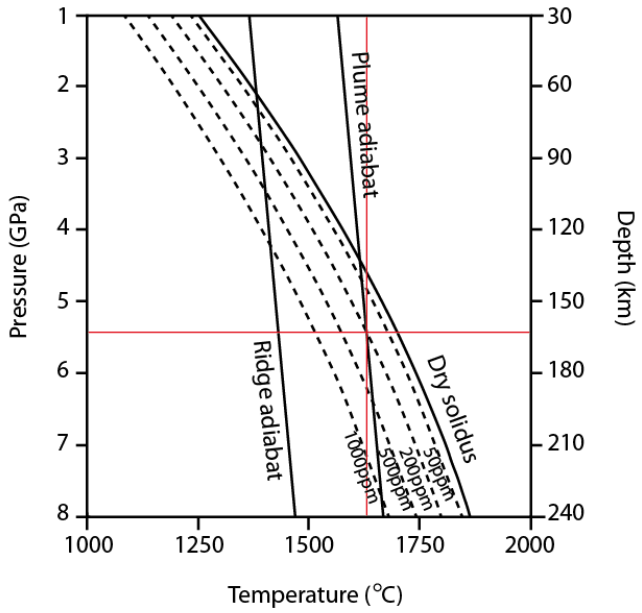

Figure 3.40: The effect of H within NAMs on the peridotite solidus according to Aubaud et al. (2004). The red lines represent the temperature and pressure of sample KB3, indicating an OH^- content of 200ppm for the entire sample.

The OH^- was calculated along sections perpendicular to the planar defect in order to observe the diffusion profile. It was calculated using the formula taken from Bell and Rossman (1992a): concentration of OH^-(ppm) = 0.7194 x Integrated absorbance per cm sample thickness. Figure 3.41 displays the diffusion profile along line 'AB' on the two dimensional image in figure 3.38, figure 3.43 displays the diffusion profile along line 'CD' and figure 3.45 displays the diffusion profile along line 'EF'. Each of the profiles contains a best fit curve and was split into parabolas (Figure 3.42, 3.44 and 3.46) used to calculate the ascent rate of the kimberlite.

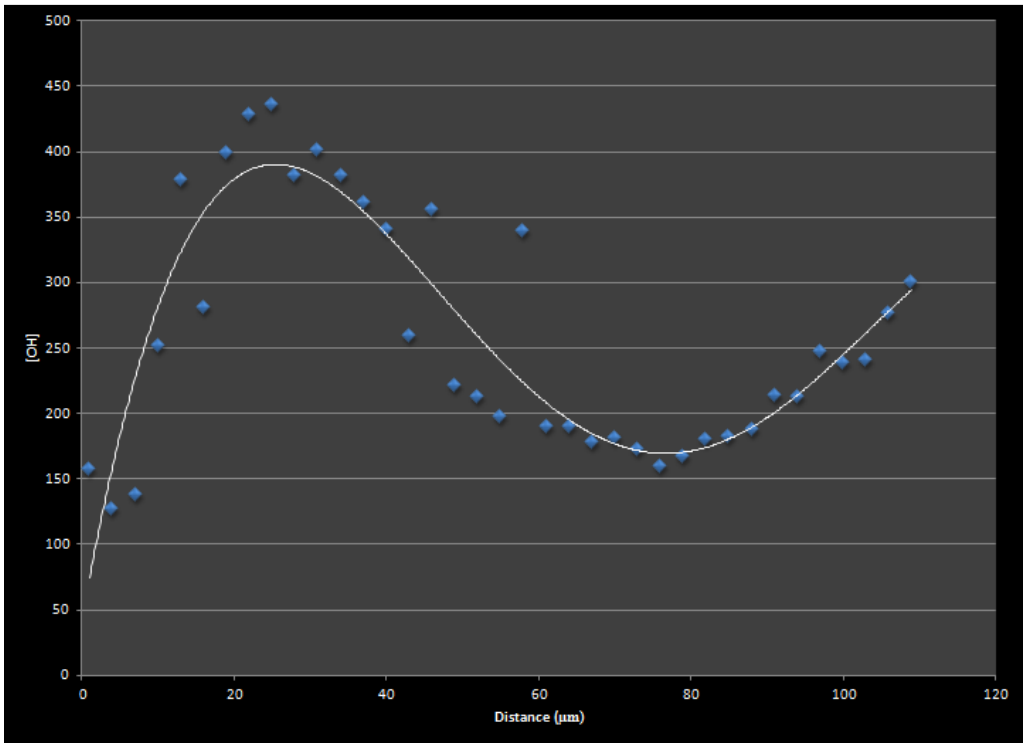

Figure 3.41: OH^- diffusion profile along the line 'AB' in figure 3.38. The OH^- concentrations and distance can be observed in the graph.

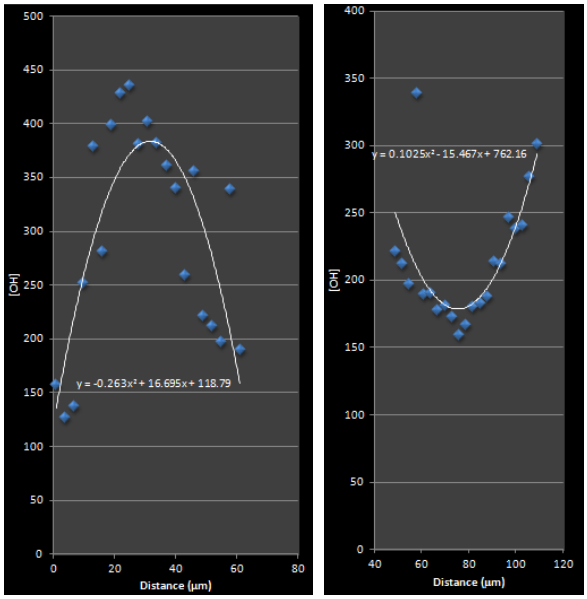

Figure 3.42: The diffusion profile in figure 3.41 is split into the parabolas.

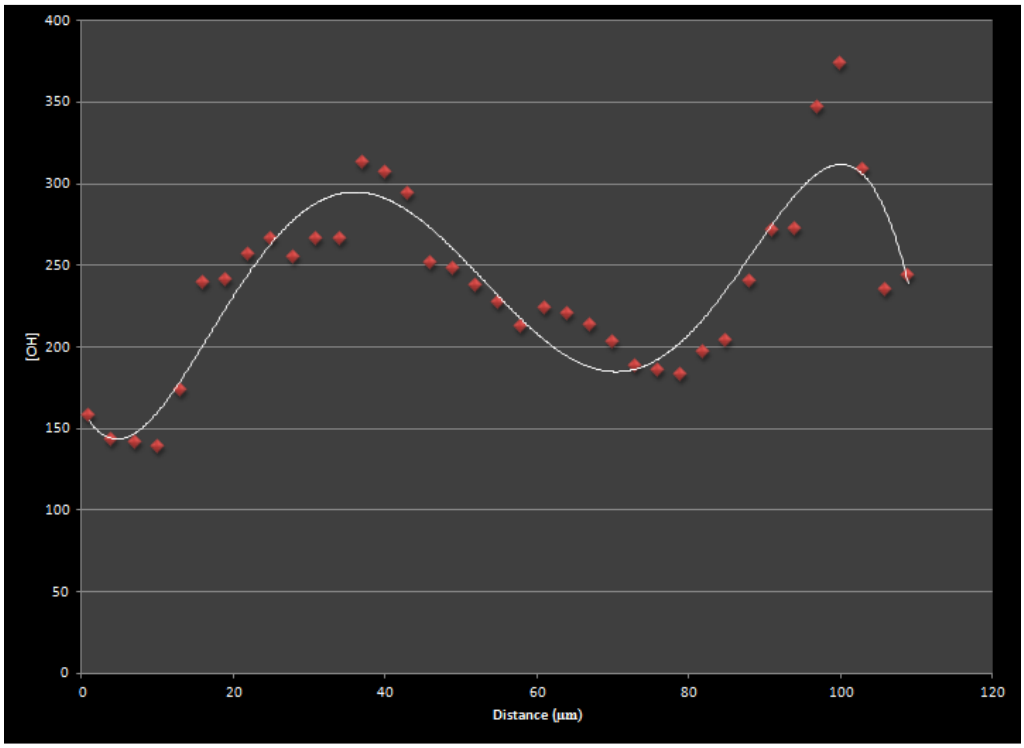

Figure 3.43: Diffusion profile along OH^- diffusion profile along line 'CD' in figure 3.38. The OH^- concentrations and distance can be observed in the graph.

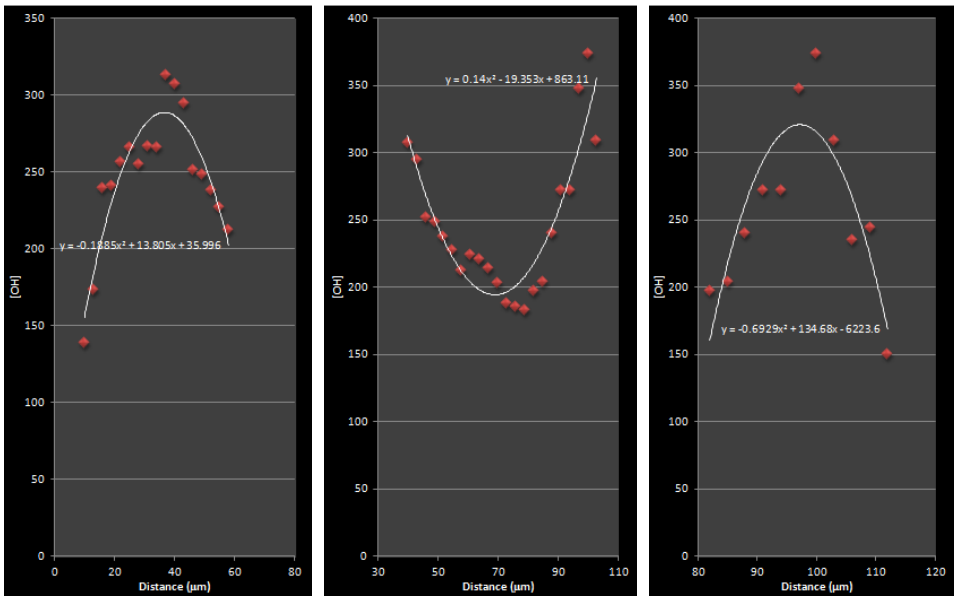

Figure 3.44: Display of the separated parabolas of figure 3.43.

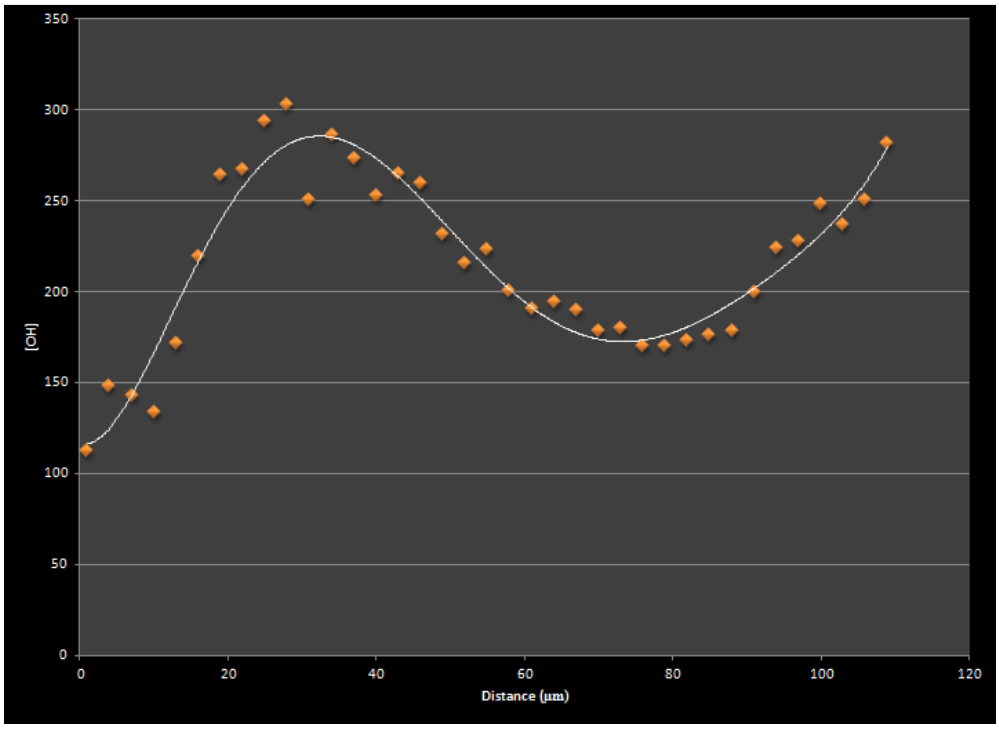

Figure 3.45: Diffusion profile along line 'EF' in figure 3.38, displaying the OH^- concentration over the distance of analysis.

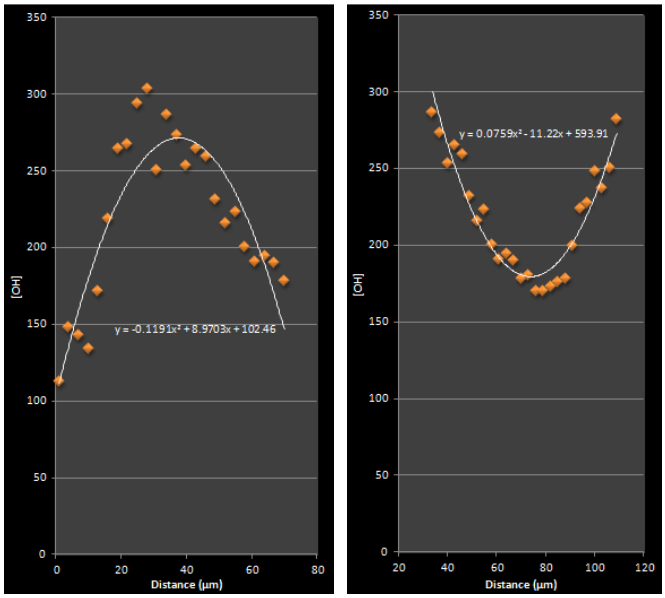

Figure 3.46: The separation of the diffusion profile in figure 3.45.

The following equation, taken from Ingrin and Blanchard (2006), is used to determine the diffusion coefficients of H^+ within the mineral structure of garnets which is needed to calculate the ascent rate:

$$D_{garnet} = D_0 exp(\frac{-130 \pm 15 kJ.mol^{-1}}{RT}) \quad (1)$$

D_{garnet}: garnet's diffusion coefficient

D_0: $\log D_0 = -6.28 \pm 0.72$

R: gas constant of 8.314 $J.K^{-1}mol^{-1}$

T: temperature

According to Demouchy et al., (2006), plots (concentration of H_2O versus the distance along the sample, such as figure 3.41 – 3.46) are used to determine the hydrogen diffusivity within minerals. Fick's second law (diffusion) was used to determine the ascent rate:

$$C_{OH}(x) = C_0(erfc\left(\frac{x}{2\sqrt{D_i t}}\right) + erfc\left(\frac{X-x}{2\sqrt{D_i t}}\right)) \quad (2)$$

$C_{OH}\ (x)$: hydroxyl concentration specifically at distance x from the sample edge

X: sample width

t: time

$erfc$: complementary error function

C_0: maximum water concentration

D_i: mobile component's chemical diffusivity

Equation (1) obtained a diffusion rate of 2.99186×10^{-11} of hydrogen in a garnet at a temperature of 1620 ºC (Figure 3.35). The diffusion coefficient was taken from Ingrin and Blanchard (2006) and is specifically generated for each mineral. This value was then used in the equation (2) along with the following data: OH^- concentration at certain distances (Figure 3.42, 3.44 and 3.46), maximum concentration of OH^- as 450ppm and width of the thin section as 0.000111 m. The temperature is directly proportional to the ascent rate owing to the viscosity of the kimberlitic melt. The time taken for the ascent process ranges between approximately 30min and a couple of hours.

4 Discussion

The samples investigated during this research, where all peridotites from the Bultfontein mine in South Africa. The following analytical methods were used: petrographic microscope, SEM and FT-IR spectroscopy and the following conclusions can be made to the following areas of interest which are mentioned in the introduction are:

"Metasomatism and effects of a kimberlitic melt on peridotitic xenoliths"

According to Nielson Pike and Schwarzma (1977), the rocks in this study are metamorphic, equigranular-mosaic. The grains in this classification are equigranular and are polygonal and have boundaries that are fairly straight (Figure 3.3 K and L). Triple junctions (120º) (Figure 3.3 A and B) are also found. Spinels, which are found in this classification and in coarser grained samples, are found as inclusions within silicate minerals (Figure 3.3 M and N) (Nielson Pike and Schwarzma, 1977).

The samples are homogenous. The orthopyroxenes in all the samples are enstatites, the clinopyroxenes are either diopsides or endiopsides, the garnets are rich in pyrope component and the olivines are forsterites ($Fo_{>90}$). All these minerals are high in Mg^{2+} content and showing high temperature conditions (>1300 ºC, according to Bowens reaction) during formation. The homogenity of the garnets shows that the uplift of the samples was too fast to allowing changes in temperatures and pressures to be reflected on the minerals themselves, although the slight peaks that are found within the elemental graphs of the garnets are possibly due to inclusions within the garnets. Tschermakite is an amphibole that occurs in rocks such as eclogites and ultramafic rocks, and usually conditions of medium to high grade metamorphism (Winchell, 1945). Antigorite commonly replaces ultramafic minerals, pervasively or in

crosscutting veinlets (Wenk and Bulak, 2004). .When comparing the mineral analysis with other results such as: Gregoire et al. (2003) and Varne (1970), the results are similar. Metasomatism and decompression are viewed in figures 3.5 and 3.6. Metasomatism causes the hydraulic fracturing and the source of the hydrant is the kimberlitic melt, where as the decompression textures form during the ascent.

Garnets are unstable when interacting with melt at <40km depth below the surface and temperatures greater than 850ºC (Rutherford, 2008). Dissolution of the garnets to spinel, which was viewed in sample KB1, occur at this temperature and when exposed to temperatures as high as 1200ºC, the dissolution takes place in less than an hour in the presence of H_2O-rich kimberlitic melt (Rutherford, 2008). This then implies that the garnets and the samples interacted with the kimberlitic melt.

"Peridotitic depth of origin"

During the investigation of OH^- within a garnet that contains a melt inclusion, it was found that the OH^- resides mostly in the garnet matrix and in very low quantities in the melt inclusion itself. The temperature and pressure of the melt inclusion allocate the origin of the sample as they plot on the plume adiabat and thus imply mantle derivation. The distribution coefficient of water between the garnet and the melt can be calculated using: $D = H_2O_{garnet}/H_2O_{melt}$. In this case it results in 0.1.

The geothermobarometry results display that the samples are from great depths with high temperatures and pressures, which is also displayed by the mineral assemblages. The temperatures obtained range between 990 K and 1893 K and the pressures between 0.56 GPa and 6.03 GPa. Using the pressures, the depths obtained range between 18.67 km and 177.34 km into the surface. Sample KB6b was calculated to have originated from within the continental crust, yet KB6a

originated from well into the mantle, even though this is the same sample. This discrepancy is due to the different geothermometric methods used and the effects that the analytical methods have on the results (Mofokeng, 1998). The garnet-orthopyroxene geothermometer (KB6b), according to Harley (1984), is affected by the MnO and the Fe_2O_3 constituent in the garnet. Dasgupta et al. (1991) reports that: the garnet-biotite Fe-Mg exchange thermometer (KB6a) that was developed by these authors, produces consistent results when comparing temperature results of rocks recrystallized at same metamorphic grade. In the Kimberley at a depth of 18.67 km into the crust, the rock composition is felsic to intermediate and peridotites are ultramafic.

"Kimberlitic melt's ascent rate"

The emplacement model that best suites this study is the Weertman crack model as this model involves a pressure that is high enough to result in speeds of ascent rates that match the results in this study. The planar defect structure found in the sample KB3 was analysed for OH^- content. The OH^- infrared band position over the defect structure is 3690 cm^{-1} and diffuses out into the matrix of the garnets creating diffusion profiles. These diffusion profiles can be used to determine the ascent rate of the kimberlitic melt to the surface. The OH^- found within the garnet grain is derived from the kimberlitic melt, which has a low viscosity of approximately: 0.1-1 Pa/s (Buisman and Spark, 2008). The highest density contrast occurs when the xenolith is incorporated within the kimberlitic melt, due to the fact that the kimberlite melt is a liquid and the deep mantle has a higher pressure. This then results in the xenolith increasing in volume as there is a change in the pressure conditions, forming decompression cracks. During crack formation the OH^- fills the void of the crack and will diffuse out of the crack into the surrounding matrix during uplift. Diffusion occurs

at high temperatures (temperature is directly proportional to the ascent rate) otherwise the melt would travel slower to the surface and thus increasing the resorption of diamonds. This diffusion process ends when the xenolith reaches the surface. The time measured here is then the time of the diffusion process which occurs from a depth of 150-180 km till the xenoliths reaches the surface. The ascent rate is dependent on the diffusion coefficient, which was taken from Ingrin and Blanchard (2006). The ascent rate determined is: 20–100 m/s. Other ascent rates include 5-37 km/s (Peslier et al., 2008). Demouchy et al. (2006) estimates that xenoliths take several hours to reach the surface from a depth of 60-70 km when travelling within a magma. Other results include an ascent velocity of 37-64 m/s involving the explosive eruptions (Humphreys et al., 2008). The reason for the differences in results is the lower viscosity of a kimberlitic melt compared to that of a magma. Melt has a high concentration of volatiles and thus lowering its viscosity and thus preserves diamonds, although similar to the results taken from Humphrey et al. (2008).

5 Conclusions

This thesis involves the investigation of ten samples taken from the Bultfontein kimberlite mine in Kimberley using a petrographic microscope, a WDS-SEM and a synchrotron-based FT-IR. During the microscopic study, hydration was observed (serpentinization) and that the rocks classify under metamorphic, equigranular mosaic. Garnets in the process of disseminating into spinels was also observed, which implies the sample was exposed to temperatures greater than 850 ℃. WDS-SEM was used to determine the compositions of the minerals in each of the samples as well as the composition of a melt inclusion. This melt inclusion was chosen on the criteria of needing to be totally-embedded, this is important to prevent contamination above or below the inclusion. Hydraulic fracturing was also found, implying hydration. The mineral's compositions were compared to other analysis executed on peridotites, all showing similar results. WDS-SEM analysis was preformed over garnet grains and results show that there is no zoning in them except possible grains of spinel causing random spikes in the compositions. Compositions of grain pairs of garnets-biotite, garnet-orthopyroxene and clinopyroxene-orthopyroxene (two pyroxene) was used in geothermobarometric studies. Temperature results range between 990 K and 1893 K and pressure results range between 0.56 GPa and 6.03 GPa. The pressures were then used to determine the samples depth of origin into the surface, the samples originated from depths ranging between 18.67 km and 177.34 km. Two geothermometers were preformed on sample KB6, this resulted in two very different depths, namely 122.77 km (garnet-biotite geothermometer) and 18.67 km (garnet-orthopyroxene geothermometer). This discrepancy can be attributed to analytical methods have different effects on the different geothermometers and the garnet-orthopyroxene geothermometer has a higher error

factor due to the fact that compounds such as MnO and Fe_2O_3 are not included in the determination of the K_D value. The main aim of this project was to locate defect structures in garnets using the synchrotron-based FT-IR and to then explore their OH^- content. The micro crack that was chosen to investigate was carefully picked to ensure no contamination. A diffusion profile of OH^- was found, which peaks within the crack and radiates outwards into the garnets matrix. This profile was used to determine the ascent rate as the diffusion process occurs during decompression as the sample is lifted towards the surface within the kimberlitic melt. Diffusion distance, diffusion coefficient of garnets, temperatures and OH^- concentrations were used to calculate the ascents rate. In conclusion it will take the kimberlitic melt between 30 min and a couple of hours to travel from a depth of 150-180 km at a speed of 20-100 m/s to reach the surface. The implication of this on kimberlites is the ascent rate is fast enough to preserve the diamonds and prevent resorption.

References

- Aubaud C, Hauri EH and Hirschmann MM, 2004, Hydrogen partition coefficients between nominally anhydrous minerals and basaltic melts, Geophysical Research Letters, v. 31, L20611, p. 1-4
- Bell DR and Rossman GR, 1991, The distribution of hydroxyl in garnets from the subcontinental mantle of southern Africa, Springer-Verlag, Contributions of Mineralogy and Petrology, v. 111, p. 161-178
- Bell DR, and Rossman GR, 1992a, The distribution of hydroxyl in garnets from the subcontinental mantle of southern Africa, Contributions to Mineralogy and Petrology, v. 111, p. 161-178
- Bell DR, and Rossman GR, 1992b, Water in Earth's mantle: The role of nominally anhydrous minerals, Science, v. 255, p. 1391-1397
- Bell DR, Rossman GR and Moore RO, 2004, Abundance and Partitioning of OH in a High-pressure Magmatic System: Megacrysts from the Monastery Kimberlite, South Africa, Journal of Petrology, v. 45, number 8, p. 1539-1564
- Beran A, Libowitzky E, 2006, Water in Natural Mantle Minerals II: Olivine, Garnet and Accessory Minerals, Reviews in Mineralogy and Geochemistry, v. 62, p. 169-191
- Best MG, 2003, Igneous and metamorphic petrology, Blackwell Science Ltd., Oxford, UK, 753pp
- Boyd FR and Danchin RV, 1980, Lherzolites, Eclogite and Megacrysts from some Kimberlites of Angola, American Journal of Science, v. 280A, p. 528-549

- Brey GP, Bulatov VK and Girnis AV, 2008, Geobarometry for Peridotites: Experiment in Simple and Natural Systems from to10GPa, Journal of Petrology, v.49, number 1, p. 3-24
- Brey GP and Kohler T, 1990, Geothermobarometry in Four-phase Lherzolites II: New Thermobarometers, and Practical Assessment of Existing Thermobarometers, Journal of Petrology, v. 31, number 6, pp. 1353-1378
- Buisman I and Sparks S, 2008, The Origin and Evolution of Kimberlite Melts: Stabilizing Phlogopite in the CMAS-CO2- H2O-K2O System, American Geophysical Union, abstract #V41D-2130
- Cairncross B, 2004, Field Guide to rocks and minerals in Southern Africa, Struik Publishers, South Africa, 292pp
- Clement CR, Skinner EM, Hawthorne JB, Kleinjan L and Allsopp HL, 1979, Precambrian ultramafic dykes with kimberlite affinities in the Kimberley area. Washington, DC: American Geophysical Union, Second International Kimberlite Conference, v. 1, p. 101-110
- Dasgupta S, Sengupta P, Guha D and Fukuoka M, 1991, A refined garnet- biotite Fe- Mg exchange geothermometers and its application in amphibolites and granulites, Springer, Contribution Mineral Petrol, v. 109, p. 130-137
- Demouchy S, Jacobsen SD, Gaillard F, Stern CR, 2006, Rapid magma ascent recorded by water diffusion profiles in mantle olivine, Geology, v. 34, number 6, p. 429-432
- Devine JD, Gardner JE, Brack HP, Layne GD, Rutherford MJ, 1995, Comparison of microanalytical methods for estimating H_2O contents of silicic volcanic glasses, American Mineralogist, v. 80, p. 319-328

- Dilek YD, Tulay B, Dikay A and Kazim Y, 2009, Fourier Transform Infrared (FT-IR) Spectroscopy for Biological Studies, G.U. Journal of Science, v. 22(3), p. 117-121
- Dowty E, 1978, Absorption optics of low symmetry crystals – application to titanian clinopyroxene spectra, Physics and chemistry of minerals, v. 3, p. 173-181
- Dziewonski AM, Anderson DL, 1981, Preliminary reference Earth model, Physics of the Earth and Planetary Interiors, v. 25, p.297–356
- Erlich EI and Hausel WD, 2002, Diamond Deposits: Origin, exploration and history of discovery, Society of Mining, Metallurgy, and Exploration, inc., Colorado, USA, 374pp
- Field M, Stiefenhofer J, Robey J, Kurszlaukis S, 2008, Kimberlite-hosted diamond deposits of southern Africa: A review: Elsevier, Ore Geology Reviews, v. 34, p. 33-75
- Gasparik T, 1984, Two-pyroxene thermobarometry with new experimental data in the system CaO - MgO - Al_20_3 - SiO_2, Springer, Contribution Mineral Petrol, v. 87, p. 87-97
- Gregoire M, Bell DR and Le Roex, AP, 2003, Garnet Lherzolites from the Kaapvaal Craton (South Africa): Trace Element Evidence for a Metasomatic History, Journal of Petrology, v. 44 (4), p. 629-657
- Gurney JJ, 1984, A correlation between garnets and diamonds, Kimberlite Occurrence and Origin: A basis for Conceptual Models in Exploration, Edited by L.E. Glover and P.G. Harris, University of Western Australia Publication, v. 8, p. 376-383
- Harley SL, 1984, An experimental study of the partitioning of Fe and Mg between garnet and orthopyroxene, Contribution Mineral Petrol, v. 86, p. 359-373
- Hirth G and Kohlstedt DL, 1996, Water in the oceanic upper mantle: implications for rheology, melt extraction and the evolution of the lithosphere, Earth and Planetary Science Letters, v. 144, p. 93-108

- http://www.googleearth.com - accessed 19 September 2011
- http://www.mindat.org/forum.php?read,86,213956,215013,quote=1 – accessed 17 October 2011
- Humphreys MCS, Menand T, Blundy JD and Klimm K, 2008, Magma ascent rates in explosive eruptions: Constraints from H2O diffusion in melt inclusions, Earth and Planetary Science Letters, v. 270, p. 25–40
- Ingrin J, Blanchard M, 2006, Diffusion of Hydrogen in Minerals, Reviews in Mineralogy and Geochemistry, v. 62, p. 291-320
- Lewis HC, 1897, Genesis and matrix of the diamond, Longmans Green and Co., London, 120pp
- Lloyd FE, Edgar AD, Forsyth DM and Barnett RL, 1991, The paragenesis of upper-mantle xenoliths from the Quaternary volcanics south-east of Gees, West Eifel, Germany, Mineralogical Magazine, v. 55, p. 95-112
- Liu X, Jin Z, Green HW, 2007, Clinoenstatite exsolution in diopsidic augite of Dabieshan: Garnet peridotite from depth of 300 km, American Mineralogist, v. 92, p. 546-552
- Meeker GP, Lowers HA, Swayze GA, Van Gosen BS, Sutley SJ and Brownfield IK, 2006, Mineralogy and morphology of amphiboles observed in soils and rocks in El Dorado Hills, California: U.S. Geological Survey, Open File Report 2006-1362, 47pp
- Miller, G.H., Rossman, G.R., and Harlow, G.E., 1987, The Natural Occurrence of Hydroxide in Olivine: Physics and Chemistry of Minerals, v. 14, p. 461-472
- Mitchell RH, 1986, Kimberlites: mineralogy, geochemistry and petrology, Plenum Press, New York, 442pp
- Mofokeng, S, 1998, A comparison of the nickel and the conventional geothermometers with respect to the Jagersfontein and the Matsoku kimberlite

peridotite xenoliths, Unpublished M.Sc. thesis, University of Cape Town, South Africa

- Nickel KG, Brey GP and Kogarko L, 1985, Orthopyroxene-clinopyroxene equilibrium the system CaO - MgO- Al_20_3 -SiO_2 (CMAS): new experimental results and implications for two-pyroxene thermometry, Contributions to Mineralogy and Petrology, v. 91, p. 44-53
- Nielson Pike JE and Schwarzma EC, 1977, Classification of Textures in Ultramafic Xenoliths, Journal of Geology, v. 85, no. 1, p. 49-61
- Niu F and James DE, 2002, Fine structure of the lowermost crust beneath the Kaapvaal craton and its implications for crustal formation and Evolution, Science Direct, Elsevier, Earth and Planetary Science Letters, v. 200, p. 121-130
- Norris RJ and Henley RW, 1976, Dewatering of a metamorphic pile, Geology, v. 8, p. 333-336
- O'Leary JA, 2007, Hydrogen isotope geochemistry of the mantle: constraints from back arc basin basalts and mantle xenoliths, PhD Thesis California institute of technology, Pasadena
- Park RG, 2005, Foundations of Structural Geology, 3rd edition, Routledge Taylor and Francis Group, London and New York, 202pp
- Pavia DL, Lampman GM, Kriz GS and Vyvyan JR, 2008, Introduction to Spectroscopy, Forth edition, Brooks/Cole, California, USA, 656pp
- Peslier AH, Woodland AB, Wolff JA, 2008, Fast kimberlite ascent rates estimated from hydrogen diffusion profiles in xenolithic mantle olivines from southern Africa, Science Direct, Elsevier, Geochimica et Cosmochimica Acta, v. 72, p. 2711–2722

- Poujol M, Robb LJ, Anhaeusser CR, Gericke B, 2003, A review of the geochronological constraints on the evolution of the Kaapvaal Craton, South Africa, Elsevier, v. 127, p. 181-213
- Purchase MD, 2009, OH Partitioning Coefficient between Garnets and Melt Inclusions in Lherzolite Xenoliths from the Kimberley Diamond Mine, South Africa, Unpublished Honours thesis, University of the Free State, South Africa
- Roper SM and Lister JR, 2007, Buoyancy-driven crack propagation: the limit of large fracture toughness, Journal of fluid Mechanism, v. 580, p. 359-380
- Rutherford MJ, 2008, Magma Ascent Rates, Reviews in Mineralogy and Geochemistry, v. 69, p. 241-271
- Sommer H and Gauert C, 2011, Hydrating laterally extensive regions of continental lithosphere by flat subduction, Journal of Geodynamics, v. 144, p. 17-24
- Sommer H, Regenauer-Lieb K, Gasharova B and Siret D, 2008, Grain boundaries: a possible water reservoir in the Earth's mantle?, Mineral Petrology, v. 94, p. 1–8
- Spear, FS, 1993, Metamorphic Phase Equilibria and Pressure-Temperature-Time Paths, Mineralogical Society of America, Washington, D. C., 799 pp
- Spence DA and Turcotte DL, 1990, Buoyancy-Driven Magma Fracture: A Mechanism for Ascent Through the Lithosphere and the Emplacement of Diamonds, Journal of Geophysics, v. 95, p. 5133-5139
- Streckeisen, A, 1976, To each plutonic rock its proper name, Earth Sci. Reviews., v. 12, p. 1–33
- Takada A, 1990, Experimental Study on Propagation of Liquid-Filled Crack in Gelatin: Shape and Velocity in Hydrostatic Stress Condition, Journal of Geophysics, v. 95, p. 8471-8481

- Varne R, 1970, Hornblende Lherzolite and the Upper Mantle, Contributions Mineralogy and Petrology, v. 27, p. 45-51
- Wagner PA, 1914, The Diamond Fields of Southern Africa, Cape Town, Struik, 355 pp.
- Wang L, Zhang Y And Essene EJ, 1996, Diffusion of the hydrous component in pyrope, American Mineralogist, v. 81, p. 706-718
- Weertman J, 1971a Theory of Water-Filled Crevasses in Glaciers Applied to Vertical Magma Transport beneath Oceanic Ridges, Journal of Geophysics, v. 76, p. 1171-1174
- Weertman J, 1971b, Velocity at Which Liquid-Filled Cracks Move in the Earth's Crust or in Glaciers, Journal of Geophysics, v. 76, p. 8544-8547
- Wenk HR and Bulak A, 2004, Minerals their Constitution and Origin. Cambridge University Press, UK, 646pp
- Winchell AN, 1945, Variations in composition and properties of calciferous amphiboles, American Mineralogist, v. 30, p.27-50
- Winter, J, 2001, An Introduction to Igneous and Metamorphic Petrology. Upper Saddle River, NJ. Prentice Hall Inc., 697pp
- Yardley BWD, 1981, Effect of cooling on the water content and mechanical behaviour of metamorphosed rocks, Geology, v. 9, p. 405-408
- Yardley BWD, 1989, An Introduction to Metamorphic Petrology, Pearson Education Limited, Harlow, England, 248pp
- Yoshino T, Yamazaki D and Mibe K, 2009, Well-wetted olivine grain boundaries in partially molten peridotite in the asthenosphere, Earth and Planetary Science Letters, Elsevier, v. 283, p. 167-173

- Zhang Y, 2010, Diffusion in Minerals and Melts: Theoretical Background, Reviews in Mineralogy & Geochemistry, v. 72, p. 5-59

Appendix 1: Mineral chemistry analysis

Olivines (4 oxygens)

wt %	KB1_OL12	KB1_OL13	KB1_OL14	KB1_OL15	KB1_OL16	KB1_OL17	KB1_OL18	KB1_OL19	KB1_OL21	KBL2_OL7	KB3_OL6	KB3_OL7	KB3_OL8	KB4_OL2	KB4_OL6	KB4_OL7
SiO2	40.46	40.94	40.75	40.87	41.11	41.04	41.01	40.95	40.82	58.89	42.18	42.24	42.52	41.40	41.92	41.65
TiO2	0.00	0.00	0.02	0.00	0.00	0.05	0.00	0.02	0.03	0.00	0.03	0.07	0.00	0.05	0.00	0.00
Al2O3	0.00	0.00	0.00	0.00	0.00	0.00	0.00	0.00	0.00	0.40	0.00	0.00	0.00	0.00	0.00	0.00
Cr2O3	0.00	0.08	0.00	0.00	0.00	0.02	0.00	0.01	0.02	0.24	0.00	0.02	0.00	0.00	0.02	0.05
BaO	0.00	0.00	0.00	0.00	0.00	0.00	0.00	0.00	0.00	0.00	0.00	0.00	0.00	0.00	0.00	0.00
FeO	9.23	9.46	9.37	9.52	9.37	9.27	9.04	9.59	9.38	5.08	7.66	7.63	7.57	7.47	7.50	7.55
MnO	0.20	0.00	0.09	0.07	0.15	0.04	0.13	0.03	0.07	0.13	0.08	0.15	0.06	0.14	0.07	0.09
MgO	47.90	49.62	49.13	48.93	49.43	49.32	48.34	49.16	48.55	35.74	52.61	52.50	52.79	50.42	49.99	49.68
CaO	0.02	0.01	0.04	0.62	0.00	0.00	0.02	0.00	0.09	0.28	0.01	0.06	0.01	0.04	0.00	0.06
Na2O	0.00	0.00	0.00	0.00	0.00	0.00	0.00	0.00	0.00	0.03	0.00	0.00	0.00	0.01	0.02	0.00
K2O	0.00	0.00	0.03	0.00	0.02	0.00	0.00	0.01	0.00	0.00	0.01	0.04	0.00	0.01	0.00	0.02
ZrO2	0.00	0.00	0.00	0.00	0.00	0.00	0.00	0.00	0.00	0.00	0.00	0.00	0.00	0.00	0.00	0.00
SO3	0.00	0.00	0.00	0.00	0.00	0.00	0.00	0.00	0.00	0.00	0.00	0.00	0.00	0.00	0.00	0.00
Cl	0.00	0.00	0.00	0.00	0.00	0.00	0.00	0.00	0.00	0.00	0.00	0.00	0.00	0.00	0.00	0.00
Total	97.81	100.10	99.43	100.00	100.08	99.74	98.55	99.77	98.94	100.80	102.59	102.71	102.95	99.53	99.51	99.12
Ferrous Form	KB1_OL12	KB1_OL13	KB1_OL14	KB1_OL15	KB1_OL16	KB1_OL17	KB1_OL18	KB1_OL19	KB1_OL21	KBL2_OL7	KB3_OL6	KB3_OL7	KB3_OL8	KB4_OL2	KB4_OL6	KB4_OL7
Si	1.01	1.00	1.00	1.00	1.00	1.00	1.01	1.00	1.01	1.33	1.00	1.00	1.00	1.01	1.02	1.02
Al	0.00	0.00	0.00	0.00	0.00	0.00	0.00	0.00	0.00	0.01	0.00	0.00	0.00	0.00	0.00	0.00
Ti	0.00	0.00	0.00	0.00	0.00	0.00	0.00	0.00	0.00	0.00	0.00	0.00	0.00	0.00	0.00	0.00
Cr	0.00	0.00	0.00	0.00	0.00	0.00	0.00	0.00	0.00	0.00	0.00	0.00	0.00	0.00	0.00	0.00
Ba	0.00	0.00	0.00	0.00	0.00	0.00	0.00	0.00	0.00	0.00	0.00	0.00	0.00	0.00	0.00	0.00
Mg	1.78	1.81	1.80	1.79	1.80	1.80	1.78	1.80	1.79	1.21	1.85	1.85	1.85	1.83	1.81	1.81
Fe	0.19	0.19	0.19	0.19	0.19	0.19	0.19	0.20	0.19	0.10	0.15	0.15	0.15	0.15	0.15	0.15
Mn	0.00	0.00	0.00	0.00	0.00	0.00	0.00	0.00	0.00	0.00	0.00	0.00	0.00	0.00	0.00	0.00
Ca	0.00	0.00	0.00	0.02	0.00	0.00	0.00	0.00	0.00	0.01	0.00	0.00	0.00	0.00	0.00	0.00
Na	0.00	0.00	0.00	0.00	0.00	0.00	0.00	0.00	0.00	0.00	0.00	0.00	0.00	0.00	0.00	0.00
K	0.00	0.00	0.00	0.00	0.00	0.00	0.00	0.00	0.00	0.00	0.00	0.00	0.00	0.00	0.00	0.00
Zr	0.00	0.00	0.00	0.00	0.00	0.00	0.00	0.00	0.00	0.00	0.00	0.00	0.00	0.00	0.00	0.00
SO3	0.00	0.00	0.00	0.00	0.00	0.00	0.00	0.00	0.00	0.00	0.00	0.00	0.00	0.00	0.00	0.00
Cl	0.00	0.00	0.00	0.00	0.00	0.00	0.00	0.00	0.00	0.00	0.00	0.00	0.00	0.00	0.00	0.00
Sum	2.99	3.00	3.00	3.00	3.00	2.99	2.99	3.00	2.99	2.66	3.00	3.00	3.00	2.99	2.98	2.98

wt %	KB4_OL10	KB4_OL20	KB4_OL21	KB4_OL22	KB4_OL23	KB4_OL24	KB4_OL30	KB4_OL31	KB4_OL33	KB5_OL2	KB5_OL9	KB5_OL11	KB5_OL18	KB6_OL6	KB6_OL7	KB6_OL8
SiO2	41.88	41.63	41.57	41.85	42.10	41.60	42.13	41.45	42.00	41.88	42.37	42.33	42.05	42.12	41.94	58.20
TiO2	0.00	0.05	0.04	0.00	0.00	0.00	0.00	0.00	0.00	0.00	0.05	0.00	0.06	0.09	0.06	0.01
Al2O3	0.00	0.00	0.00	0.00	0.00	0.00	0.00	0.00	0.00	0.00	0.00	0.00	0.00	0.00	0.00	0.35
Cr2O3	0.06	0.00	0.05	0.03	0.02	0.06	0.05	0.04	0.08	0.13	0.05	0.19	0.13	0.08	0.00	0.39
BaO	0.00	0.00	0.00	0.00	0.00	0.00	0.00	0.00	0.00	0.00	0.00	0.00	0.00	0.00	0.00	0.00
FeO	7.49	7.42	7.42	7.77	7.42	7.47	7.64	7.64	7.46	6.67	6.32	6.74	6.27	7.12	7.08	4.29
MnO	0.11	0.15	0.21	0.10	0.07	0.04	0.14	0.04	0.09	0.04	0.14	0.00	0.08	0.10	0.09	0.19
MgO	49.82	50.33	50.08	49.85	49.73	49.98	49.79	49.04	50.06	51.28	51.92	51.93	50.97	49.86	49.78	34.60
CaO	0.04	0.00	0.03	0.00	0.01	0.01	0.05	0.03	0.07	0.01	0.07	0.04	0.00	0.05	0.03	0.41
Na2O	0.00	0.01	0.00	0.00	0.00	0.01	0.00	0.00	0.00	0.00	0.00	0.00	0.02	0.00	0.00	0.19
K2O	0.00	0.07	0.00	0.00	0.00	0.00	0.00	0.02	0.00	0.00	0.05	0.05	0.08	0.00	0.00	0.09
ZrO2	0.00	0.00	0.00	0.00	0.00	0.00	0.00	0.00	0.00	0.00	0.00	0.00	0.00	0.00	0.00	0.00
SO3	0.00	0.00	0.00	0.00	0.00	0.00	0.00	0.00	0.00	0.00	0.00	0.00	0.00	0.00	0.00	0.00
Cl	0.00	0.00	0.00	0.00	0.00	0.00	0.00	0.00	0.00	0.00	0.00	0.00	0.00	0.00	0.00	0.00
Total	99.38	99.65	99.40	99.60	99.34	99.16	99.80	98.26	99.75	100.01	100.96	101.28	99.65	99.41	98.97	98.73
Ferrous Form	KB4_OL10	KB4_OL20	KB4_OL21	KB4_OL22	KB4_OL23	KB4_OL24	KB4_OL30	KB4_OL31	KB4_OL33	KB5_OL2	KB5_OL9	KB5_OL11	KB5_OL18	KB6_OL6	KB6_OL7	KB6_OL8
Si	1.02	1.01	1.01	1.02	1.02	1.01	1.02	1.02	1.02	1.01	1.01	1.01	1.02	1.02	1.02	1.34
Al	0.00	0.00	0.00	0.00	0.00	0.00	0.00	0.00	0.00	0.00	0.00	0.00	0.00	0.00	0.00	0.01
Ti	0.00	0.00	0.00	0.00	0.00	0.00	0.00	0.00	0.00	0.00	0.00	0.00	0.00	0.00	0.00	0.00
Cr	0.00	0.00	0.00	0.00	0.00	0.00	0.00	0.00	0.00	0.00	0.00	0.00	0.00	0.00	0.00	0.01
Ba	0.00	0.00	0.00	0.00	0.00	0.00	0.00	0.00	0.00	0.00	0.00	0.00	0.00	0.00	0.00	0.00
Mg	1.81	1.82	1.82	1.81	1.80	1.82	1.80	1.80	1.81	1.84	1.85	1.84	1.83	1.80	1.81	1.19
Fe	0.15	0.15	0.15	0.16	0.15	0.15	0.15	0.16	0.15	0.13	0.13	0.13	0.13	0.14	0.14	0.08
Mn	0.00	0.00	0.00	0.00	0.00	0.00	0.00	0.00	0.00	0.00	0.00	0.00	0.00	0.00	0.00	0.00
Ca	0.00	0.00	0.00	0.00	0.00	0.00	0.00	0.00	0.00	0.00	0.00	0.00	0.00	0.00	0.00	0.01
Na	0.00	0.00	0.00	0.00	0.00	0.00	0.00	0.00	0.00	0.00	0.00	0.00	0.00	0.00	0.00	0.01
K	0.00	0.00	0.00	0.00	0.00	0.00	0.00	0.00	0.00	0.00	0.00	0.00	0.00	0.00	0.00	0.00
Zr	0.00	0.00	0.00	0.00	0.00	0.00	0.00	0.00	0.00	0.00	0.00	0.00	0.00	0.00	0.00	0.00
SO3	0.00	0.00	0.00	0.00	0.00	0.00	0.00	0.00	0.00	0.00	0.00	0.00	0.00	0.00	0.00	0.00
Cl	0.00	0.00	0.00	0.00	0.00	0.00	0.00	0.00	0.00	0.00	0.00	0.00	0.00	0.00	0.00	0.00
Sum	2.98	2.99	2.99	2.98	2.98	2.99	2.98	2.98	2.98	2.99	2.99	2.99	2.98	2.98	2.98	2.66

wt %	KB6_ OL19	KB6_ OL20	KB6_ OL21	KB6_ OL25	KB6_ OL26	KB7_ OL5	KB7_ OL6	KB7_ OL13	KB8_ OL1	KB8_ OL13	KB8_ OL14	KB8_ OL15	KB8_ OL23	KB9_ OL8	KB9_ OL9	KB9_ OL15
SiO2	41.34	41.57	41.55	42.02	58.96	41.45	41.57	41.23	41.22	41.80	41.40	41.40	41.09	41.67	41.46	41.28
TiO2	0.04	0.00	0.00	0.00	0.03	0.00	0.05	0.01	0.00	0.00	0.00	0.05	0.00	0.03	0.03	0.00
Al2O3	0.00	0.00	0.00	0.00	0.66	0.00	0.12	0.00	0.00	0.00	0.00	0.00	0.00	0.04	0.00	0.00
Cr2O3	0.00	0.02	0.06	0.10	0.40	0.04	0.03	0.00	0.00	0.04	0.09	0.00	0.00	0.01	0.00	0.00
BaO	0.00	0.00	0.00	0.00	0.00	0.00	0.00	0.00	0.00	0.00	0.00	0.00	0.00	0.00	0.00	0.00
FeO	7.16	7.20	7.01	6.80	4.42	7.49	7.69	7.34	6.94	7.19	6.98	7.03	6.98	6.85	6.87	6.76
MnO	0.12	0.13	0.05	0.13	0.11	0.02	0.08	0.25	0.10	0.01	0.15	0.12	0.09	0.18	0.08	0.08
MgO	48.70	49.71	48.98	50.23	34.88	49.38	48.95	48.63	50.14	50.89	49.80	50.96	51.05	50.97	50.19	50.23
CaO	0.01	0.01	0.06	0.04	0.53	0.02	0.00	0.02	0.09	0.07	0.05	0.03	0.05	0.03	0.09	0.04
Na2O	0.00	0.00	0.04	0.00	0.12	0.00	0.00	0.00	0.05	0.00	0.00	0.01	0.01	0.00	0.00	0.02
K2O	0.00	0.05	0.05	0.06	0.00	0.07	0.01	0.04	0.04	0.00	0.00	0.00	0.00	0.05	0.03	0.02
ZrO2	0.00	0.00	0.00	0.00	0.00	0.00	0.00	0.00	0.00	0.00	0.00	0.00	0.00	0.00	0.00	0.00
SO3	0.00	0.00	0.00	0.00	0.00	0.00	0.00	0.00	0.00	0.00	0.00	0.00	0.00	0.00	0.00	0.00
Cl	0.00	0.00	0.00	0.00	0.00	0.00	0.00	0.00	0.00	0.00	0.00	0.00	0.00	0.00	0.00	0.00
Total	97.37	98.69	97.79	99.37	100.10	98.47	98.50	97.52	98.59	99.99	98.47	99.60	99.28	99.82	98.76	98.42
Ferrous Form	KB6_ OL19	KB6_ OL20	KB6_ OL21	KB6_ OL25	KB6_ OL26	KB7_ OL5	KB7_ OL6	KB7_ OL13	KB8_ OL1	KB8_ OL13	KB8_ OL14	KB8_ OL15	KB8_ OL23	KB9_ OL8	KB9_ OL9	KB9_ OL15
Si	1.02	1.02	1.02	1.02	1.34	1.02	1.02	1.02	1.01	1.01	1.01	1.00	1.00	1.01	1.01	1.01
Al	0.00	0.00	0.00	0.00	0.02	0.00	0.00	0.00	0.00	0.00	0.00	0.00	0.00	0.00	0.00	0.00
Ti	0.00	0.00	0.00	0.00	0.00	0.00	0.00	0.00	0.00	0.00	0.00	0.00	0.00	0.00	0.00	0.00
Cr	0.00	0.00	0.00	0.00	0.01	0.00	0.00	0.00	0.00	0.00	0.00	0.00	0.00	0.00	0.00	0.00
Ba	0.00	0.00	0.00	0.00	0.00	0.00	0.00	0.00	0.00	0.00	0.00	0.00	0.00	0.00	0.00	0.00
Mg	1.80	1.81	1.80	1.82	1.18	1.81	1.79	1.80	1.83	1.83	1.82	1.84	1.85	1.84	1.83	1.83
Fe	0.15	0.15	0.14	0.14	0.08	0.15	0.16	0.15	0.14	0.15	0.14	0.14	0.14	0.14	0.14	0.14
Mn	0.00	0.00	0.00	0.00	0.00	0.00	0.00	0.01	0.00	0.00	0.00	0.00	0.00	0.00	0.00	0.00
Ca	0.00	0.00	0.00	0.00	0.01	0.00	0.00	0.00	0.00	0.00	0.00	0.00	0.00	0.00	0.00	0.00
Na	0.00	0.00	0.00	0.00	0.01	0.00	0.00	0.00	0.00	0.00	0.00	0.00	0.00	0.00	0.00	0.00
K	0.00	0.00	0.00	0.00	0.00	0.00	0.00	0.00	0.00	0.00	0.00	0.00	0.00	0.00	0.00	0.00
Zr	0.00	0.00	0.00	0.00	0.00	0.00	0.00	0.00	0.00	0.00	0.00	0.00	0.00	0.00	0.00	0.00
SO3	0.00	0.00	0.00	0.00	0.00	0.00	0.00	0.00	0.00	0.00	0.00	0.00	0.00	0.00	0.00	0.00
Cl	0.00	0.00	0.00	0.00	0.00	0.00	0.00	0.00	0.00	0.00	0.00	0.00	0.00	0.00	0.00	0.00
Sum	2.98	2.98	2.98	2.98	2.65	2.98	2.98	2.98	2.99	2.99	2.98	2.99	3.00	2.99	2.99	2.99

Clinopyroxene (6 oxygens)

wt %	KBL2_ CPX1	KBL2_ CPX2	KBL2_ CPX5	KB3_ CPX7	KB3_ CPX10	KB3_ CPX20	KB3_ CPX22	KB3_ CPX23	KB3_ CPX24	KB3_ CPX25	KB4_ CPX1A	KB4_ CPX1	KB4_ CPX4
SiO2	54.96	54.40	54.69	51.88	46.28	54.12	57.75	55.81	56.55	56.45	55.31	55.17	54.69
TiO2	0.07	0.04	0.00	0.23	0.30	0.21	0.20	0.14	0.18	0.18	0.12	0.02	0.17
Al2O3	2.09	2.24	2.11	2.84	14.06	1.30	0.65	0.74	2.30	2.75	1.83	1.72	1.70
Cr2O3	1.48	1.68	1.35	0.24	2.02	0.87	0.40	0.94	1.26	0.80	1.86	1.96	1.91
BaO	0.00	0.00	0.00	0.00	0.00	0.00	0.00	0.00	0.00	0.00	0.00	0.00	0.00
FeO	2.36	2.32	2.37	3.75	3.24	5.19	4.16	4.89	3.51	3.21	2.03	2.20	2.14
MnO	0.04	0.03	0.01	0.53	0.11	0.22	0.23	0.20	0.00	0.11	0.00	0.06	0.13
MgO	15.26	15.77	15.34	16.97	19.70	25.71	18.26	17.91	17.49	18.07	16.44	17.05	16.72
CaO	19.87	19.85	20.16	20.62	9.48	12.75	20.30	18.66	19.04	18.07	19.85	19.16	19.36
Na2O	2.05	2.00	2.04	0.13	3.63	1.02	0.99	0.99	1.49	1.48	1.73	1.73	1.81
K2O	0.01	0.04	0.00	0.03	1.11	0.00	0.00	0.00	0.00	0.00	0.00	0.00	0.08
ZrO2	0.00	0.00	0.00	0.00	0.00	0.00	0.00	0.00	0.00	0.00	0.00	0.00	0.00
SO3	0.00	0.00	0.00	0.00	0.00	0.00	0.00	0.00	0.00	0.00	0.00	0.00	0.00
Cl	0.00	0.00	0.00	0.00	0.00	0.00	0.00	0.00	0.00	0.00	0.00	0.00	0.00
Total	98.19	98.37	98.08	97.20	99.92	101.39	102.92	100.27	101.82	101.12	99.18	99.07	98.71
Ferrous Form	**KBL2_ CPX1**	**KBL2_ CPX2**	**KBL2_ CPX5**	**KB3_ CPX7**	**KB3_ CPX10**	**KB3_ CPX20**	**KB3_ CPX22**	**KB3_ CPX23**	**KB3_ CPX24**	**KB3_ CPX25**	**KB4_ CPX1A**	**KB4_ CPX1**	**KB4_ CPX4**
Si	2.02	2.00	2.01	1.94	1.66	1.92	2.03	2.02	2.00	2.00	2.01	2.00	2.00
Al	0.09	0.10	0.09	0.12	0.60	0.05	0.03	0.03	0.10	0.11	0.08	0.07	0.07
Ti	0.00	0.00	0.00	0.01	0.01	0.01	0.01	0.00	0.00	0.00	0.00	0.00	0.00
Cr	0.04	0.05	0.04	0.01	0.06	0.02	0.01	0.03	0.04	0.02	0.05	0.06	0.06
Ba	0.00	0.00	0.00	0.00	0.00	0.00	0.00	0.00	0.00	0.00	0.00	0.00	0.00
Mg	0.83	0.86	0.84	0.95	1.06	1.36	0.95	0.96	0.92	0.95	0.89	0.92	0.91
Fe	0.07	0.07	0.07	0.12	0.10	0.15	0.12	0.15	0.10	0.10	0.06	0.07	0.07
Mn	0.00	0.00	0.00	0.02	0.00	0.01	0.01	0.01	0.00	0.00	0.00	0.00	0.00
Ca	0.78	0.78	0.79	0.83	0.37	0.48	0.76	0.72	0.72	0.69	0.77	0.75	0.76
Na	0.15	0.14	0.15	0.01	0.25	0.07	0.07	0.07	0.10	0.10	0.12	0.12	0.13
K	0.00	0.00	0.00	0.00	0.05	0.00	0.00	0.00	0.00	0.00	0.00	0.00	0.00
Zr	0.00	0.00	0.00	0.00	0.00	0.00	0.00	0.00	0.00	0.00	0.00	0.00	0.00
SO3	0.00	0.00	0.00	0.00	0.00	0.00	0.00	0.00	0.00	0.00	0.00	0.00	0.00
Cl	0.00	0.00	0.00	0.00	0.00	0.00	0.00	0.00	0.00	0.00	0.00	0.00	0.00
Sum	3.99	4.00	4.00	3.99	4.15	4.07	3.98	3.99	3.98	3.98	3.99	3.99	4.00

wt %	KB4_ CPX8	KB4_ CPX11	KB4_ CPX18	KB4_ CPX28	KB4_ CPX29	KB5_ CPX3	KB5_ CPX5	KB5_ CPX7	KB5_ CPX12	KB5_ CPX14	KB5_ CPX23	KB5_ CPX24	KB6_ CPX9
SiO2	55.21	55.16	55.56	54.91	54.61	55.27	54.77	55.05	55.37	54.18	55.13	55.24	54.25
TiO2	0.05	0.35	0.14	0.33	0.32	0.04	0.07	0.03	0.00	0.00	0.04	0.05	0.64
Al2O3	1.65	2.65	1.97	2.60	2.62	1.43	1.17	1.61	1.15	1.64	1.53	1.60	3.60
Cr2O3	2.02	2.18	1.89	2.10	2.31	1.16	1.22	1.33	0.98	1.76	1.16	1.07	0.83
BaO	0.00	0.00	0.00	0.00	0.00	0.00	0.00	0.00	0.00	0.00	0.00	0.00	0.00
FeO	2.36	2.40	2.39	2.20	2.41	1.47	1.34	1.38	1.37	1.35	1.37	1.32	2.81
MnO	0.00	0.08	0.10	0.12	0.08	0.00	0.00	0.03	0.12	0.01	0.00	0.00	0.16
MgO	17.35	16.39	16.55	16.43	16.45	17.54	18.09	17.76	17.92	17.50	17.55	18.39	16.15
CaO	19.36	18.23	19.28	18.21	17.97	22.95	22.98	23.15	23.28	22.82	23.05	23.12	19.25
Na2O	1.55	2.28	1.75	2.10	2.17	0.31	0.41	0.34	0.32	0.41	0.32	0.36	1.49
K2O	0.00	0.00	0.07	0.01	0.04	0.04	0.00	0.04	0.02	0.05	0.04	0.00	0.05
ZrO2	0.00	0.00	0.00	0.00	0.00	0.00	0.00	0.00	0.00	0.00	0.00	0.00	0.00
SO3	0.00	0.00	0.00	0.00	0.00	0.00	0.00	0.00	0.00	0.00	0.00	0.00	0.00
Cl	0.00	0.00	0.00	0.00	0.00	0.00	0.00	0.00	0.00	0.00	0.00	0.00	0.00
Total	99.56	99.72	99.71	99.00	98.98	100.19	100.05	100.71	100.51	99.71	100.18	101.14	99.23
Ferrous Form	**KB4_ CPX8**	**KB4_ CPX11**	**KB4_ CPX18**	**KB4_ CPX28**	**KB4_ CPX29**	**KB5_ CPX3**	**KB5_ CPX5**	**KB5_ CPX7**	**KB5_ CPX12**	**KB5_ CPX14**	**KB5_ CPX23**	**KB5_ CPX24**	**KB6_ CPX9**
Si	2.00	1.99	2.01	1.99	1.99	1.99	1.98	1.97	1.99	1.96	1.98	1.97	1.97
Al	0.07	0.11	0.08	0.11	0.11	0.06	0.05	0.07	0.05	0.07	0.06	0.07	0.15
Ti	0.00	0.01	0.00	0.01	0.01	0.00	0.00	0.00	0.00	0.00	0.00	0.00	0.02
Cr	0.06	0.06	0.05	0.06	0.07	0.03	0.03	0.04	0.03	0.05	0.03	0.03	0.02
Ba	0.00	0.00	0.00	0.00	0.00	0.00	0.00	0.00	0.00	0.00	0.00	0.00	0.00
Mg	0.94	0.88	0.89	0.89	0.89	0.94	0.97	0.95	0.96	0.95	0.94	0.98	0.87
Fe	0.07	0.07	0.07	0.07	0.07	0.04	0.04	0.04	0.04	0.04	0.04	0.04	0.09
Mn	0.00	0.00	0.00	0.00	0.00	0.00	0.00	0.00	0.00	0.00	0.00	0.00	0.00
Ca	0.75	0.70	0.75	0.71	0.70	0.88	0.89	0.89	0.90	0.89	0.89	0.88	0.75
Na	0.11	0.16	0.12	0.15	0.15	0.02	0.03	0.02	0.02	0.03	0.02	0.02	0.10
K	0.00	0.00	0.00	0.00	0.00	0.00	0.00	0.00	0.00	0.00	0.00	0.00	0.00
Zr	0.00	0.00	0.00	0.00	0.00	0.00	0.00	0.00	0.00	0.00	0.00	0.00	0.00
SO3	0.00	0.00	0.00	0.00	0.00	0.00	0.00	0.00	0.00	0.00	0.00	0.00	0.00
Cl	0.00	0.00	0.00	0.00	0.00	0.00	0.00	0.00	0.00	0.00	0.00	0.00	0.00
Sum	3.99	3.99	3.98	3.99	3.99	3.98	3.99	3.99	3.99	3.99	3.98	3.99	3.98

wt %	KB6_ CPX10	KB6_ CPX11	KB6_ CPX23	KB7_ CPX11	KB7_ CPX12	KB8_ CPX5	KB8_ CPX6	KB8_ CPX7	KB8_ CPX11	KB8_ CPX26	KB9_ CPX13	KB9_ CPX14	KB9_ CPX16
SiO2	53.36	53.75	55.53	54.84	54.41	53.60	53.84	54.42	53.83	55.37	54.64	54.45	54.01
TiO2	0.77	0.78	0.05	0.05	0.05	0.15	0.15	0.14	0.31	0.89	0.20	0.27	0.55
Al2O3	3.07	3.95	1.35	2.06	1.95	1.88	1.31	0.39	2.43	0.34	3.47	0.83	1.88
Cr2O3	0.78	0.94	0.28	1.62	1.75	1.44	1.72	2.20	1.64	1.25	2.72	1.61	1.46
BaO	0.00	0.00	0.00	0.00	0.00	0.00	0.00	0.00	0.00	0.00	0.00	0.00	0.00
FeO	2.75	2.74	2.89	2.14	2.09	2.45	2.54	2.78	2.72	3.63	2.10	2.18	2.64
MnO	0.22	0.09	0.25	0.00	0.00	0.18	0.23	0.06	0.21	0.09	0.02	0.29	0.18
MgO	16.30	16.59	18.50	15.92	15.56	16.30	16.38	16.42	16.10	19.48	14.27	17.97	17.07
CaO	19.18	19.64	19.80	19.77	19.84	19.90	19.17	19.34	19.83	18.62	17.74	19.97	19.36
Na2O	1.43	1.53	0.76	1.67	1.81	1.32	1.91	1.69	1.80	1.01	3.27	1.11	1.39
K2O	0.09	0.07	0.09	0.00	0.00	0.08	0.07	0.06	0.03	0.04	0.00	0.00	0.07
ZrO2	0.00	0.00	0.00	0.00	0.00	0.00	0.00	0.00	0.00	0.00	0.00	0.00	0.00
SO3	0.00	0.00	0.00	0.00	0.00	0.00	0.00	0.00	0.00	0.00	0.00	0.00	0.00
Cl	0.00	0.00	0.00	0.00	0.00	0.00	0.00	0.00	0.00	0.00	0.00	0.00	0.00
Total	97.95	100.07	99.50	98.08	97.46	97.29	97.33	97.50	98.89	100.72	98.43	98.66	98.60
Ferrous Form	**KB6_ CPX10**	**KB6_ CPX11**	**KB6_ CPX23**	**KB7_ CPX11**	**KB7_ CPX12**	**KB8_ CPX5**	**KB8_ CPX6**	**KB8_ CPX7**	**KB8_ CPX11**	**KB8_ CPX26**	**KB9_ CPX13**	**KB9_ CPX14**	**KB9_ CPX16**
Si	1.96	1.94	2.01	2.01	2.01	1.99	2.00	2.02	1.97	1.99	2.00	1.99	1.98
Al	0.13	0.17	0.06	0.09	0.08	0.08	0.06	0.02	0.10	0.01	0.15	0.04	0.08
Ti	0.02	0.02	0.00	0.00	0.00	0.00	0.00	0.00	0.01	0.02	0.01	0.01	0.02
Cr	0.02	0.03	0.01	0.05	0.05	0.04	0.05	0.06	0.05	0.04	0.08	0.05	0.04
Ba	0.00	0.00	0.00	0.00	0.00	0.00	0.00	0.00	0.00	0.00	0.00	0.00	0.00
Mg	0.89	0.89	1.00	0.87	0.86	0.90	0.91	0.91	0.88	1.04	0.78	0.98	0.93
Fe	0.08	0.08	0.09	0.07	0.06	0.08	0.08	0.09	0.08	0.11	0.06	0.07	0.08
Mn	0.01	0.00	0.01	0.00	0.00	0.01	0.01	0.00	0.01	0.00	0.00	0.01	0.01
Ca	0.76	0.76	0.77	0.78	0.79	0.79	0.76	0.77	0.78	0.72	0.69	0.78	0.76
Na	0.10	0.11	0.05	0.12	0.13	0.09	0.14	0.12	0.13	0.07	0.23	0.08	0.10
K	0.00	0.00	0.00	0.00	0.00	0.00	0.00	0.00	0.00	0.00	0.00	0.00	0.00
Zr	0.00	0.00	0.00	0.00	0.00	0.00	0.00	0.00	0.00	0.00	0.00	0.00	0.00
SO3	0.00	0.00	0.00	0.00	0.00	0.00	0.00	0.00	0.00	0.00	0.00	0.00	0.00
Cl	0.00	0.00	0.00	0.00	0.00	0.00	0.00	0.00	0.00	0.00	0.00	0.00	0.00
Sum	3.99	4.00	3.99	3.98	3.98	3.99	4.01	4.00	4.01	4.00	4.00	4.00	4.00

wt %	KB9_ CPX17	KB9_ CPX21	KB9_ CPX24	KB10_ CPX4	KB10_ CPX5
SiO2	54.72	53.29	54.26	55.24	55.17
TiO2	0.05	0.67	0.25	0.20	0.17
Al2O3	2.77	2.13	0.85	0.73	0.49
Cr2O3	2.25	1.99	1.65	1.70	1.23
BaO	0.00	0.00	0.00	0.00	0.00
FeO	2.05	2.25	2.68	2.60	2.52
MnO	0.06	0.12	0.13	0.11	0.08
MgO	15.01	16.67	18.70	16.87	18.68
CaO	18.65	19.93	19.43	20.22	19.79
Na2O	2.71	1.29	1.10	1.24	0.85
K2O	0.00	0.07	0.02	0.01	0.05
ZrO2	0.00	0.00	0.00	0.00	0.00
SO3	0.00	0.00	0.00	0.00	0.00
Cl	0.00	0.00	0.00	0.00	0.00
Total	98.26	98.41	99.06	98.92	99.02
Ferrous Form	KB9_ CPX17	KB9_ CPX21	KB9_ CPX24	KB10_ CPX4	KB10_ CPX5
Si	2.00	1.96	1.98	2.02	2.01
Al	0.12	0.09	0.04	0.03	0.02
Ti	0.00	0.02	0.01	0.01	0.00
Cr	0.07	0.06	0.05	0.05	0.04
Ba	0.00	0.00	0.00	0.00	0.00
Mg	0.82	0.91	1.02	0.92	1.01
Fe	0.06	0.07	0.08	0.08	0.08
Mn	0.00	0.00	0.00	0.00	0.00
Ca	0.73	0.79	0.76	0.79	0.77
Na	0.19	0.09	0.08	0.09	0.06
K	0.00	0.00	0.00	0.00	0.00
Zr	0.00	0.00	0.00	0.00	0.00
SO3	0.00	0.00	0.00	0.00	0.00
Cl	0.00	0.00	0.00	0.00	0.00
Sum	4.00	3.99	4.01	3.98	3.99

Orthopyroxene (6 oxygens)

wt %	KB1_ OPX6	KB1_ OPX7	KB1_ OPX8	KB1_ OPX9	KB1_ OPX10	KB1_ OPX11	KB1_ OPX22	KB1_ OPX23	KB1_ OPX24	KBL2_ OPX3	KBL2_ OPX4	KBL2_ OPX6	KB3_ OPX10
SiO2	57.15	57.20	57.51	57.66	57.60	57.58	58.09	57.60	57.24	40.95	58.30	58.54	57.57
TiO2	0.13	0.00	0.00	0.06	0.04	0.01	0.04	0.01	0.05	0.04	0.01	0.00	0.05
Al2O3	0.53	0.11	0.63	0.42	0.60	0.48	0.44	0.60	0.21	0.00	0.24	0.39	0.42
Cr2O3	0.31	0.25	0.27	0.18	0.31	0.34	0.32	0.29	0.21	0.08	0.12	0.19	0.26
BaO	0.00	0.00	0.00	0.00	0.00	0.00	0.00	0.00	0.00	0.00	0.00	0.00	0.00
FeO	5.55	5.66	5.86	5.76	5.76	5.58	5.72	5.64	5.60	8.16	5.04	5.08	4.70
MnO	0.09	0.07	0.09	0.06	0.16	0.10	0.11	0.11	0.14	0.07	0.14	0.11	0.10
MgO	33.63	33.51	34.06	33.91	33.91	33.62	33.89	33.73	33.49	49.18	34.98	35.58	35.16
CaO	0.48	0.48	0.54	0.45	0.50	0.46	0.37	0.48	0.48	0.03	0.30	0.27	0.40
Na2O	0.18	0.18	0.16	0.18	0.19	0.17	0.16	0.14	0.19	0.00	0.03	0.05	0.16
K2O	0.00	0.02	0.04	0.00	0.00	0.00	0.00	0.02	0.00	0.06	0.00	0.00	0.02
ZrO2	0.00	0.00	0.00	0.00	0.00	0.00	0.00	0.00	0.00	0.00	0.00	0.00	0.00
SO3	0.00	0.00	0.00	0.00	0.00	0.00	0.00	0.00	0.00	0.00	0.00	0.00	0.00
Cl	0.00	0.00	0.00	0.00	0.00	0.00	0.00	0.00	0.00	0.00	0.00	0.00	0.00
Total	98.04	97.48	99.16	98.69	99.07	98.35	99.14	98.62	97.61	98.56	99.15	100.22	98.82
Ferrous Form	**KB1_ OPX6**	**KB1_ OPX7**	**KB1_ OPX8**	**KB1_ OPX9**	**KB1_ OPX10**	**KB1_ OPX11**	**KB1_ OPX22**	**KB1_ OPX23**	**KB1_ OPX24**	**KBL2_ OPX3**	**KBL2_ OPX4**	**KBL2_ OPX6**	**KB3_ OPX10**
Si	2.00	2.01	1.99	2.01	2.00	2.01	2.01	2.00	2.01	1.51	2.01	2.00	1.99
Al	0.02	0.00	0.03	0.02	0.02	0.02	0.02	0.02	0.01	0.00	0.01	0.02	0.02
Ti	0.00	0.00	0.00	0.00	0.00	0.00	0.00	0.00	0.00	0.00	0.00	0.00	0.00
Cr	0.01	0.01	0.01	0.01	0.01	0.01	0.01	0.01	0.01	0.00	0.00	0.01	0.01
Ba	0.00	0.00	0.00	0.00	0.00	0.00	0.00	0.00	0.00	0.00	0.00	0.00	0.00
Mg	1.76	1.76	1.76	1.76	1.75	1.75	1.75	1.75	1.76	2.71	1.80	1.81	1.81
Fe	0.16	0.17	0.17	0.17	0.17	0.16	0.17	0.16	0.16	0.25	0.15	0.15	0.14
Mn	0.00	0.00	0.00	0.00	0.00	0.00	0.00	0.00	0.00	0.00	0.00	0.00	0.00
Ca	0.02	0.02	0.02	0.02	0.02	0.02	0.01	0.02	0.02	0.00	0.01	0.01	0.01
Na	0.01	0.01	0.01	0.01	0.01	0.01	0.01	0.01	0.01	0.00	0.00	0.00	0.01
K	0.00	0.00	0.00	0.00	0.00	0.00	0.00	0.00	0.00	0.00	0.00	0.00	0.00
Zr	0.00	0.00	0.00	0.00	0.00	0.00	0.00	0.00	0.00	0.00	0.00	0.00	0.00
SO3	0.00	0.00	0.00	0.00	0.00	0.00	0.00	0.00	0.00	0.00	0.00	0.00	0.00
Cl	0.00	0.00	0.00	0.00	0.00	0.00	0.00	0.00	0.00	0.00	0.00	0.00	0.00
Sum	3.99	3.99	3.99	3.99	3.99	3.98	3.98	3.98	3.98	4.49	3.98	3.99	4.00

wt %	KB3_ OPX9	KB3_ OPX11	KB4_ OPX3	KB4_ OPX5	KB4_ OPX9	KB4_ OPX15	KB4_ OPX16	KB4_ OPX17	KB5_ OPX1	KB5_ OPX15	KB5_ OPX16	KB5_ OPX19	KB5_ OPX21
SiO2	42.94	59.91	58.94	58.91	59.14	58.92	59.58	59.38	57.55	58.14	58.31	57.80	57.45
TiO2	0.00	0.00	0.11	0.00	0.01	0.02	0.08	0.12	0.01	0.11	0.00	0.02	0.00
Al2O3	0.00	0.42	0.74	0.27	0.53	0.26	0.50	0.72	1.99	2.28	1.93	2.04	2.46
Cr2O3	0.07	0.22	0.58	0.36	0.36	0.46	0.37	0.35	0.81	0.81	0.73	0.69	0.91
BaO	0.00	0.00	0.00	0.00	0.00	0.00	0.00	0.00	0.00	0.00	0.00	0.00	0.00
FeO	7.42	4.67	4.69	4.57	4.47	4.60	4.43	4.55	4.15	4.61	4.28	4.16	4.17
MnO	0.00	0.14	0.12	0.14	0.15	0.06	0.13	0.16	0.15	0.05	0.00	0.28	0.07
MgO	52.93	36.78	34.34	35.46	34.93	34.87	35.94	35.59	34.74	35.38	35.47	34.84	34.46
CaO	0.03	0.16	0.60	0.59	0.42	0.65	0.52	0.57	0.71	0.58	0.64	0.81	0.67
Na2O	0.00	0.05	0.16	0.17	0.09	0.12	0.18	0.09	0.02	0.01	0.00	0.02	0.00
K2O	0.00	0.02	0.00	0.00	0.07	0.03	0.03	0.00	0.02	0.02	0.01	0.00	0.04
ZrO2	0.00	0.00	0.00	0.00	0.00	0.00	0.00	0.00	0.00	0.00	0.00	0.00	0.00
SO3	0.00	0.00	0.00	0.00	0.00	0.00	0.00	0.00	0.00	0.00	0.00	0.00	0.00
Cl	0.00	0.00	0.00	0.00	0.00	0.00	0.00	0.00	0.00	0.00	0.00	0.00	0.00
Total	103.39	102.36	100.28	100.47	100.16	99.98	101.75	101.55	100.14	101.98	101.37	100.65	100.23
Ferrous Form	**KB3_ OPX9**	**KB3_ OPX11**	**KB4_ OPX3**	**KB4_ OPX5**	**KB4_ OPX9**	**KB4_ OPX15**	**KB4_ OPX16**	**KB4_ OPX17**	**KB5_ OPX1**	**KB5_ OPX15**	**KB5_ OPX16**	**KB5_ OPX19**	**KB5_ OPX21**
Si	1.51	2.00	2.01	2.00	2.01	2.01	2.00	2.00	1.96	1.95	1.97	1.96	1.96
Al	0.00	0.02	0.03	0.01	0.02	0.01	0.02	0.03	0.08	0.09	0.08	0.08	0.10
Ti	0.00	0.00	0.00	0.00	0.00	0.00	0.00	0.00	0.00	0.00	0.00	0.00	0.00
Cr	0.00	0.01	0.02	0.01	0.01	0.01	0.01	0.01	0.02	0.02	0.02	0.02	0.02
Ba	0.00	0.00	0.00	0.00	0.00	0.00	0.00	0.00	0.00	0.00	0.00	0.00	0.00
Mg	2.77	1.83	1.74	1.80	1.77	1.78	1.80	1.79	1.77	1.77	1.78	1.76	1.75
Fe	0.22	0.13	0.13	0.13	0.13	0.13	0.12	0.13	0.12	0.13	0.12	0.12	0.12
Mn	0.00	0.00	0.00	0.00	0.00	0.00	0.00	0.00	0.00	0.00	0.00	0.01	0.00
Ca	0.00	0.01	0.02	0.02	0.02	0.02	0.02	0.02	0.03	0.02	0.02	0.03	0.02
Na	0.00	0.00	0.01	0.01	0.01	0.01	0.01	0.01	0.00	0.00	0.00	0.00	0.00
K	0.00	0.00	0.00	0.00	0.00	0.00	0.00	0.00	0.00	0.00	0.00	0.00	0.00
Zr	0.00	0.00	0.00	0.00	0.00	0.00	0.00	0.00	0.00	0.00	0.00	0.00	0.00
SO3	0.00	0.00	0.00	0.00	0.00	0.00	0.00	0.00	0.00	0.00	0.00	0.00	0.00
Cl	0.00	0.00	0.00	0.00	0.00	0.00	0.00	0.00	0.00	0.00	0.00	0.00	0.00
Sum	4.49	3.99	3.97	3.99	3.97	3.98	3.99	3.98	3.99	3.99	3.99	3.99	3.98

wt %	KB5_ OPX25	KB5_ OPX28	KB6_ OPX4	KB6_ OPX5	KB6_ OPX12	KB6_ OPX13	KB6_ OPX17	KB7_ OPX2	KB7_ OPX3	KB7_ OPX7	KB7_ OPX8A	KB8_ OPX9	KB8_ OPX16
SiO2	0.27	59.30	59.16	58.99	59.15	58.62	58.47	58.87	58.91	58.47	57.99	56.31	58.81
TiO2	0.04	0.08	0.04	0.02	0.06	0.00	0.00	0.00	0.00	0.08	0.00	0.03	0.07
Al2O3	20.03	1.70	0.57	0.26	0.62	0.35	0.78	0.81	0.26	0.48	0.78	2.81	0.00
Cr2O3	47.70	0.89	0.38	0.35	0.38	0.38	0.26	0.34	0.21	0.23	0.31	0.58	0.20
BaO	0.00	0.00	0.00	0.00	0.00	0.00	0.00	0.00	0.00	0.00	0.00	0.00	0.00
FeO	16.12	4.71	4.40	4.43	4.36	4.30	4.35	4.56	4.38	4.57	4.55	4.47	4.52
MnO	0.47	0.03	0.01	0.11	0.11	0.05	0.07	0.07	0.23	0.07	0.15	0.08	0.08
MgO	11.87	35.57	34.90	34.67	34.56	34.94	33.81	34.32	35.92	34.88	33.97	32.47	35.56
CaO	0.49	0.45	0.44	0.41	0.49	0.39	0.53	0.46	0.14	0.45	0.37	2.25	0.08
Na2O	0.01	0.03	0.16	0.15	0.11	0.16	0.18	0.13	0.11	0.05	0.07	0.99	0.01
K2O	0.00	0.05	0.00	0.00	0.01	0.03	0.00	0.00	0.06	0.04	0.03	0.13	0.00
ZrO2	0.00	0.00	0.00	0.00	0.00	0.00	0.00	0.00	0.00	0.00	0.00	0.00	0.00
SO3	0.00	0.00	0.00	0.00	0.00	0.00	0.00	0.00	0.00	0.00	0.00	0.00	0.00
Cl	0.00	0.00	0.00	0.00	0.00	0.00	0.00	0.00	0.00	0.00	0.00	0.00	0.00
Total	97.00	102.81	100.06	99.38	99.84	99.22	98.44	99.55	100.21	99.30	98.22	100.11	99.32
Ferrous Form	**KB5_ OPX25**	**KB5_ OPX28**	**KB6_ OPX4**	**KB6_ OPX5**	**KB6_ OPX12**	**KB6_ OPX13**	**KB6_ OPX17**	**KB7_ OPX2**	**KB7_ OPX3**	**KB7_ OPX7**	**KB7_ OPX8A**	**KB8_ OPX9**	**KB8_ OPX16**
Si	0.01	1.97	2.01	2.02	2.02	2.01	2.02	2.02	2.01	2.01	2.01	1.94	2.02
Al	1.14	0.07	0.02	0.01	0.03	0.01	0.03	0.03	0.01	0.02	0.03	0.11	0.00
Ti	0.00	0.00	0.00	0.00	0.00	0.00	0.00	0.00	0.00	0.00	0.00	0.00	0.00
Cr	1.81	0.02	0.01	0.01	0.01	0.01	0.01	0.01	0.01	0.01	0.01	0.02	0.01
Ba	0.00	0.00	0.00	0.00	0.00	0.00	0.00	0.00	0.00	0.00	0.00	0.00	0.00
Mg	0.85	1.76	1.77	1.77	1.76	1.79	1.74	1.75	1.82	1.79	1.76	1.67	1.82
Fe	0.65	0.13	0.13	0.13	0.12	0.12	0.13	0.13	0.12	0.13	0.13	0.13	0.13
Mn	0.02	0.00	0.00	0.00	0.00	0.00	0.00	0.00	0.01	0.00	0.00	0.00	0.00
Ca	0.03	0.02	0.02	0.01	0.02	0.01	0.02	0.02	0.00	0.02	0.01	0.08	0.00
Na	0.00	0.00	0.01	0.01	0.01	0.01	0.01	0.01	0.01	0.00	0.00	0.07	0.00
K	0.00	0.00	0.00	0.00	0.00	0.00	0.00	0.00	0.00	0.00	0.00	0.01	0.00
Zr	0.00	0.00	0.00	0.00	0.00	0.00	0.00	0.00	0.00	0.00	0.00	0.00	0.00
SO3	0.00	0.00	0.00	0.00	0.00	0.00	0.00	0.00	0.00	0.00	0.00	0.00	0.00
Cl	0.00	0.00	0.00	0.00	0.00	0.00	0.00	0.00	0.00	0.00	0.00	0.00	0.00
Sum	4.51	3.98	3.97	3.97	3.97	3.98	3.96	3.97	3.99	3.98	3.97	4.03	3.98

wt %	KB8_ OPX20	KB8_ OPX25	KB8_ OPX28	KB9_ OPX6	KB9_ OPX19	KB10_ OPX1	KB10_ OPX2	KB10_ OPX3	KB10_ OPX6	KB10_ OPX7
SiO2	47.53	59.57	60.11	58.48	58.23	56.33	56.72	56.64	57.03	55.53
TiO2	0.01	0.00	0.05	0.00	0.04	0.00	0.11	0.04	0.06	0.01
Al2O3	10.66	0.00	0.53	0.43	0.28	3.29	3.13	3.06	3.14	2.67
Cr2O3	1.20	0.07	0.14	0.34	0.39	0.85	1.00	0.86	0.74	0.85
BaO	0.00	0.00	0.00	0.00	0.00	0.00	0.00	0.00	0.00	0.00
FeO	3.07	4.65	4.59	4.25	4.21	4.34	4.92	4.26	4.26	4.40
MnO	0.00	0.09	0.07	0.20	0.04	0.15	0.16	0.07	0.08	0.13
MgO	19.86	36.81	36.09	35.71	34.92	33.96	33.69	34.22	34.26	33.96
CaO	10.06	0.15	0.11	0.25	0.29	0.81	0.59	0.77	0.90	0.77
Na2O	4.30	0.01	0.01	0.08	0.09	0.05	0.06	0.01	0.04	0.02
K2O	0.41	0.00	0.01	0.03	0.05	0.03	0.03	0.06	0.00	0.01
ZrO2	0.00	0.00	0.00	0.00	0.00	0.00	0.00	0.00	0.00	0.00
SO3	0.00	0.00	0.00	0.00	0.00	0.00	0.00	0.00	0.00	0.00
Cl	0.00	0.00	0.00	0.00	0.00	0.00	0.00	0.00	0.00	0.00
Total	97.10	101.34	101.71	99.76	98.54	99.81	100.41	99.98	100.50	98.35
Ferrous Form	**KB8_ OPX20**	**KB8_ OPX25**	**KB8_ OPX28**	**KB9_ OPX6**	**KB9_ OPX19**	**KB10_ OPX1**	**KB10_ OPX2**	**KB10_ OPX3**	**KB10_ OPX6**	**KB10_ OPX7**
Si	1.75	2.01	2.01	2.00	2.01	1.93	1.94	1.94	1.94	1.94
Al	0.46	0.00	0.02	0.02	0.01	0.13	0.13	0.12	0.13	0.11
Ti	0.00	0.00	0.00	0.00	0.00	0.00	0.00	0.00	0.00	0.00
Cr	0.04	0.00	0.00	0.01	0.01	0.02	0.03	0.02	0.02	0.02
Ba	0.00	0.00	0.00	0.00	0.00	0.00	0.00	0.00	0.00	0.00
Mg	1.09	1.85	1.80	1.82	1.80	1.74	1.72	1.75	1.74	1.77
Fe	0.09	0.13	0.13	0.12	0.12	0.12	0.14	0.12	0.12	0.13
Mn	0.00	0.00	0.00	0.01	0.00	0.00	0.00	0.00	0.00	0.00
Ca	0.40	0.01	0.00	0.01	0.01	0.03	0.02	0.03	0.03	0.03
Na	0.31	0.00	0.00	0.01	0.01	0.00	0.00	0.00	0.00	0.00
K	0.02	0.00	0.00	0.00	0.00	0.00	0.00	0.00	0.00	0.00
Zr	0.00	0.00	0.00	0.00	0.00	0.00	0.00	0.00	0.00	0.00
SO3	0.00	0.00	0.00	0.00	0.00	0.00	0.00	0.00	0.00	0.00
Cl	0.00	0.00	0.00	0.00	0.00	0.00	0.00	0.00	0.00	0.00
Sum	4.16	3.99	3.97	3.99	3.98	3.99	3.98	3.99	3.99	4.00

Garnets (12 oxygens)

wt %	KB1_ grt1	KB1_ grt2	KB1_ grt3	KB1_ grt4	KB1_ grt5	KB3_ Gt1	KB3_ Gt6	KB3_ grt15	KB3_ grt1	KB3_ grt2	KB3_ grt3	KB4_ GT2	KB4_ GT12	KB4_ GT13
SiO2	42.43	42.34	42.99	42.54	42.57	42.59	42.87	42.26	42.64	42.75	42.63	42.84	42.12	42.05
TiO2	0.17	0.16	0.12	0.15	0.12	0.11	0.07	0.03	0.08	0.03	0.02	0.40	0.04	0.12
Al2O3	21.43	21.51	21.75	21.50	21.53	21.79	22.25	21.03	22.05	22.10	21.58	19.59	18.81	18.63
Cr2O3	2.95	3.03	3.16	2.80	2.81	2.51	1.79	3.04	2.77	2.79	2.73	5.31	6.67	6.35
BaO	0.00	0.00	0.00	0.00	0.00	0.00	0.00	0.00	0.00	0.00	0.00	0.00	0.00	0.00
FeO	6.05	6.14	6.13	6.29	6.22	8.00	7.98	7.86	7.80	7.65	7.80	6.69	6.76	6.66
MnO	0.25	0.23	0.32	0.27	0.37	0.42	0.55	0.37	0.46	0.32	0.36	0.36	0.30	0.29
MgO	22.44	22.06	22.75	22.83	22.75	20.45	20.35	19.91	21.27	21.39	21.59	20.29	19.75	19.46
CaO	4.00	3.94	4.00	4.01	3.97	4.46	4.35	4.83	4.48	4.48	4.49	5.63	5.92	5.95
Na2O	0.03	0.03	0.03	0.04	0.03	0.03	0.04	0.02	0.02	0.00	0.01	0.08	0.00	0.04
K2O	0.05	0.03	0.01	0.04	0.00	0.04	0.10	0.00	0.04	0.00	0.00	0.00	0.00	0.02
ZrO2	0.00	0.00	0.00	0.00	0.00	0.00	0.00	0.00	0.00	0.00	0.00	0.00	0.00	0.00
SO3	0.00	0.00	0.00	0.00	0.00	0.00	0.00	0.00	0.00	0.00	0.00	0.00	0.00	0.00
Cl	0.00	0.00	0.00	0.00	0.00	0.00	0.00	0.00	0.00	0.00	0.00	0.00	0.00	0.00
Total	99.80	99.46	101.25	100.45	100.38	100.39	100.36	99.35	101.62	101.50	101.20	101.18	100.35	99.56
Ferrous Form	KB1_ grt1	KB1_ grt2	KB1_ grt3	KB1_ grt4	KB1_ grt5	KB3_ Gt1	KB3_ Gt6	KB3_ grt15	KB3_ grt1	KB3_ grt2	KB3_ grt3	KB4_ GT2	KB4_ GT12	KB4_ GT13
Si	3.00	3.01	3.00	2.99	3.00	3.02	3.03	3.03	2.99	3.00	3.00	3.03	3.02	3.04
Al	1.79	1.80	1.79	1.78	1.79	1.82	1.86	1.78	1.82	1.83	1.79	1.64	1.59	1.59
Ti	0.01	0.01	0.01	0.01	0.01	0.01	0.00	0.00	0.00	0.00	0.00	0.02	0.00	0.01
Cr	0.16	0.17	0.17	0.16	0.16	0.14	0.10	0.17	0.15	0.15	0.15	0.30	0.38	0.36
Ba	0.00	0.00	0.00	0.00	0.00	0.00	0.00	0.00	0.00	0.00	0.00	0.00	0.00	0.00
Mg	2.37	2.33	2.37	2.39	2.39	2.16	2.15	2.13	2.22	2.23	2.27	2.14	2.11	2.10
Fe	0.36	0.36	0.36	0.37	0.37	0.47	0.47	0.47	0.46	0.45	0.46	0.40	0.41	0.40
Mn	0.01	0.01	0.02	0.02	0.02	0.02	0.03	0.02	0.03	0.02	0.02	0.02	0.02	0.02
Ca	0.30	0.30	0.30	0.30	0.30	0.34	0.33	0.37	0.34	0.34	0.34	0.43	0.46	0.46
Na	0.00	0.00	0.00	0.01	0.00	0.00	0.01	0.00	0.00	0.00	0.00	0.01	0.00	0.01
K	0.00	0.00	0.00	0.00	0.00	0.00	0.01	0.00	0.00	0.00	0.00	0.00	0.00	0.00
Zr	0.00	0.00	0.00	0.00	0.00	0.00	0.00	0.00	0.00	0.00	0.00	0.00	0.00	0.00
SO3	0.00	0.00	0.00	0.00	0.00	0.00	0.00	0.00	0.00	0.00	0.00	0.00	0.00	0.00
Cl	0.00	0.00	0.00	0.00	0.00	0.00	0.00	0.00	0.00	0.00	0.00	0.00	0.00	0.00
Sum	8.02	8.00	8.02	8.03	8.03	8.00	7.99	7.99	8.02	8.01	8.03	7.98	7.99	7.98

wt %	KB4_ GT14A	KB4_ GT19	KB6_ GT1	KB6_ GT1A	KB6_ GT2	KB6_ GT3	KB6_ GT14	KB6_ GT15	KB6_ GT18	KB6_ GT28	KB6_ GT31	KB7_ GT1	KB7_ GT3	KB7_ GT9
SiO2	42.81	42.00	41.83	42.00	42.49	42.57	42.10	42.19	41.78	42.28	42.56	41.62	41.64	42.18
TiO2	0.09	0.18	0.12	0.13	0.00	0.11	0.01	0.07	0.04	0.05	0.02	0.07	0.11	0.09
Al2O3	19.34	18.53	19.48	19.69	20.24	20.02	19.60	20.16	20.12	20.02	20.33	20.26	20.05	20.47
Cr2O3	6.49	6.46	4.96	4.83	4.96	5.00	4.87	4.64	4.83	4.90	4.79	4.04	4.20	4.30
BaO	0.00	0.00	0.00	0.00	0.00	0.00	0.00	0.00	0.00	0.00	0.00	0.00	0.00	0.00
FeO	6.89	6.74	6.60	6.81	6.68	6.76	6.53	6.93	6.52	6.78	6.80	6.88	6.91	7.04
MnO	0.35	0.35	0.29	0.33	0.31	0.35	0.42	0.33	0.28	0.32	0.35	0.42	0.39	0.32
MgO	20.20	20.07	20.15	20.21	20.64	20.28	18.90	19.99	20.53	20.40	20.19	19.16	19.22	19.90
CaO	6.00	5.85	5.20	4.81	5.03	5.02	5.04	5.05	4.79	4.90	4.95	5.11	5.17	5.02
Na2O	0.03	0.03	0.05	0.00	0.04	0.02	0.00	0.04	0.06	0.05	0.46	0.00	0.05	0.01
K2O	0.07	0.02	0.00	0.02	0.00	0.02	0.00	0.02	0.00	0.00	0.00	0.00	0.01	0.00
ZrO2	0.00	0.00	0.00	0.00	0.00	0.00	0.00	0.00	0.00	0.00	0.00	0.00	0.00	0.00
SO3	0.00	0.00	0.00	0.00	0.00	0.00	0.00	0.00	0.00	0.00	0.00	0.00	0.00	0.00
Cl	0.00	0.00	0.00	0.00	0.00	0.00	0.00	0.00	0.00	0.00	0.00	0.00	0.00	0.00
Total	102.28	100.23	98.68	98.84	100.39	100.15	97.47	99.40	98.94	99.70	100.46	97.55	97.75	99.33
Ferrous Form	KB4_ GT14A	KB4_ GT19	KB6_ GT1	KB6_ GT1A	KB6_ GT2	KB6_ GT3	KB6_ GT14	KB6_ GT15	KB6_ GT18	KB6_ GT28	KB6_ GT31	KB7_ GT1	KB7_ GT3	KB7_ GT9
Si	3.02	3.02	3.03	3.04	3.02	3.04	3.08	3.03	3.01	3.03	3.03	3.04	3.04	3.03
Al	1.61	1.57	1.66	1.68	1.70	1.68	1.69	1.71	1.71	1.69	1.71	1.75	1.73	1.73
Ti	0.00	0.01	0.01	0.01	0.00	0.01	0.00	0.00	0.00	0.00	0.00	0.00	0.01	0.00
Cr	0.36	0.37	0.28	0.28	0.28	0.28	0.28	0.26	0.28	0.28	0.27	0.23	0.24	0.24
Ba	0.00	0.00	0.00	0.00	0.00	0.00	0.00	0.00	0.00	0.00	0.00	0.00	0.00	0.00
Mg	2.12	2.15	2.18	2.18	2.19	2.16	2.06	2.14	2.21	2.18	2.14	2.09	2.09	2.13
Fe	0.41	0.41	0.40	0.41	0.40	0.40	0.40	0.42	0.39	0.41	0.40	0.42	0.42	0.42
Mn	0.02	0.02	0.02	0.02	0.02	0.02	0.03	0.02	0.02	0.02	0.02	0.03	0.02	0.02
Ca	0.45	0.45	0.40	0.37	0.38	0.38	0.40	0.39	0.37	0.38	0.38	0.40	0.40	0.39
Na	0.00	0.00	0.01	0.00	0.01	0.00	0.00	0.01	0.01	0.01	0.06	0.00	0.01	0.00
K	0.01	0.00	0.00	0.00	0.00	0.00	0.00	0.00	0.00	0.00	0.00	0.00	0.00	0.00
Zr	0.00	0.00	0.00	0.00	0.00	0.00	0.00	0.00	0.00	0.00	0.00	0.00	0.00	0.00
SO3	0.00	0.00	0.00	0.00	0.00	0.00	0.00	0.00	0.00	0.00	0.00	0.00	0.00	0.00
Cl	0.00	0.00	0.00	0.00	0.00	0.00	0.00	0.00	0.00	0.00	0.00	0.00	0.00	0.00
Sum	8.00	8.00	7.99	7.98	7.99	7.98	7.93	7.98	8.00	7.99	8.01	7.96	7.97	7.98

wt %	KB7_ GT10	KB9_ GT1	KB9_ GT2	KB9_ GT3	KB9_ GT10	KB9_ GT11	KB9_ GT12
SiO2	41.95	41.92	41.45	41.96	41.99	41.72	42.33
TiO2	0.05	0.04	0.07	0.04	0.15	0.04	0.09
Al2O3	20.57	20.56	20.40	20.69	21.06	20.11	21.21
Cr2O3	4.24	3.94	3.99	3.97	3.90	3.89	4.20
BaO	0.00	0.00	0.00	0.00	0.00	0.00	0.00
FeO	6.82	6.99	7.02	6.77	6.88	6.90	6.94
MnO	0.38	0.41	0.43	0.57	0.43	0.41	0.40
MgO	20.26	20.20	20.17	20.46	20.17	20.26	20.66
CaO	5.19	4.83	4.95	4.97	4.95	4.73	4.91
Na2O	0.00	0.02	0.05	0.02	0.03	0.03	0.03
K2O	0.00	0.02	0.00	0.00	0.04	0.04	0.04
ZrO2	0.00	0.00	0.00	0.00	0.00	0.00	0.00
SO3	0.00	0.00	0.00	0.00	0.00	0.00	0.00
Cl	0.00	0.00	0.00	0.00	0.00	0.00	0.00
Total	99.47	98.94	98.54	99.47	99.60	98.13	100.78
Ferrous Form	**KB7_ GT10**	**KB9_ GT1**	**KB9_ GT2**	**KB9_ GT3**	**KB9_ GT10**	**KB9_ GT11**	**KB9_ GT12**
Si	3.01	3.02	3.01	3.01	3.01	3.03	3.00
Al	1.74	1.75	1.74	1.75	1.78	1.72	1.77
Ti	0.00	0.00	0.00	0.00	0.01	0.00	0.00
Cr	0.24	0.22	0.23	0.23	0.22	0.22	0.23
Ba	0.00	0.00	0.00	0.00	0.00	0.00	0.00
Mg	2.17	2.17	2.18	2.19	2.15	2.19	2.18
Fe	0.41	0.42	0.43	0.41	0.41	0.42	0.41
Mn	0.02	0.02	0.03	0.03	0.03	0.03	0.02
Ca	0.40	0.37	0.38	0.38	0.38	0.37	0.37
Na	0.00	0.00	0.01	0.00	0.00	0.00	0.00
K	0.00	0.00	0.00	0.00	0.00	0.00	0.00
Zr	0.00	0.00	0.00	0.00	0.00	0.00	0.00
SO3	0.00	0.00	0.00	0.00	0.00	0.00	0.00
Cl	0.00	0.00	0.00	0.00	0.00	0.00	0.00
Sum	8.00	7.99	8.01	8.00	7.99	8.00	8.00

Biotites

wt%	KB3_BT5	KB3_BT27	KB3_BT28	KB3_BT29	KB4_BT26	KB6_BT30	KB6_BT32	KB8_BT2	KB8_BT12	KB8_BT21	KB9_BT4	KB9_BT5	KB9_BT18	KB9_BT22	KB9_BT25
SiO2	39.81	41.70	39.15	40.42	35.25	41.32	40.55	40.93	41.45	40.89	38.11	40.72	40.08	39.96	40.20
TiO2	0.71	0.50	0.92	0.49	0.22	1.20	0.81	0.44	0.46	0.35	0.41	0.60	1.72	1.69	1.57
Al2O3	15.07	12.70	14.64	15.61	12.03	12.72	13.72	13.98	14.17	13.31	15.70	13.42	13.93	13.83	13.86
Cr2O3	1.40	2.27	1.55	1.05	3.76	1.31	1.82	0.90	0.76	0.87	2.74	1.07	2.11	2.25	2.20
BaO	0.00	0.00	0.00	0.00	0.00	0.00	0.00	0.00	0.00	0.00	0.00	0.00	0.00	0.00	0.00
FeO	3.14	3.81	3.16	3.17	6.26	2.99	2.85	2.23	2.21	2.29	2.93	2.50	2.63	2.57	2.65
MnO	0.07	0.09	0.08	0.00	0.08	0.15	0.00	0.04	0.03	0.06	0.11	0.06	0.00	0.11	0.00
MgO	23.61	20.48	25.10	25.61	27.72	23.72	23.15	24.75	25.23	25.32	22.65	24.67	23.58	22.74	23.69
CaO	0.03	7.92	0.01	0.00	0.77	0.06	0.08	0.03	0.06	0.00	0.09	0.05	0.03	0.13	0.06
Na2O	1.00	3.27	1.33	1.17	0.92	0.37	0.50	1.65	1.53	1.69	0.53	0.89	0.39	0.49	0.39
K2O	8.70	2.03	8.13	8.67	2.64	9.75	10.11	7.85	7.97	8.20	10.00	9.46	9.97	9.96	9.84
ZrO2	0.00	0.00	0.00	0.00	0.00	0.00	0.00	0.00	0.00	0.00	0.00	0.00	0.00	0.00	0.00
SO3	0.00	0.00	0.00	0.00	0.00	0.00	0.00	0.00	0.00	0.00	0.00	0.00	0.00	0.00	0.00
Cl	0.00	0.00	0.00	0.00	0.00	0.00	0.00	0.00	0.00	0.00	0.00	0.00	0.00	0.00	0.00
F	0.00	0.00	0.00	0.00	0.00	0.00	0.00	0.00	0.00	0.00	0.00	0.00	0.00	0.00	0.00
Total	93.54	94.77	94.06	96.18	89.64	93.59	93.58	92.79	93.88	92.98	93.26	93.43	94.44	93.73	94.45

Amphiboles

wt%	KB3_ AM11	KB3_ AM13	KB3_ AM14	KB3_ AM15	KB3_ AM16	KB3_ AM17
SiO2	46.49	47.28	44.22	44.80	46.50	45.99
TiO2	0.26	0.27	0.45	0.60	0.17	0.35
Al2O3	13.98	11.98	13.44	12.87	15.19	12.99
Cr2O3	1.98	2.08	1.64	1.83	2.11	2.03
BaO	0.00	0.00	0.00	0.00	0.00	0.00
FeO	3.43	3.68	4.35	3.97	3.61	3.22
MnO	0.00	0.06	0.07	0.11	0.11	0.00
MgO	19.93	20.14	18.89	18.49	20.01	20.00
CaO	8.99	9.18	11.68	11.31	8.58	9.13
Na2O	3.88	4.15	3.34	3.39	3.88	3.70
K2O	0.91	1.03	0.77	0.85	0.76	1.05
ZrO2	0.00	0.00	0.00	0.00	0.00	0.00
SO3	0.00	0.00	0.00	0.00	0.00	0.00
Cl	0.00	0.00	0.00	0.00	0.00	0.00
F	0.00	0.00	0.00	0.00	0.00	0.00
Total	99.86	99.86	98.86	98.21	100.92	98.46

Serpentine

wt%	KB3 serp14
SiO2	32.05
TiO2	0.04
Al2O3	16.73
Cr2O3	1.09
BaO	0.00
FeO	8.23
MnO	0.15
MgO	24.64
CaO	1.13
Na2O	0.03
K2O	0.00
ZrO2	0.00
SO3	0.00
Cl	0.00
F	0.00
Total	84.10